INFORMATION TO USERS

This manuscript has been reproduced from the microfilm master. UMI films the text directly from the original or copy submitted. Thus, some thesis and dissertation copies are in typewriter face, while others may be from any type of computer printer.

The quality of this reproduction is dependent upon the quality of the copy submitted. Broken or indistinct print, colored or poor quality illustrations and photographs, print bleedthrough, substandard margins, and improper alignment can adversely affect reproduction.

In the unlikely event that the author did not send UMI a complete manuscript and there are missing pages, these will be noted. Also, if unauthorized copyright material had to be removed, a note will indicate the deletion.

Oversize materials (e.g., maps, drawings, charts) are reproduced by sectioning the original, beginning at the upper left-hand corner and continuing from left to right in equal sections with small overlaps. Each original is also photographed in one exposure and is included in reduced form at the back of the book.

Photographs included in the original manuscript have been reproduced xerographically in this copy. Higher quality 6" x 9" black and white photographic prints are available for any photographs or illustrations appearing in this copy for an additional charge. Contact UMI directly to order.

UMI

A Bell & Howell Information Company
300 North Zeeb Road, Ann Arbor MI 48106-1346 USA
313/761-4700 800/521-0600

The Influence of Convectively Generated Thermal Forcing on the Mesoscale Circulation around Squall Lines.

by

Rajul Edward Pandya

A dissertation submitted in partial fulfillment
of the requirements for the degree of

Doctor of Philosophy

University of Washington

1996

Approved by Robert A. Houze

(Chairperson of Supervisory Committee)

Program Authorized
to Offer Degree ATMOSPHERIC SCIENCES

Date 7 OCTOBER 1996

In presenting this dissertation in partial fulfillment of the requirements for the Doctoral Degree at the University of Washington, I agree that the Library shall make its copies freely available for inspection. I further agree that extensive copying of this dissertation is allowable only for scholarly purposes consistent with "fair use" as prescribed in the U.S. Copyright Law. Requests for copying or reproduction of this dissertation may be referred to University Microfilms, 1490 Eisenhower Place, P.O. Box 975, Ann Arbor, MI 48106, to whom the author has granted "the right to reproduce and sell (a) copies of the manuscript in microfilm and/or (b) printed copies of the manuscript made from microfilm."

Signature 

Date 7 OCTOBER 1996

University of Washington

Abstract

The Influence of Convectively Generated Thermal Forcing on the Mesoscale Circulation around Squall Lines.

by Rajul Edward Pandya

Chairperson of Supervisory Committee: Professor Dale R. Durran

Department of Atmospheric Sciences

The dynamical processes that determine the kinematic and thermodynamic structure of the mesoscale region around squall lines are examined using a series of numerical simulations. The features that develop in a realistic two-dimensional reference simulation of a squall line with trailing stratiform precipitation are compared to the features generated by a steady thermal forcing in a "dry" two-dimensional simulation with no microphysical parameterization. The thermal forcing in the dry simulation is a scaled and smoothed time average of the latent heat released and absorbed in and near the leading convective line in the reference simulation. The mesoscale circulation in the dry simulation resembles the mesoscale circulation in the reference simulation and around real squall lines suggesting that the circulation around squall lines is the result of gravity waves forced primarily by the low-frequency components of the latent heating and cooling in the leading line.

Other features of real squall lines squall lines and the reference simulation are reproduced in the dry simulation as well, including cellularity in the leading line and upper-level potential temperature perturbations in the trailing stratiform region. The gravity waves generated by the time-mean thermal forcing in the leading line are also shown to play a

role in the distribution of stratiform cloudiness. Additional numerical simulations, in which either the thermal forcing or the large-scale environmental conditions were varied, reveal that the circulation generated by the thermal forcing shows a greater sensitivity to variations in the thermal forcing than to variations in the large-scale environment. Finally, it is demonstrated that the depth of the thermal forcing in the leading convective line, not the height of the tropopause, is the primary factor determining the height of the trailing anvil cloud.

The comparison of dry and reference simulations is repeated using three-dimensional simulations. A three-dimensional thermal forcing, constructed from the pattern of latent heating and cooling in the leading convective line of a three-dimensional moist simulation, is shown to generate a circulation which resembles the circulation in the three-dimensional reference simulation and in real squall lines. This circulation included the line-normal components of the flow found in the two-dimensional simulations, as well as three-dimensional components of the flow such as the Mesoscale Convective Vortex. Additional simulations demonstrate that the Coriolis force can modify the circulation toward an asymmetric organization even when the thermal forcing and the mean-state environment exhibit no asymmetries.

TABLE OF CONTENTS

LIST OF FIGURES

LIST OF TABLES

ACKNOWLEDGMENTS

Financial support was provided by a National Science Foundation Graduate Fellowship and a National Aeronautics and Space Administration Space Grant. Additional support was provided by National Science Foundation Grant ATM-9218376, with Dr. Dale Durran as the principal investigator. Computer resources were provided by the National Center for Atmospheric Research, which is sponsored by the National Science Foundation.

I wish to thank my advisor, Dr. Dale Durran, for his careful mentorship. His insight and guidance were invaluable in developing the ideas presented in this thesis and an important part of my own (ongoing) maturation as a scientist. His sense of humor and enthusiasm have made this process enjoyable. Dr. Bradley Smull provided many informative discussions and careful comments which significantly improved this thesis. The members of my reading committee, Dr. Christopher Bretherton and Dr. Robert Houze, Jr., also provided comments which improved this thesis. Finally, I would like to thank Dr. James Holton and Dr. Uy-Loi Ly for serving on my committee as well.

I am grateful to my many colleagues at the UW who have made this a pleasant and productive work environment. In particular, Dr. Harry Edmon and Mr. David Warren have patiently dealt with my many computer-related questions, and Ms. Kathryn Stout and Mr. Don Atkinson have cheerfully and efficiently provided administrative support. I have enjoyed the friendship of Mr. Bart Brashers, Mr. James Mccaa, Mr. Stephen Marshall, Mr. Edward Flinchem and Mr. William Lipscomb

over these 5 years.

My parents, Mrs. Magda and Mr. Vidyut Pandya, and my sister, Ms. Mira Pandya, have been an unending source of support; it is impossible for me to imagine a more loving family. Finally, I would like to thank my wife, Dr. Amy Alter, for her unwavering affection, encouragement, and understanding; I feel lucky to be married to her.

DEDICATION

This thesis is dedicated to my grandfather, Mr. K. C. Pandya, who has selflessly supported the educational aspirations of friends and family alike. His generosity and strong commitment to education have been an inspiration to me.

Chapter 1

INTRODUCTION

Deep convection in the atmosphere is frequently observed to occur in close association with a pervasive region of mid-to-upper tropospheric stratiform cloudiness; an organization which is known as a mesoscale convective system (MCS). The heaviest precipitation, highest radar reflectivity, and most severe weather of the system are all associated with the actively convecting regions of the MCS, while the stratiform region is characterized by gentler, steady precipitation and weaker, but more spatially extensive, radar returns. Due to the large area covered by the stratiform anvil, however, its contribution to the system's total rainfall can be as high as 40% (Houze 1977; Gamache and Houze 1983). MCSs occur in both the tropics and in midlatitudes and produce climatologically significant precipitation in both regions. Over the great plains of North America, for example, precipitation from MCSs accounts for approximately half of the summer time precipitation (Fritsch *et al.* 1986). MCSs are also important local weather phenomena; many severe weather events, including tornadoes and severe straight line winds, flood producing rainfall, and damaging hail, are associated with thunderstorms embedded within MCSs.

The importance of the circulations in the stratiform region has motivated a number of investigators to examine the stratiform region carefully using both observations and numerical models. The kinematic and thermodynamic features in the the trailing stratiform region behind squall lines are especially well documented, in part due to the extremely

valuable PRE-STORM[1] data set. A review of squall line literature, presented in Chapter 2, demonstrates that although the circulation in the trailing stratiform region behind squall lines is well diagnosed, the underlying dynamical processes that determine the circulation are less well understood. Although investigators have proposed various dynamical causes for particular features of the circulation, there is no single dynamical process that has been applied universally to the various components of the circulation.

The thesis of this work is that the *principal kinematic and thermodynamic features of the mesoscale region around squall lines are the result of low-frequency gravity waves forced by the time-mean pattern of latent heat released and absorbed in the leading convective line*. This hypothesis provides a unifying dynamical explanation for the various features in the trailing region of squall lines. It rests on the distinction between the dynamical role buoyancy plays in the stratiform regions and convective regions of MCSs. Within the convective regions, buoyancy acts to accelerate parcels in their direction of motion; the convective updrafts are positively buoyant *plumes* that develop in response to the internal release and absorption of latent heat. In the stratiform region, however, buoyancy acts primarily as a restoring force and accelerates parcels in opposition to their direction of motion. This allows the propagation of gravity *waves* generated by the latent heat released and absorbed in the region of active convection. An important distinction between the dynamics of the plumes in the convective region and the gravity waves in the stratiform region involves the role of air parcel advection. Plumes propagate primarily through the physical transport of air parcels, whereas small-amplitude gravity waves can propagate without producing any net displacement of air parcels.

Observations have shown that deep convection can generate gravity waves (Miller and Sanders 1980). Conversely, gravity waves have also been implicated in triggering deep convection (Uccellini 1975; Ley and Peltier 1978, Koch *et al.* 1988). Less well understood is the extent to which deep convection and gravity waves can coexist and mutually interact

[1] PRE-STORM is the *P*reliminary *R*egional *E*xpirement for STORM-Central. STORM is the National *S*tormscale *O*perational *R*esearch *M*eteorology program.

in order to strengthen and organize mesoscale convective systems. A number of theoretical studies have attempted to elucidate the possible feedbacks between linear gravity waves and convection through analytic or semi-analytic wave-CISK formulations in which the thermal forcing from latent heating and cooling is parameterized as a function of the wave induced flow perturbations (Lindzen 1974; Raymond 1976 and 1984; Davies 1979; Xu and Clark 1984; Nehrkorn 1986). Attempts have also been made to identify and interpret the influence of gravity waves in numerical simulations of two-dimensional squall lines (Schmidt and Cotton 1990; Cram *et al.* 1992). More recently, Yang and Houze (1995a) have shown that the cellular vertical velocity in the stratiform region resembles gravity waves. This study, like much of the previous work, was directed toward isolating individual gravity wave modes that play a crucial role in the convection. In the case of wave-CISK, considerable efforts have been devoted to developing heating parameterizations and choosing basic-state environmental profiles that yield a spatial scale for the most unstable mode that agrees with the observations. In the numerical simulations attention has been devoted to features resembling monochromatic gravity waves since these are most easily identified as gravity waves (both by visual inspection and by quantitative comparison with linear wave theory through the evaluation of polarization and dispersion relations).

Recent investigations have demonstrated, however, that linear gravity waves generated by a steady heat source can cause disturbances that have little resemblance to the canonical picture of a monochromatic internal gravity wave (Bretherton 1988; Nichols *et al.* 1991; Pandya *et al.* 1993, Mapes 1993; Mapes and Houze 1995). An example of the flow in this type of disturbance is shown in Fig. 1.1, which was calculated using the Boussinesq equations linearized about a horizontally uniform basic state at rest. The heat source is confined to a compact region 10 km deep centered at $x = 0$ km (given by (6) in Nicholls *et al.* 1991), and, as shown in Fig. 1.1, it generates a circulation with low-level flow directed toward the heat source and an upper-level flow directed away from the heating. Since these are linear solutions in a basic state with no mean wind, the advection of momentum plays no role in the development of this circulation. The speed at which the leading edge of

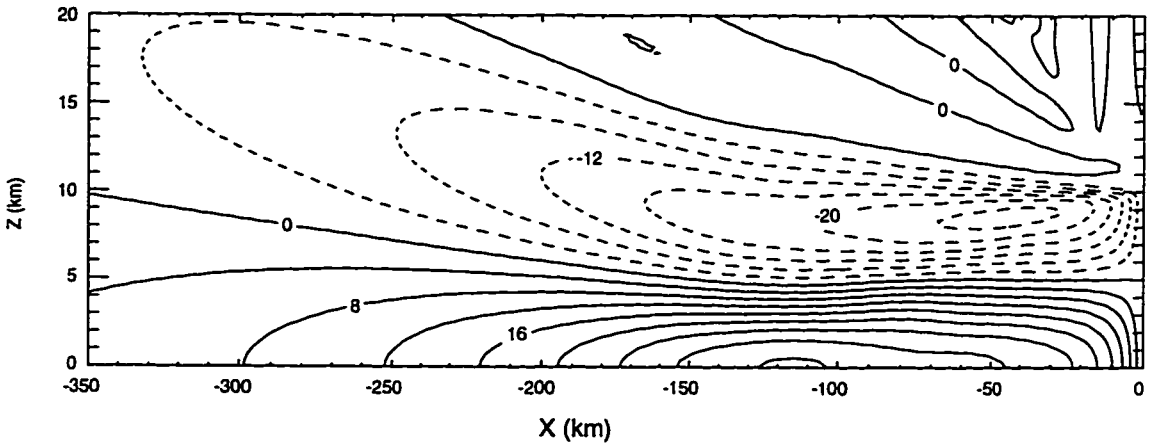

Figure 1.1. Horizontal velocity (contoured in 4 m s^{-1} intervals) at $t = 2$ hours generated by a compact heat source in a linear model.

the circulation propagates to the left is governed by a gravity-wave group velocity and is independent of the magnitude of the velocity extrema in the upper and lower branches of the flow. Some confusion may arise in applying the term gravity wave to the disturbance in Fig. 1.1, since the region behind the wave front is almost horizontally homogeneous and does not resemble a simple wave. If the heating were switched off, however, the disturbance would have a trailing edge propagating leftward at the same speed as the leading edge and would be easily recognizable as a wave pulse. Since the underlying dynamics are the same whether or not the heat source is switched off, we refer to the disturbance shown in Fig. 1.1 as a gravity wave.

Squall lines form in environments that are conditionally unstable. One might suppose, therefore, that any cloudy region within the leading line or trailing anvil might be statically unstable. In fact, most of the interior of the system is stably stratified, including much of the leading line. This can be seen in Figure 1.2, which is a contour plot of the Brunt-Väisälä frequency within a two-dimensional numerical simulation of a squall line. (Details of the numerical model used to generate this storm will be discussed in Chapter 3, along with a discussion of all the models used in this study.) In saturated regions, the conventional

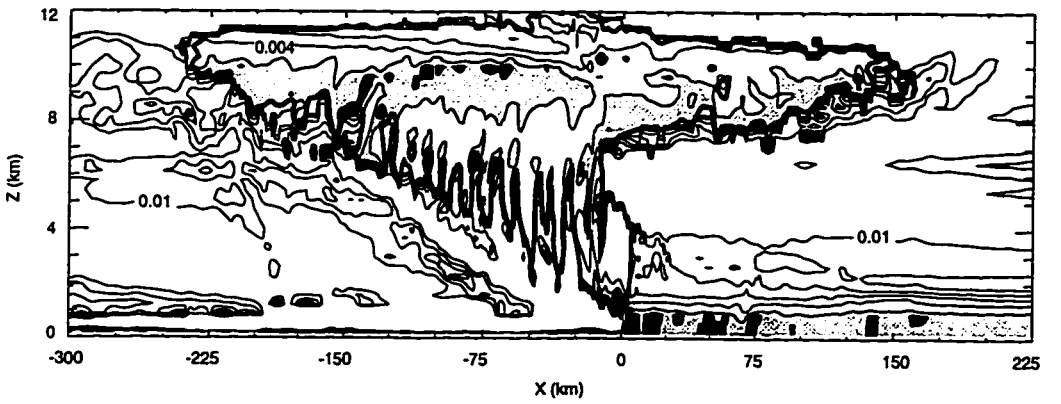

Figure 1.2. Brunt-Väisälä frequency (contoured in 0.002 s^{-1} intervals) in a numerically simulated squall line. Cloud outline is indicated by the heavy contour. Dark shading indicates statically unstable regions. Light shading appears where $N < 0.002\ s^{-1}$.

formula for the Brunt-Väisälä frequency was modified to take into account the effects of latent heat release on the static stability (Durran and Klemp 1982), in which case

$$N_m^2 = \begin{cases} g\left\{\frac{1+(Lq_s/RT)}{1+(\epsilon L^2 q_s/c_p RT^2)}\left(\frac{d\ln\theta}{dz}+\frac{L}{c_pT}\frac{dq_s}{dz}\right)-\frac{dq_w}{dz}\right\} & \text{if } q_v \geq q_s \\ g\left(\frac{d\ln\theta}{dz}\right) & \text{otherwise,} \end{cases} \tag{1.1}$$

where q_v is the mixing ratio of water vapor, q_s is the saturated mixing ratio of water vapor, and q_w is the mixing ratio of all hydrometeors.[2] The outline of the cloud, defined by regions in which the cloud liquid water mixing ratio exceeds 1.0 g kg^{-1}, is also plotted as the thick line in Fig. 1.2. The only persistent areas of negative Brunt-Väisälä frequency (which appear as darkly shaded regions) are in the well mixed boundary layer and in the low-level core of the main updraft. There are also a few small transient regions of negative N_m within the stratiform anvil, but Fig. 1.2 indicates that the bulk of the leading-line/trailing-stratiform system is stably stratified. Gravity waves can, therefore, propagate throughout essentially the entire system.

Chapter 4 will demonstrate that gravity waves do propagate throughout the stratiform

[2] L is the latent heat of vaporization for water, C_p is the specific heat of dry air at constant pressure, R is the ideal gas constant for dry air, ϵ is 0.622, T is the sensible temperature, and θ is the potential temperature.

region of MCSs and are responsible for the circulation outside of the convective regions. The gravity waves are forced by the time-mean thermal forcing in the leading convective line. This will be demonstrated by a detailed comparison of two nonlinear squall line simulations: one conventional cloud simulation with microphysics and a second "dry" simulation in which the circulation results from gravity waves generated by a steady pattern of heating and cooling that represents the latent heating and cooling of the leading convection. Mapes (1993) and Mapes and Houze (1995) also investigated the gravity waves generated by a steady forcing in an effort to understand the impact of convection on larger scale circulations. They examined the linear gravity waves generated by a fixed divergence profile (which is equivalent to a thermal forcing) in order to investigate how the large scale environment responds to an MCS. The dry simulation in Chapter 4 uses a similar approach except that it uses a more complicated thermal forcing to force nonlinear gravity waves within the MCS. Garner and Thorpe (1991) also performed expirements using specified thermal forcing to investigate the circulation within squall lines. They, however, used a time-varying thermal forcing which was related to the circulation around the convection.

In Chapter 5, the results of some sensitivity tests are discussed; these tests show that the gravity waves have a strong nonlinear component dependent on the formation of a low-level cold pool. Further tests show that the gravity waves exhibit a greater sensitivity to the thermal forcing that generates them than to the environment through which they propagate. Chapter 6 examines the results of some three-dimensional numerical simulations, and Chapter 7 is a summary of the major conclusions to be drawn from this research.

Chapter 2

REVIEW OF SQUALL LINE RESEARCH

Although many investigators have classified MCSs according to the evolution and structure of the embedded convection (e.g. Bluestein and Jain 1985; Blanchard 1990), a few investigators have classified MCSs according to the location of the stratiform cloud and precipitation relative to the embedded convection. (Houze *et al.* 1990; Loehrer and Johnson 1995). Houze *et al.* (1990) used 6 years of data from the NSSL[1] WSR-57 radar to examine the echo structure of 63 MCSs that occurred over Oklahoma. The MCSs they observed spanned a continuous spectrum of mesoscale organization, from those with large, irregular stratiform regions with randomly distributed regions of convection to more organized systems. Approximately 2/3 of the MCSs they observed showed an organization in which high reflectivity convective cells were arranged along a moving line and followed by a large region of stratiform cloudiness. Houze *et al.* (1990) referred to this organization as a leading-line/trailing-stratiform (LL-TS) structure. The LL-TS systems observed by Houze *et al.* (1990) were midlatitude systems, but squall lines with extensive trailing anvils have also been observed in the maritime tropics (e.g. Houze 1977; Gamache and Houze 1983; Houze and Rappaport 1984), in west Africa (e.g. Roux *et al.* 1984; Chong *et al.* 1987; Roux 1988), and over northern Australia (Rasmussen and Rutledge 1993).

2.1 Quasi-two-dimensional circulation

We can gain considerable insight into the circulation around real LL-TS MCSs by approximating the system as two dimensional. This fact has been exploited by a number of

[1] NSSL is the *N*ational *S*evere *S*torms *L*aboratories.

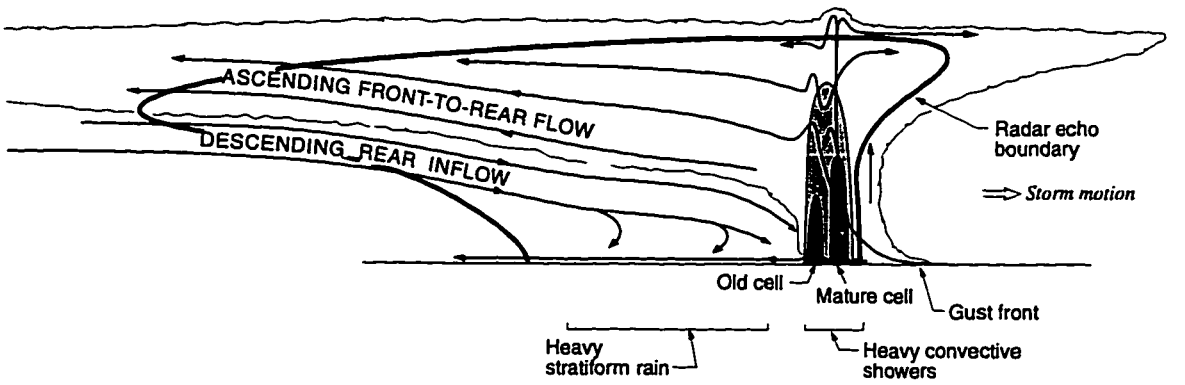

Figure 2.1. Conceptual model of a multicell squall line with trailing stratiform precipitation. The storm is viewed in a cross section perpendicular to the convective line (adapted from Houze *et al.* 1989).

numerical modeling studies which have reproduced many of the features observed in real squall lines using two-dimensional numerical simulations (e.g. Thorpe *et al.* 1982; Dudhia *et al.* 1987; Rotunno *et al.* 1988; Fovell and Ogura 1988; Lafore and Moncrieff 1989). A schematic diagram of the circulation and cloud structure in a conceptual two-dimensional model of a squall line is shown in Figure 2.1 (Houze *et al.* 1989), which depicts the circulation in a cross section taken normal to the leading convective line. Two regions of stratiform cloudiness (indicated by the thin scalloped line) are visible around the cellular leading line in Fig. 2.1: an extensive meso-β-scale trailing anvil in the mid-to-upper troposphere and a smaller leading anvil in the upper troposphere. The flow ahead of the squall line is front-to-rear, except at upper levels in the anvil, where the flow is rear-to-front (as indicated by the streamlines in the leading anvil). In a conceptual model of a squall line with trailing stratiform precipitation, Zipser (1977, see his Fig. 13) showed the flow behind the leading line arranged in three layers: an upper level front-to-rear flow, a midlevel rear-to-front flow (somewhat limited in extent) and a region of front-to-rear flow near the surface. The circulation features indicated in the trailing stratiform region of Fig. 2.1 are the "ascending front-to-rear flow" and the "descending rear inflow"; in addition a low-level front-to-rear at the surface is indicated by the streamlines. All of these flows are shown in

a reference frame translating with the storm, and are discussed in this chapter.

2.1.1 The leading convective line

Radar reflectivity cells, (indicated by the darker stippling) are shown within the leading line in this schematic diagram. The lifecycle of each cell is similar to the lifecycle of an isolated cell: cells form as high θ_e air from the boundary layer is forced above its lifting condensation level by convergence at the storms leading edge, the upward motion continues until the positive buoyancy from latent heat release is overcome by precipitation loading and/or the cell is effectively cut off from the high θ_e source by subsequent new cell development, and the cells decay in a precipitation driven downdraft (Byers and Braham 1949). As the cells age, they travel rearward through the storm, as indicated in Fig. 2.1 where the cell labeled "old cell" lies to the rear of the one labeled "mature cell". The principal dynamic process involved in the early life of the cells is that of buoyantly driven motion; the growing cells are positively buoyant plumes that develop in response to the internal release of latent heat. The importance of buoyant energy in driving convection is the basis for the predictive value of the skew-T or pseudo-adiabatic charts as well as diagnosed quantities like the convective available potential energy (CAPE).

Recent modeling work has suggested that the character of the convection is strongly influenced by the by the relative magnitudes of buoyant energy and energy in the vertical shear of the horizontal wind, which can be quantified by the bulk Richardson number. The bulk Richardson number is given by

$$R = \frac{CAPE}{.5\Delta u^2},$$

where Δu is the difference between the environmental winds at low and midlevels. The CAPE is the integrated positive buoyancy of a parcel ascending from the surface, given by

$$CAPE = g \int \frac{\theta_v(z) - \bar{\theta_v}(z)}{\bar{\theta_v}(z)} dz,$$

where $\theta_v(z)$ is the temperature of the ascending parcel, $\bar{\theta_v}(z)$ is the temperature of the environment, and the integration is performed for $\bar{\theta_v}(z) > \bar{\theta_v}(z)$ (*i.e.* from the level of

free convection to the level of neutral buoyancy.[2] Weisman and Klemp (1982) showed that storms in environments with $R > 40$ tended to evolve as multicellular storms in their model simulations. They also noted the tendency for real storms that form in environments characterized by large values of R to be multicellular.

Typically, the convection in midlatitude squall lines is observed to slant opposite the direction of storm motion (*i. e.* to the rear) with height. Thorpe *et al.* (1982) suggested that the low-level gust front in addition to causing the forced lifting of surface and near-surface air parcels to their level of free convection, might also influence the air parcels as they ascend freely beyond their level of free convection. Rotunno *et al.* (1988) considered the relative magnitude of the vorticity associated with the horizontal buoyancy gradient across the front of the low-level cold pool and the vorticity associated with the vertical shear of the horizontal wind. They found that when the cold pools vorticity exceeded that of the ambient shear, the updrafts in the convective region of their simulated storms slanted backward with height. Rotunno *et al.* (1988) noted that this state, although characterized by weaker updraft velocities than storms with vertical updraft velocities, had stronger stratiform circulations (including the upper level front-to-rear flow and midlevel rear inflow discussed later). The backward slanted convection occurred later in the storm's lifetime as the cold pool developed, and was long-lived and stable.

2.1.2 Ascending front-to-rear flow

In their analysis of the 22 May 1976 LL-TS system that passed over the mesonetwork of the NSSL in central Oklahoma, Ogura and Liou (1980) used composite and objective analysis techniques to determine the time-averaged structure in a vertical cross section through the squall line system. They observed an ascending front-to-rear flow (FTRF) extending at least 180 km behind the leading line. The FTRF, which joined the low-to-mid level front-to-rear flow located ahead of the line, rose sharply in the vicinity of the leading line, then more

[2] The level of neutral buoyancy is also called the equilibrium level.

gradually farther away. Ogura and Liou noted that u was approximately constant along the streamlines in the updraft, which might suggest that the FTRF is the result of air-parcels from ahead of the storm conserving their horizontal momentum as they rise in convective updrafts. Using single-Doppler radar to analyize the same storm, Smull and Houze (1985) noted prominent convective scale maxima in the FTRF and suggested that convective cell dynamics might contribute to the FTRF. In a subsequent dual-Doppler analysis, they were able to confirm that the FTRF accelerated as it crossed the convective region, and noted that the profile of vertical momentum flux could produce an acceleration consistent with that observed. LeMone (1983) and LeMone *et al.* (1984) argued, on the basis of observations of tropical systems, that the FTRF is the result of acceleration provided by a midlevel meso-γ-low that forms hydrostatically behind and beneath the positively buoyant air in the rearward slanting convective line. Observations (Ogura and Liou 1980; Smull and Houze 1987a, 1987b) confirm that the convection in the 22 May 1976 storm sloped rearward with height. Fovell and Ogura (1988) simulated the 22 May 1976 storm using a two-dimensional, non-hydrostatic cloud model and found that a largely hydrostatic low-pressure region formed behind and under the tilted leading line. Further, they attributed the rearward acceleration of the air-parcels that formed the FTRF to the pressure gradient associated with this low.

While the discussion so far has focussed on the flow behind the 22 May 1976 squall line, the FTRF has been observed in a number of LL-TS systems. The 10 June 1985 squall line, observed as part of the PRE-STORM field project, showed an FTRF that extended the length of the stratiform anvil (see Fig. 11 of Smull and Houze 1987b). Other PRE-STORM storms show an extensive FTRF as well: the 3-4 June storm (Stumpf and Johnson 1991) which had a fairly irregular leading line, and the 23-24 June 85 storm (Johnson and Bartels 1992). Betts *et al.* (1976) reported the existence of FTRF in the Venezuelan storms they analyzed, while Roux *et al.* (1984) and Roux (1988) reported FTRF in their analysis of squall lines with trailing stratiform precipitation observed over the Ivory Coast in Africa

during COPT 81.[3] The FTRF is also easily reproduced in cloud models (e.g. Lafore and Moncrieff 1988; Szeto and Cho 1994) and mesoscale models (e.g. Zhang and Gao 1989; Gao *et al.* 1990). Gao *et al.* (1990) determined that line-normal pressure gradients were the dominant term in the momentum budget of their simulated squall line, and thus essentially determined the entire circulation in the squall line including, in particular, the FTRF.

Another fairly ubiquitous feature of LL-TS systems is the low-level front-to-rear flow. Zipser (1969, 1977) noted that this feature was colder than the environment and attributed it to convective-scale saturated downdrafts, although he also suggested that it is augmented by mixing with mesoscale, unsaturated downdrafts. Smull and Houze(1987b) pointed out that the descending rear inflow could further augment the low-level cold pool as well. In numerical simulations by Rotunno *et al.* (1988) show, the midlevel air descending toward the surface in the rear inflow also contributed to the low-level front-to-rear flow.

2.1.3 Descending rear-to-front flow

Between the two layers of front-to-rear flow a midlevel "descending rear inflow" is indicated in Fig. 2.1. A midlevel intrusion of dry, low θ_e air was observed in the mature-to-decaying stages of tropical systems by Zipser (1969, 1977). Smull and Houze (1987b) reviewed 18 LL-TS MCSs in both the tropics and midlatitudes and classified them according to the strength of the midlevel rear inflow (RI). They found three cases exhibited a strong, jet-like RI that extended from the trailing edge of the stratiform anvil to the systems leading line and had speeds that exceeded 15 m s^{-1}. Ten of the 18 cases they studied were labeled "stagnation zone" cases, with a RI of less than 5 m s^{-1}. In some of these cases, the midlevel flow never actually became rear-to-front, instead there was a broad mid-level band of very weak front-to-rear flow with stronger front-to-rear flow above and below. Smull and Houze also noted that the FTRF in these systems was weaker than the FTRF in the strong rear inflow cases. Stagnation zone cases were dominated by, but not restricted to tropical

[3] COPT 81 is *Convection Profonde Tropicale* 1981.

systems, while all 3 strong RI cases occurred in midlatitudes. The RI in the strong cases was vertically compact and centered at 550 mb, while the stagnation zone cases showed a broad region of inflow centered around 700 mb. Five additional cases were documented by Smull and Houze with inflows between 5 and 10 m s^{-1}. These were called weak inflow cases and as a group exhibited no regular structure.

The 10-11 June 1985 Squall line observed during PRE-STORM and cited by Smull and Houze (1987b) as an example of the strong RI case had a strong RI extending more than 200 km behind the gust front (see Figs. 11b and 11d of Smull and Houze 1987b). The RI shows a bimodal velocity structure, with an area of slow velocities located between two regions of fast velocities: one at the rear of the stratiform region and another just behind the leading convective line. The 28 May 1985 LL-TS system, also presented by Smull and Houze (1987b) as an example of strong RI, had a bimodal RI as well; the RI was strongest at the trailing edge and strong just behind the leading line and weak in between. In their analysis of the 22 May 1976 squall line (the third of the strong RI cases presented by Smull and Houze 1987b), Ogura and Liou (1980) showed a bimodal RI with a maximum exceeding 10 m s^{-1} at 135 km behind the line, and a second, much weaker region of RI 50 km behind the leading line. In between these two regions of RI the flow reversed and was front-to-rear. Smull and Houze (1985), in their single-Doppler analysis of the same storm, also showed an upper level maximum in RI at the back edge of the anvil separated from a lower-level region of RI closer to the leading line by a region of front-to-rear flow, although they noted that this storm evolved toward a more continuous RI with time. Klimowski (1994) used dual-Doppler analysis techniques to construct a series of cross sections through the 28-29 June 1989 LL-TS system that passed through the North Dakota Thunderstorm Project observational network. These cross sections show that the RI varied significantly in time and space, but was nearly always bimodal with the strongest RI at the trailing edge of the system and another region of strong RI near the leading line. In some of the cross-sections, the two regions of strong RI are separated by areas of front-to-rear flow.

Stumpf and Johnson (1991) used dual-Doppler radar observations to analyize the 3-4 June 1985 MCS that was observed during the Oklahoma-Kansas PRE-STORM. They found that the RI in this system descended abruptly to the surface at the rear edge of the stratiform region and never penetrated to the leading line. This system differed from the conventional LL-TS structure in that it consisted of two convective lines: one to the north oriented NE-SW and a line to the south oriented N-S. This storm was also unique because it formed as a cold-frontal MCS, which meant that there was a thermally modulated large scale structure to the ambient flow. Johnson and Bartels (1990) observed a more conventional LL-TS MCS, the 23-24 June 1985 PRE-STORM system, and documented a rapidly descending RI at the rear of the stratiform region that also didn't penetrate into the interior of the storm.

Smull and Houze (1987b), noting the bimodal nature of the RI, suggested that two separate mechanisms may have acted to produce the RI, one at the leading edge and one in the stratiform region. Smull and Houze (1987a) used dual-Doppler radar analysis to diagnose convective scale maxima in the RI within the leading line of the 22 May 1976 system. This and their estimation of the forward acceleration predicted by the vertical convergence of horizontal momentum flux in the convective updrafts and downdrafts led them to suggest that processes within the convective line were responsible for accelerating midlevel air forward. LeMone (1983) and LeMone *et al.* (1984) found similar accelerations in their analysis of tropical systems and attributed them to a hydrostatically induced pressure minimum behind and beneath the backward slanting, positively buoyant convective updrafts; they invoked the same feature to explain the generation of the FTRF. Such a pressure minimum has been observed in the 10-11 June 1985 midlatitude squall line observed by Biggerstaff and Houze (1991a and 1991b) and in the 6-7 May 1985 MCS observed by Brandes (1990) as part of PRE-STORM. A meso-γ-scale low has also been produced in numerical simulations of idealized midlatitude squall lines (Szeto and Cho 1994). In their numerical simulations of the 22 May 1976 squall line Fovell and Ogura (1988) attributed the forward acceleration of midlevel air to a hydrostatic pressure minimum that formed to

the rear of the backward sloping leading line. Klimowski's (1994) analysis of the development of the 28-29 June 1989 squall line revealed that the RI was initiated near the high-reflectivity cores of the leading line and spread rearward with time. Klimowski interpreted these observations as evidence that the RI was primarily the result of processes associated with the strong convection at the leading edge of the system. Lafore and Moncrieff (1989) used two-dimensional numerical simulations based on storms observed in West Africa during COPT81 to conclude that horizontal potential temperature gradient across the leading line, due in part to the latent heat released in the convective region, generated a horizontal line-parallel vorticity that lead to the development of the RI. Weisman (1992) asserted that the rearward tilt to the convective line in his numerical simulations produced horizontal gradients of buoyancy that drew midlevel air into the system.

The presence of maximum RI at the back edge of the stratiform anvil has led a number of investigators to suggest that processes tied to the production of the stratiform precipitation might be important in understanding the RI. Smull and Houze (1987b) suggested that the part of RI at the back edge of the stratiform region forms as midlevel air is drawn into the system from the rear by a midlevel mesolow located there. The midlevel low is thought to be a hydrostatic response to latent heating above and evaporative cooling below (Brown 1979; Leary and Houze 1979). Stumpf and Johnson (1991) noted that the RI in the 3-4 June 1985 storm (which never penetrated the storm's interior) was strongest under the most extensive stratiform anvil, and nonexistent where there was no anvil. This led them to hypothesize that the RI in that case depended on precipitation processes within the stratiform anvil. Lin and Johnson (1994) suggested that the RI in the 26-27 June 1985 PRE-STORM system was the result of microphysical processes within the stratiform region. Leary and Houze (1979) suggested that ice processes specifically could aid in the production of a mid-level mesolow and hence contribute to the RI. Yang and Houze (1995b) concluded that the addition of a bulk-ice microphysical parameterization to a warm-rain cloud model leads to a more realistic RI. Gallus and Johnson (1995a and b) performed a series of simulations of the stratiform region of the 10-11 June 1985 squall line in which they specified

one-dimensional profiles of thermal forcing and hydrometeor advection meant to represent inputs from the convective region at the lateral boundary of a two-dimensional kinematic cloud model. They concluded that ice processes within the stratiform region were an important dynamical contribution to the development of the rear inflow.

A few studies have suggested that synoptic scale processes may also help to force the RI. Zhang and Gao (1989) attributed the RI in their mesoscale model simulation of the 10-11 June 1985 squall line with trailing anvil to both large scale baroclinicity and stratiform processes. Brandes (1990) suggested that the RI at the rear of the 6-7 May 1985 system was the result of both large-scale westerlies behind the storm and convective scale processes in the system's interior.

2.1.4 Mesoscale vertical motions

In the 22 May 1976 squall line, Ogura and Liou (1980) reported a broad region of upward motion above 550 mb that extended 180 km behind the leading line. Beneath this, a narrower region of downward vertical motion was diagnosed (see their Fig. 13). Biggerstaff and Houze (1991a) observed a similar broad mesoscale updraft overlying a smaller, but still mesoscale, downdraft in the the tailing anvil of the 10-11 June 1985 squall line. They determined that the mesoscale updraft scaled with the size of the stratiform cloud and suggested that the updraft was driven by positively buoyant air advected rearward from the convective towers. Biggerstaff and Houze also found the mesoscale downdraft scaled according to the size of the stratiform precipitation region, which suggests that the downdraft is driven by microphysical processes, chiefly melting and evaporation. In modeling studies, Brown (1979) attributed the downdraft to evaporative cooling of air beneath the anvil while Leary and Houze (1979) suggested that ice processes could further amplify this circulation.

2.2 *Three-dimensional circulations*

Radar observations of squall lines reveal along-line variability that cannot be accounted for in the quasi-two dimensional analysis presented in the previous section. Nolen (1959) referred to sinusoidal variations in the position of the leading line as "line-wave echo patterns", and Fujita (1978) noted the forward bowing of the leading line in certain locations. The tendency for convection to be most intense in the southern end and the stratiform region to dominate the northern end has been noted in some storms and is discussed in Section 2.2.1. Section 2.2.2 discusses the presence of a midlevel vortex in the trailing stratiform anvil.

2.2.1 *Symmetric versus asymmetric structures*

Approximately 26% of the LL-TS systems documented in the climatological study of Houze *et al.* (1990) showed an arc shaped leading line with the stratiform region centered symmetrically behind it. A schematic of this symmetric LL-TS organization is shown in plan view in Fig. 2.2a. The leading line in these systems is generally a few hundred kilometers long and oriented NE-SW with the most vigorous convection in the center of the line. The stratiform region is concave with its apex directly behind the strongest convection (Smull and Houze 1985; Smull and Houze 1987b; Jorgensen and Smull 1993). Stumpf and Johnson (1991) observed an enhanced reflectivity gradient at the rear of the trailing stratiform echo co-located with a maximum in the rear inflow and argued that the rear inflow caused the tightened reflectivity gradient by bringing dry midlevel air that evaporated the hydrometeors into the system.

The leading line in Fig. 2.2a is broadly similar in appearance to the "bow echoes" described by Fujita (1978). Fujita noted the tendency for bow echoes to be associated with microbursts, and other investigators have reported damaging, straight line winds at the apex of the bow (e.g. Nolen 1959; Hamilton 1970). "Derechoes", straight-line wind gusts exceeding 23 m s^{-1} with a major axis of length greater than 400 km, have been associated

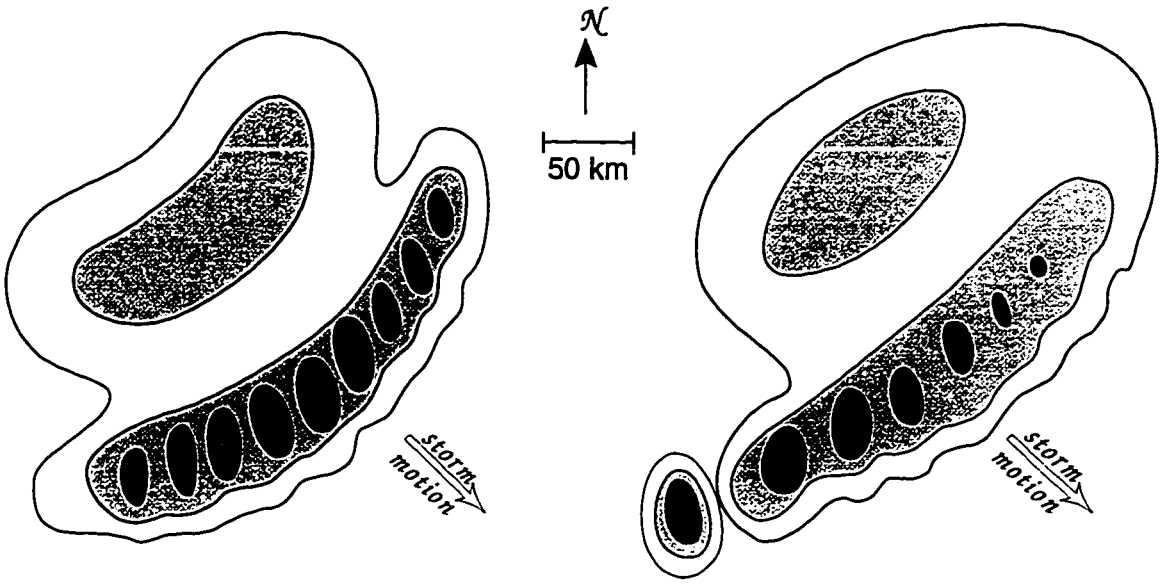

Figure 2.2. Conceptual model of two kinds of leading line/trailing anvil mesoscale convective systems: (a) symmetric and (b) asymmetric. Radar reflectivity is indicated by stippling. Adapted from Houze *et al.* (1980).

with bow-echo systems as well (Johns and Hirt 1987).

In their radar analysis of the 22 May 1976 system, Smull and Houze(1985) noted a relatively narrow maximum in RI appeared at the back edge of the trailing anvil directly behind the apex of a bow in the leading line. Jorgenson and Smull (1993) used airborne dual-Doppler radar to analyze a squall line that occurred on 28 May 1991, and showed that the most intense RI occurred behind the bowed portion of the leading line. Observations of the 28 May 1976 (Smull and Houze 1987b) storm, the 6-7 May 1985 storm (Brandes 1981), and the 2 August 1981 storm observed as a part of the CCOPE[4] field program also show the strongest RI behind a bow in the leading line (Schmidt and Cotton 1989). In Weisman's (1992) simulation of bow echoes, the strongest RI occurred behind the apex of the bow. Weisman attributed the strong RI to the action of vortices that formed at the

[4] CCOPE is the *C*ooperative *C*onvective *P*recipatation *E*xpirement.

line's ends and acted as a vortex couplet to accelerate the flow between them. Skamarock *et al.* (1994) also showed the strongest RI behind the bowed portion of the line in their three-dimensional simulations of LL-TS systems.

Approximately 38% of the LL-TS MCSs had the stratiform region placed asymmetrically behind the leading line, as shown in Fig. 2.2b. The leading line in asymmetric systems is oriented NE-SW, as in the symmetric systems, but the convection is strongest at the SW end of the line and the stratiform region is located to the NE and behind the line. Pedgley (1962) developed a conceptual model for squall lines that is very similar to the asymmetric schematic presented in Fig. 2.2b based on his observations of an English MCS. The 10 June 1985 PRE-STORM squall line is a good example of the asymmetric case, with a large stratiform anvil located to the the NW of the most vigorous convection in the leading line (see Fig. 10b of Smull and Houze 1987b). Houze *et al.* (1990) point out, however, that the most of the LL-TS systems did not completely match either the symmetric or asymmetric model, but that the systems occurred with a continuous spectrum of structures bounded by the symmetric and asymmetric case.

Recent work has suggested that the two classes of LL-TS convective systems presented in Fig. 2.2, symmetric and asymmetric, do not represent two completely distinct kinds of storms. Instead, the two classes seem to correspond to stages in the lifetime of the storm. Loehrer and Johnson (1995) examined 16 storms that passed over the PRE-STORM mesonetwork in Oklahoma and Nebraska, and found that 75% of the systems resembled the asymmetric schematic by the time they left the observational domain. Many of these same systems, however, exhibited a symmetric structure when they entered the domain or formed within the domain, leading Loehrer and Johnson (1995) to conclude that LL-TS systems evolve from an initially symmetric structure toward an asymmetric structure. Numerical simulations of three-dimensional squall lines by Skamarock *et al.* (1994) show a similar evolution from symmetric to asymmetric structure, but only when the Coriolis force is included in the governing equations.

2.2.2 *The mesoscale convective vortex*

Three distinctly horizontal mesoscale circulations are associated with mature MCSs exhibiting rotational characteristics: a low-level divergent flow (e.g. Fujita 1959), a mid-level cyclonic flow known as the mesoscale convective vortex (MCV)[5], and an upper-level anticyclonic, divergent outflow (e.g. Fritsch *et al.* 1981). Bartels and Maddox (1991) analyzed 24 MCSs (half of which met the MCC size criteria) and found that the MCV had a typical diameter of 150-300 km, and an average lifetime of 12 hours. The MCVs tended to be located in the mesoscale updraft or on the boundary between the mesoscale up and downdrafts, between 2.5 to 4 km AGL. Brandes (1990) suggested that the MCVs are inherently stable, and may contribute to the longevity of the MCS they are found in. MCVs can sometimes be inferred from radar, where they are associated with a hook-like pattern in the trailing stratiform region (e.g. Brandes 1990; Johnson and Bartels 1992; Jorgenson and Smull 1993).

MCVs show a lot of variation in nearly all their properties. They range in size from tens of kilometers like the MCV documented by Verlinde and Cotton (1990) in their study of 16-17 PRE-STORM MCS, to a diameter greater than 400 km (Bartels and Maddox 1991). Although some MCV live long enough to be inferred from the midlevel cloud patterns observed via satellite after the upper level anvil has dissipated (Johnston 1981), Biggerstaff and Houze (1991b) observed regions of cyclonic vorticity that lasted less than 5 hours. Johnson and Bartels (1992) looked at a particularly deep MCV (extending all the way to 8 km AGL) and concluded that although the thermodynamic structure was complicated, the MCV was basically warmer than its environment. Brandes (1990) found the MCV accompanying the 6-7 May MCS to be cooler than the environment, and Brandes and Zeigler (1990) used dual-Doppler radar to show that this MCV occurred in a mesoscale downdraft. Zhang (1992) used a three-dimensional mesoscale model to show that the MCV associated with the 10 June squall line (observed by Biggerstaff and Houze 1991b) was a

[5] This feature has also been called the mesoscale cyclonic vortex.

cold-core vortex that occurred in a region of downward air motion.

In their climatological study of MCVs, Bartels and Maddox (1991) argued that the convergence/stretching of planetary vorticity was more important to the generation of cyclonic vorticity in the MCV than either the tilting or advection terms of the quasi-vorticity equation. Johnson and Bartels (1992), in their analysis of the MCV accompanying the 23-24 PRE-STORM June 1985 MCS, suggested that the midtropospheric convergence due to the mesoscale updraft-downdraft couplet in the stratiform region amplified the MCV as the MCS itself decayed. Johnson and Bartels (1992) also pointed out, however, that the MCV in this case was associated with a pre-existing short wave trough. Brandes (1990) argued that the strong midlevel cyclonic vorticity of the 6-7 May 1985 PRE-STORM MCV was the result of convergence into the mesoscale downdraft and that the weaker low-level vorticity arose from the tilting of horizontal vorticity associated with the low-level potential temperature gradient caused by the spreading cold pool. Brandes and Ziegler (1992) concluded that a significant amount of the vorticity amplified by the mesoscale downdraft was first created by tilting the horizontal vorticity. Verlinde and Cotton (1990) determined that tilting of horizontal vorticity in convective updrafts created vertical vorticity which was later amplified by convergence in the 16-17 May 1985 PRE-STORM MCV. Biggerstaff and Houze (1991b), in contrast, analyzed the vorticity budget of the 10-11 June squall line and found that the tilting terms dominated the stretching terms by a factor of five. Zhang (1992) asserted, on the basis of his numerical simulations of the same system, that stretching of absolute vorticity from the synoptic scale short wave trough dominated the early growth of the MCV, tilting became increasingly important as the RI developed, and stretching again became the dominant term in the decaying stage. Skamarock *et al.* (1994) simulated a realistic MCS in their simulation and suggested that the convergence of large scale planetary vorticity is crucial to the formation of the MCV, but that tilting of ambient and baroclinically generated horizontal vorticity is not negligible.

Fujita (1978) suggested that cyclonic vortex that has since come to be called the MCV might be part of a vortex couplet, with an anticyclonic vortex forming to the south. Weis-

man (1992), in his three-dimensional numerical simulation of bow echoes, noted the presence of a vortex couplet, with a cyclonic vortex to the north and an anticyclonic vortex to the south. Skamarock *et al.* (1994) found that the inclusion of the Coriolis force in numerical simulations favored the development of the cyclonic member of the vortex pair. Until recently, however, observational evidence of the anticyclonic component of the vortex couplet has been scarce. Smull and Weisman (1993) reported a vortex pair in their analysis of the 23 May 1991 bow echo, which was observed using airborne Doppler radar. Scott and Rutledge (1995) reported on the existence of a weak anticyclonic vortex to the south of a much larger cyclonic vortex in their analysis of the 28 May 1985 asymmetric LL-TS MCS observed during PRE-STORM.

Chapter 3

DESCRIPTION OF NUMERICAL MODELS

Three numerical models were used in this study: a two-dimensional Boussinesq linear model, a two-dimensional incompressible fully nonlinear model, and a three-dimensional incompressible fully nonlinear nested grid model. The linear model was developed by the author and is described in detail in Section 3.1, and the two and three-dimensional nonlinear models are described in Sections 3.2 and 3.3, respectively. These models are pre-existing numerical models that were chosen for their availability to the author and modified for this study.

3.1 The linear model

The linear model was used to investigate the extent to which the gravity waves that determine the circulation in the stratiform region of MCSs are linear. The physical process investigated by the linear model is that of a stratified fluid responding to a pattern of infinitesimal heating and cooling. This physical system is described by the incompressible linearized two-dimensional Boussinesq equations. Only two dimensions were used in order to simplify the computations and to facilitate comparison to the two-dimensional nonlinear simulations. The Boussinesq approximation, in which the density is considered constant except where it is coupled to gravity in the vertical momentum equation, provided further simplification. It is an acceptable approximation in the troposphere, where the variation of density with height has a small dynamic effect. The constraint of incompressibility was chosen to avoid explicit accounting of sound waves, which are not important to the mesoscale circulation that develops around squall lines.

3.1.1 Basic equations

In a horizontally uniform basic state with a mean wind of $\bar{U}(z)$ and stability $N(z)$, the two-dimensional incompressible Boussinesq equations are

$$\left(\frac{\partial}{\partial t}+\bar{U}(z)\frac{\partial}{\partial x}\right)u'+w\frac{d\bar{U}}{dz}+\frac{1}{\rho_o}\frac{\partial p'}{\partial x}=0$$

$$\left(\frac{\partial}{\partial t}+\bar{U}(z)\frac{\partial}{\partial x}\right)w'+\frac{1}{\rho_o}\frac{\partial p'}{\partial z}=b$$

$$\left(\frac{\partial}{\partial t}+\bar{U}(z)\frac{\partial}{\partial x}\right)b+w'N^2(z)=Q(x,z)$$

$$\frac{\partial u'}{\partial x}+\frac{\partial w'}{\partial z}=0,$$

where Q represents the thermal forcing, u' is the perturbation horizontal wind, w' is the perturbation vertical velocity, and b is the buoyancy. These equations can be combined to give

$$\left(\frac{\partial}{\partial t}+\bar{U}(z)\frac{\partial}{\partial x}\right)^2\left(\frac{\partial^2 w'}{\partial z^2}+\frac{\partial^2 w'}{\partial x^2}\right)-\frac{d^2\bar{U}}{dz^2}\left(\frac{\partial}{\partial x}+\bar{U}(z)\frac{\partial w}{\partial x}\right)\frac{\partial w'}{\partial x}+$$

$$N^2(z)\frac{\partial^2 w'}{\partial x^2}=\frac{\partial^2 Q(x,z)}{\partial x^2}. \tag{3.1}$$

Analytic and quasi-analytic solutions to (3.1) can be found with the aid of some additional approximations. Nicholls *et al.* (1991) obtained quasi-analytic expressions for u', w', θ' and p', by choosing $Q(x,z)$ to be analytic and separable in x and z, considering an environment in which $N(z)=N_0$ and $U(z)=0$, and applying the hydrostatic approximation. Lin and Smith (1988) and Bretherton (1988) used Green's functions to obtain quasi-analytic solutions for w' when $N(z)=N_0$ and $U(z)=U_0$. These techniques have two principal disadvantages: they are useful only in vertically uniform mean states, which aren't representative of real world convection, and they involve integrations and special functions which must be evaluated to gain physical insight. The integration and evaluation of the special functions can be nontrivial and a potential source of significant error as pointed out in Pandya *et al.* (1993).

Alternatively, (3.1) can be integrated numerically. Unlike the approaches that aim for analytic or quasi-analytic solutions, the numerical integration of (3.1) allows arbitrary vertical structure in both the mean wind and the applied heating. One might suppose the that numerical model would produce an output less amenable to direct physical insight than an analytic or quasi-analytic solution; in fact, the numerical solution output is directly available for graphical display without the difficult special programming necessary to evaluate the integrations and special functions in that often appear in analytic or quasi-analytic solutions.

3.1.2 Numerical integration

The numerical solution of (3.1) begins, like many of the analytic solutions, by taking the Fourier transform in x, giving

$$\left(\frac{\partial^2}{\partial t^2} + 2ik\bar{U}\frac{\partial}{\partial t} - \bar{U}^2k^2\right)\left(\frac{\partial^2\hat{w}}{\partial z^2} - k^2\hat{w}\right) -$$

$$\frac{d^2\bar{U}}{dz^2}\left(ik\frac{\partial\hat{w}}{\partial t} - \bar{U}k^2\hat{w}\right) - N^2k^2\hat{w} = -k^2\hat{Q}, \tag{3.2}$$

where $\hat{w}$ is the horizontal Fourier Transform of w' and k is the horizontal wavelength. The numerical integration of (3.2) is done by first approximating (3.2) by the finite difference equation

$$\delta_t^2\delta_z^2\hat{w} + 2\bar{U}ik\delta_{2t}\delta_z^2\hat{w} - k^2\delta_t^2\hat{w} - 2\bar{U}ik^3\delta_{2t}\hat{w} - ik\frac{\partial^2\bar{U}}{\partial z^2}\delta_{2t}\hat{w} =$$

$$\bar{U}^2k^2\left(\delta_z^2\hat{w} - k^2\hat{w}\right) - \bar{U}k^2\frac{d^2\bar{U}}{dz^2}\hat{w} + N^2k^2\hat{w} - k^2\hat{Q}, \tag{3.3}$$

where $\delta_{nz}f$ is the centered finite difference operator defined such that

$$\delta_{nz}f(z) = [f(z + n\Delta z/2) - f(z - n\Delta z/2)]/(n\Delta z),$$

and, from the definition of δ_{nz},

$$\delta_z^2 f = \delta_z(\delta_z f) = \frac{f(z+\Delta z) - 2f(z) + f(z-\Delta z)}{(\Delta z)^2}.$$

Expanding (3.3) and grouping like terms gives an equation of the form

$$A\hat{w}_{m+1}^{n+1} + B\hat{w}_m^{n+1} + C\hat{w}_{m-1}^{n+1} = F, \tag{3.4}$$

where

$$A = C = \gamma = -1 - ik\Delta t\bar{U} + k^2\Delta t^2\frac{\bar{U}^2}{2},$$

$$B = -2\gamma - k^2\Delta z^2\gamma + \frac{1}{2}\Delta t\Delta z^2\frac{d\bar{U}}{dz},$$

and

$$F = k^2\Delta t^2\hat{Q} - k^2\Delta t^2N^2w_m^n + k^2\left(2w_m^n - w_m^{n-1} + ik\Delta t\bar{U}w_m^{n-1} + \frac{1}{2}k^2\Delta t^2\bar{U}^2w_m^{n-1}\right) -$$

$$2\delta_z^2w_m^n + \delta_z^2w_m^{n-1}\left(1 - ik\Delta t\bar{U} - k^2\Delta t^2\frac{\bar{U}^2}{2}\right) + \frac{d^2\bar{U}}{dz^2}\left(k^2\Delta t^2\bar{U}w_m^n + \frac{1}{2}k\Delta tw_n^m - 1\right)$$

The subscripts here refer to the vertical level (*i. e.* $\hat{w}_m = \hat{w}(m\Delta z)$ where Δz is the vertical grid spacing), while the superscripts refer to time.

Equation (3.4) can be applied for $m = 2$ to nz-1 to construct the inner rows of an nz by nz matrix. The complication arises in the first and last row of the matrix, (*i.e.* where m =1 and $m = nz$). At $m = 1$, for example, (3.4) requires knowledge of w_0^{n+1}. A rigid lower boundary at the surface requires $\hat{w}_0^{n+1} = 0$. The upper boundary is treated using a radiation condition similar to that of Klemp and Durran (1983) and Bougeault (1983),

$$\left(\frac{\partial}{\partial t} + i\bar{U}k\right)\frac{\partial w}{\partial z} = -|k|N\hat{w}, \tag{3.5}$$

which allows only upwardly propagating waves and therefore represents an open upper boundary. Although (3.5) is strictly true only for hydrostatic waves, the waves are sufficiently close hydrostatic along the upper boundary that this condition works well.

A standard trapezoidal finite-difference can be used to approximate (3.5) giving,

$$\delta_t\left(\frac{\partial\hat{w}}{\partial z}\right) + ik\bar{U}\langle\left(\frac{\partial\hat{w}}{\partial z}\right)\rangle_t = -|k|N\langle\hat{w}\rangle_t, \tag{3.6}$$

where $\langle f\rangle_t$ is an averaging operator defined such that

$$\langle f\rangle_{nt} = [f(t + \Delta t) + f(t - (n-1)\Delta t)]/2.$$

Applying (3.6) at the point $m = nz$ and rearranging gives

$$\hat{w}_{nz+1}^{n+1}\left(1+\frac{1}{2}ik\Delta t\bar{U}\right) = \hat{w}_{nz}^{n+1}\left(-|k|N\Delta t\Delta z\right) + \hat{w}_{nz-1}^{n+1}\left(1+\frac{1}{2}ik\Delta t\bar{U}\right) +$$

$$\hat{w}_{nz+1}^{n}\left(1-\frac{1}{2}ik\Delta t\bar{U}\right) + \hat{w}_{nz}^{n}\left(-|k|N\Delta t\Delta z\right) + \hat{w}_{nz-1}^{n}\left(-1+\frac{1}{2}ik\Delta t\bar{U}\right),$$

which can be used to replace $\hat{w}_{nz+1}^{n+1}$ in (3.4) applied at $m = nz$. Although this expression is implicit, it makes use of only $\hat{w}_{nz}^{n+1}$ and $\hat{w}_{nz-1}^{n+1}$, and so preserves the tri-diagonal matrix form of (3.4). After finding $\hat{w^{n+1}}$ using a standard tridiagonal algorithm, a fast Fourier Transform routine can be used to find w' at time $n+1$.

The linear nature of the basic equations allows the numerical integration to proceed in a straight forward way. There is no need for any spatial smoothing since the linearity of this model precludes the possibility of nonlinear instability. The absence of an energy cascade to small scales means there is also no need to parameterize subgrid scale processes like eddy diffusion. Open lateral boundaries can be approximated by a using a sufficiently large periodic domain.

3.1.3 Stability and phase speed error

The stability of the numerical integration scheme given by (3.3) is difficult to analyze directly. We can gain some insight, however, by considering the simpler case of a hydrostatic atmosphere with a mean wind of zero and no thermal forcing. Under these conditions, (3.2) reduces to

$$\frac{\partial^2}{\partial t^2}\left(\frac{\partial^2 \hat{w}}{\partial z^2}\right) - N^2k^2\hat{w} = 0, \tag{3.7}$$

Plugging in an assumed solution of the form $\hat{w} = \hat{w}_o \exp\left[i\left(mz - \omega t\right)\right]$, gives a horizontal dispersion relation of

$$C_r = \pm N/m, \tag{3.8}$$

which implies that horizontal phase speed (and horizontal group velocity since the two are identical for hydrostatic waves) is independent of the horizontal wavenumber k. Thus, there is no dispersion of horizontal wavelengths.

Applying the type of finite difference approximation of the time derivative used in (3.3) to (3.7) gives,

$$\frac{1}{\Delta t^2}\left[\left(\frac{\partial^2 w}{\partial z^2}\right)^{n+1} - 2\left(\frac{\partial^2 w}{\partial z^2}\right)^{n} + \left(\frac{\partial^2 w}{\partial z^2}\right)^{n-1}\right] - N^2 k^2 w^n = 0. \tag{3.9}$$

Like the leapfrog scheme, the finite difference scheme shown above uses the middle time level for the terms undifferentiated in time; it will be referred to as the "quasi-leapfrog scheme". Substituting an assumed solution $\hat{w} = \hat{w}_o \exp[i(mz - \omega t)]$ into 3.9 gives, after some rearranging,

$$m^2[2\cos(\omega\Delta t) - 2] - N^2 k^2 \Delta t^2 = 0. \tag{3.10}$$

For waves that are well resolved in time (*i. e.* $\omega\Delta t \ll 1$) this gives a dispersion relation of

$$C_{lf}^2 = C_r^2\left(1 + \frac{1}{12}C_r^2 k^2 \Delta t^2 + \ldots\right), \tag{3.11}$$

where only terms to order Δt^2 have been kept in the expansion of the cosine term. Comparing (3.11) to (3.8) reveals that the quasi-leapfrog scheme slightly overestimates the phase speed of the waves and introduces an erroneous dispersion of horizontal wavelengths.

Rearranging (3.10) gives

$$\cos(\omega\Delta t) = 1 - \frac{N^2 k^2 \Delta t^2}{2m^2}.$$

The frequency, ω, will be real and introduce no growing mode into the solution provided

$$0 < \frac{N^2 k^2 \Delta t^2}{m^2} < 4.$$

Since the left hand inequality is obviously satisfied in any stably stratified fluid, the stability criteria for the quasi-leapfrog scheme comes from applying right hand inequality to the waves with the largest possible k, the $2\Delta x$ waves. Thus, the stability criteria for the quasi-leapfrog scheme is

$$\frac{C_r \Delta t}{\Delta x} < \frac{2}{\pi}. \tag{3.12}$$

The stability criteria for the quasi-leapfrog scheme limits the maximum time step one can take in integrating (3.1). A second scheme, called the "quasi-trapezoidal" scheme was

constructed to avoid the constraints on the step size imposed by the stability criteria of the leapfrog scheme. Like the trapezoidal scheme, it uses a time average of the terms undifferentiated in time to be unconditionally stable. Applying the quasi-trapezoidal scheme to (3.7) gives

$$\delta_t^2 \left(\frac{\partial^2 \hat{w}}{\partial z^2} \right) - \langle N^2 k^2 \hat{w} \rangle_{2t} = 0. \tag{3.13}$$

Plugging in an assumed solution of the form $\hat{w} = \hat{w}_o \exp[i\,(mz - \omega t)]$ and doing some algebra gives

$$\cos(\omega \Delta t) = \frac{2m^2}{2m^2 + N^2 K^2 \Delta t^2}.$$

Since the right hand side of the above equation is always less than or equal to 1, $\omega \Delta t$ is always real, and the quasi-trapezoidal scheme is, as designed, unconditionally stable.

The dispersion relation for this scheme, determined in the same way as for the quasi-leapfrog scheme, is

$$C_t^2 = C_r^2 \left(1 - \frac{5}{12} C_r^2 k^2 \Delta t^2 + \ldots \right). \tag{3.14}$$

Comparing the dispersion for the quasi-trapezoidal scheme (3.14) to that for the quasi-leapfrog scheme (3.11) shows that, for a given time-step Δt, the quasi-trapezoidal scheme introduces five times as much dispersion of horizontal wavelengths as the quasi-leapfrog scheme. Further, the quasi-trapezoidal scheme misrepresents the phase speed by five times as much as the quasi-leapfrog scheme. Figure 3.1 shows a comparison of the quasi-trapezoidal and quasi-leapfrog scheme when applied to the simple case of an atmosphere capped by a rigid lid and forced by a simple heat source with with a half-sinusoidal structure in the vertical and a witch of Agnesi profile in the horizontal (see Nicholls *et al.* 1992). The solid line in Fig. 3.1 is the vertical velocity at 5 km above the surface at time 2 hours computed using semi-analytic techniques. The heating excites many different horizontal wavelengths but only a single vertical wavelength; thus, according to (3.8), there should be no dispersion. The dispersion of horizontal wavelengths, however, shows up clearly in the trailing edge of the pulse in quasi-trapezoidal scheme (long-dashed line). For this

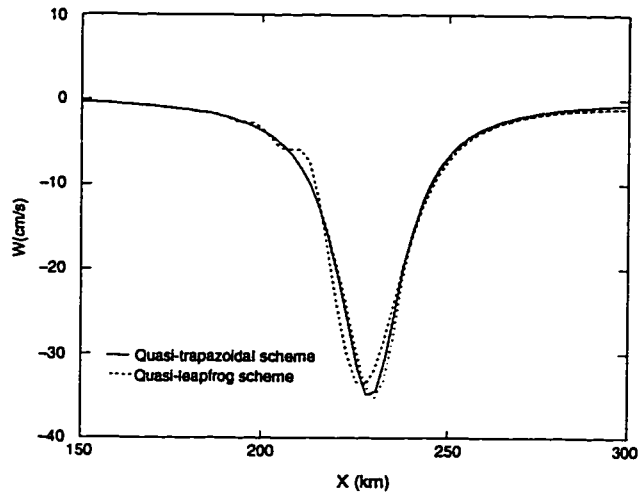

Figure 3.1. A comparison of the quasi-leapfrog and quasi-trapezoidal schemes. The true solution is indicated by the solid line.

computation, Δt and Δx were chosen so that

$$\frac{C_r \Delta t}{\Delta x} \approx 0.1,$$

which falls well within the stability limits for the quasi-leapfrog scheme. The results of an integration performed with the quasi-leapfrog scheme, with the same choice of Δt and Δx, are shown in Fig. 3.1 by the short-dashed line. Notice that the quasi-leapfrog scheme, unlike the quasi-trapezoidal scheme, does not show the effects of dispersion. The quasi-leapfrog scheme solution leads the true solution while the quasi-trapezoidal scheme lags the true solution, in agreement with (3.11) and (3.14). Since the time step chosen for the two integrations is the same, Fig. 3.1 implies that the increased stability of the quasi-trapezoidal scheme affords no increase in computational efficiency because the quasi-trapezoidal scheme produces large errors at a time step for which the quasi-leapfrog scheme is still stable. For this reason, the quasi-leapfrog method was used in constructing the linear model.

Figure 3.2a demonstrates the accuracy of the numerical integration by comparing the

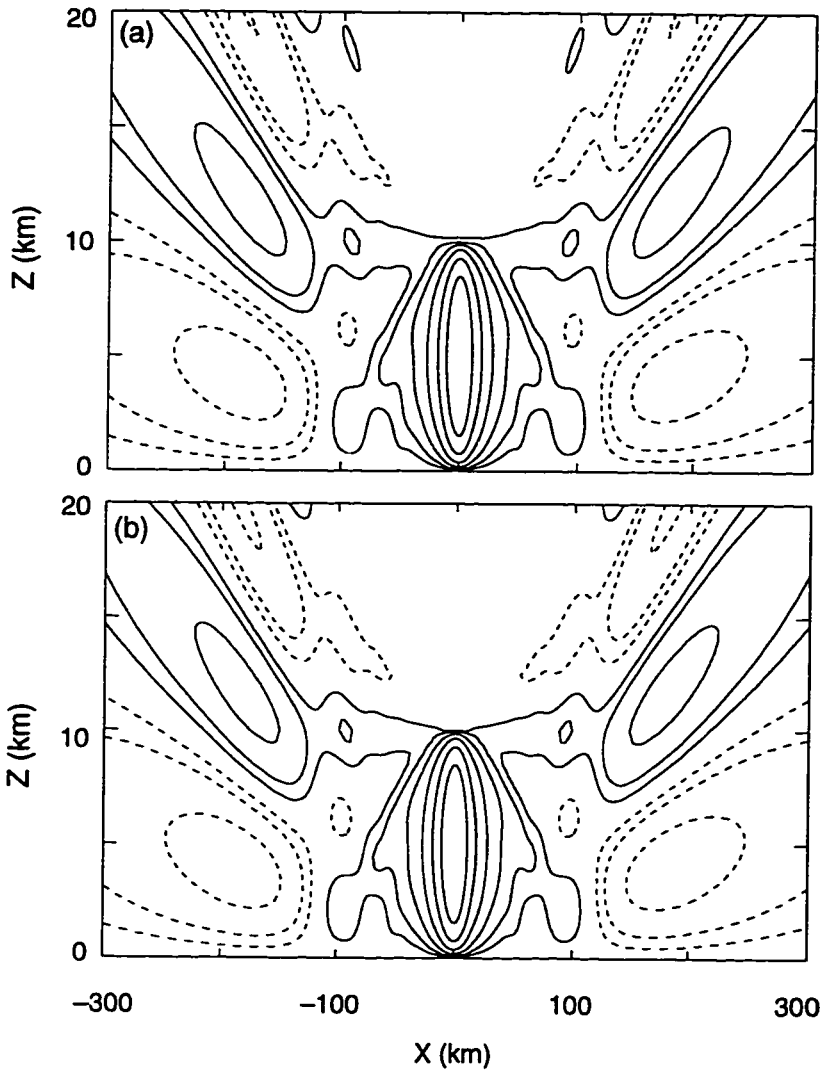

Figure 3.2. Vertical velocity (2 m s^{-1} contours, negative values dashed) forced in a Boussinesq atmosphere by a specified heating of the form given in Nicholls *et al.* (1992). (a) Analytic solution from Pandya *et al.* (1993). (b) Solution from the linear numerical model.

vertical velocity determined by numerical integration to the vertical velocity computed using a quasi-analytic technique. In this example, the atmosphere is assumed to be in hydrostatic balance, $\bar{U}$ is assumed to be uniformly 0, and N is 0.01 s^{-1}. A thermal forcing,

described by

$$Q(x,z) = \begin{cases} Q_o \frac{a^2}{a^2+x^2} \sin\left(\frac{z\pi}{H}\right) & \text{if } z < H \\ 0 & \text{otherwise,} \end{cases},$$

where $a = H = 10$ km, is applied. Figure 3.2a shows the vertical velocity at $t = 2$ hours, computed using the numerical model. In this simulation, $\Delta x = 5$ km, $\Delta z = 500$ m, and $\Delta t = 12$ s. Figure 3.2b shows a plot of the quasi-analytic solution at the same time, as determined by Pandya *et al.* (1993).

3.2 A two-dimensional nonlinear model

The two-dimensional squall line simulations presented in this paper were performed using a two dimensional version of the cloud model used in Miller and Durran (1991). This is a nonhydrostatic and fully compressible model, employing the warm rain bulk microphysics used in the Klemp and Wilhelmson (1978) cloud model. The governing equations for this model are the momentum equations,

$$\frac{\partial(\rho u)}{\partial t} + \frac{\partial(\rho u^2)}{\partial x} + \frac{\partial(\rho uw)}{\partial z} + \frac{\partial p}{\partial x} = \rho D_u \tag{3.15}$$

$$\frac{\partial(\rho w)}{\partial t} + \frac{\partial(\rho uw)}{\partial x} + \frac{\partial(\rho w^2)}{\partial z} + \frac{\partial p}{\partial z} = -(\rho - \bar{\rho})g + \rho D_w, \tag{3.16}$$

a prognostic pressure equation derived from the continuity equation,

$$\frac{\partial p}{\partial t} + \frac{c_p p}{c_v \rho}\left[\frac{\partial(\rho u)}{\partial x} + \frac{\partial(\rho w)}{\partial z}\right] = \frac{c_p p}{c_v \theta}\frac{\partial \theta}{\partial t}, \tag{3.17}$$

and the thermodynamic equation,

$$\frac{\partial \theta}{\partial t} + u\frac{\partial \theta}{\partial x} + w\frac{\partial \theta}{\partial z} = Q + D_\theta. \tag{3.18}$$

The D_u, D_w, and D_θ terms in (3.15), (3.16), and (3.18) denote the subgrid scale mixing determined using the Richardson number dependent first-order closure scheme described in Durran and Klemp (1983). The term $\bar{\rho}$ in (3.16) is the mean state density. In (3.18) Q represents a diabatic heat source, either applied externally or computed as the result of

microphysical processes; u, v, and w are the wind components in the x, y and z directions and p is the pressure. This system is completed by the equation of state and, in moist simulations, the continuity equations for water, which are given in Durran and Klemp (1983).

Equations (3.15) - (3.18) were integrated using a two-time-step scheme (Klemp and Wilhelmson 1978; Skamarock and Klemp 1992) in which a small time step was used to stably integrate the terms involving high-speed sound waves and a larger time step was used for other terms. The model domain was 700 km wide by 22 km high, with a horizontal resolution of 1000 m and and a vertical resolution of 350 m. The small time step was 2 seconds, and the large time step was 6 seconds. The upper and lateral boundaries were open, allowing waves to propagate out of the computational domain with minimal spurious reflection. Perturbations in u and θ were advected outward through the lateral boundaries at fixed phase speeds equal to the Doppler-shifted phase speed of the gravest gravity wave mode (Pearson 1974; Durran *et al.* 1993). The radiation upper boundary condition followed Klemp and Durran (1983) and Bougeault (1983).

3.3 A three-dimensional nested-grid nonlinear model

Like the two-dimensional model, the three dimensional model is an fully compressible, nonhydrostatic model. The momentum equations are cast in advective form, and π is used as the prognostic variable. The two horizontal momentum equations in advective are,

$$\frac{du}{dt} + fv + c_p\theta_v\frac{\partial \pi}{\partial x} = D_u \tag{3.19}$$

$$\frac{dv}{dt} + -fu + c_p\theta_v\frac{\partial \pi}{\partial v} = D_v, \tag{3.20}$$

and the vertical momentum equation is

$$\frac{dw}{dt} + c_p\theta_v\frac{\partial \pi}{\partial z} = g\frac{\theta_v - \bar{\theta}_v}{\bar{\theta}_v} + D_w. \tag{3.21}$$

The prognostic pressure equation is given by

$$\frac{d\pi}{dt} + w\bar{\Pi}_z + \frac{R}{c_v}\left(\bar{\Pi} + \pi\right)\left(\frac{\partial u}{\partial x} + \frac{\partial v}{\partial y} + \frac{\partial w}{\partial z}\right) - \frac{R}{c_v}\frac{\left(\bar{\Pi} + \pi\right)}{\theta_v}\frac{d\theta_v}{dt} = 0, \tag{3.22}$$

and the thermodynamic energy equation is

$$\frac{d\theta}{dt} = D_\theta. \tag{3.23}$$

In 3.19, 3.20, 3.21, and 3.23 the D_u, D_v, D_w, and D_θ terms denote subgrid scale mixing determined via a Richardson number dependent first-order closure scheme (Durran and Klemp, 1983),

$$\frac{d}{dt} = u\frac{\partial}{\partial x} v\frac{\partial}{\partial y} + w\frac{\partial}{\partial z},$$

$$\theta_v = \theta(1 + 0.61 q_v),$$

and

$$\bar{\Pi} + \pi = \left(\frac{p}{p_o}\right)^{\frac{R}{c_p}},$$

where p is the pressure, p_0 is a reference pressure, q_c is the water vapor content of the air, f is the Coriolis parameter (unless otherwise noted, f is 0 and the Coriolis force is neglected in the simulations presented here), and all other symbols have their conventional meanings. This system is completed by the equation of state; unlike the two-dimensional model, this model does not yet have any moist processes, so there is no continuity equation for water.

This system is integrated forward in time using a two time-step technique similar to the one used in the two-dimensional model. The boundary conditions are also handled in the same way as the two-dimensional model. In order to increase computational efficiency, the three-dimensional model uses grids of different spatial and temporal resolutions. In the simulations presented in Chapter 6, a fine resolution mesh is centered around the region of the thermal forcing in order to better resolve the fine scale structures associated with the thermal forcing. Farther from the thermal forcing, where the behavior of the atmosphere is dominated by large scale features, the resolution in coarser. The procedure for nesting of grids is described in Skamarock and Klemp (1993).

Chapter 4

QUASI-TWO-DIMENSIONAL CIRCULATION AROUND SQUALL LINES

Section 2.1 demonstrated that many of the features around squall lines can be understood as part of a quasi-two dimensional circulation. In this chapter, the quasi-two dimensional circulation will be examined with particular attention to the role of gravity waves forced by the time-mean convective thermal forcing in the circulation. A pair of two-dimensional numerical simulations will be compared; a "reference simulation" of LL-TS system with a parameterization of warm cloud microphysics, and a "dry simulation", in which the microphysical forcing has been eliminated and a steady thermal forcing is used instead to excite the circulations. After describing the initial conditions in Section 4.1, the horizontal velocity perturbations in both simulations are compared in Section 4.2. In Section 4.3 the vertical motions in the trailing stratiform region are examined, and Section 4.4 focuses on the upper-level temperature perturbations in the trailing anvil.

4.1 Initial conditions

The simulations presented here were initialized with horizontally uniform profiles of wind, temperature, and moisture based on observations of the pre-storm environment of the 22 May 1976 squall line that passed through the mesonetwork of the NSSL in central Oklahoma (Ogura and Liou 1980). The thermodynamic sounding is shown in Fig. 4.1a; it is a smoothed version of the HNT 1430 CST sounding. In addition to the smoothing, the thermodynamic profile has been modified by warming and moistening the layer between the surface and $\sim$ 850 mb in order to facilitate the development of convection. This mod-

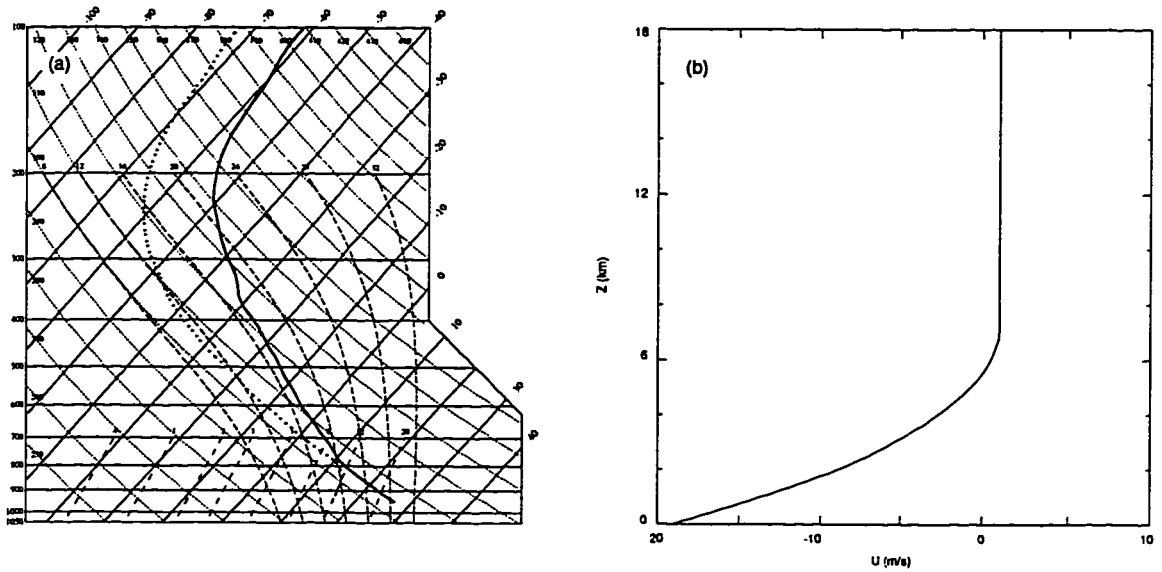

Figure 4.1. The initial sounding used in the reference and dry simulations: (a) Skew-T diagram diagram showing the temperature (solid) and dewpoint temperature (dashed); (b) vertical profile of the horizontal wind speed.

ified sounding is identical to the one used in a previous numerical simulation of the 22 May 1976 squall line performed by Fovell and Ogura (1988); it has a CAPE (convective available potential energy) of $\sim$ 2400 J kg^{-1}. Fig. 4.1b shows the storm-relative mean horizontal wind used in the reference simulation. It is also similar to the wind profile presented in Fovell and Ogura (1988), but is smoothed to eliminate discontinuities in the wind shear. Even with this smoothing, the low-level shear in the reference state wind profile remains comparable to that observed in the pre-storm environment on 22 May 1976 (Ogura and Liou 1980). Convection in the reference simulation was initiated using a 2 K warm bubble near the surface.

4.2 Mesoscale horizontal velocity perturbations

As shown in Fig. 2.1, the observed flow in the trailing stratiform region can be divided into two primary currents: an upper-level ascending front-to-rear flow (FTRF) and a mid-level

descending rear inflow (RI). Figure 2.1 also shows an upper level rear-to-front flow ahead of the convective line. This feature, often associated with a forward spreading cloud anvil, will be referred to as the leading anvil flow (LAF).

In the remainder of this section, two numerical simulations are compared to illustrate the role that gravity waves forced by the latent heating and cooling in and near the leading convective line play in the development and maintenance of the horizontal velocity perturbations in the mesoscale region around convection. The first of these simulations, the reference simulation, is a complete simulation which employed a parameterization of warm cloud microphysics. The second simulation presented here was performed with the microphysical parameterizations switched off; instead the circulation was generated by a steady thermal forcing.

4.2.1 Time-averaged horizontal velocity

Figure 4.2a shows a 30-minute time-average of the storm relative horizontal velocity that develops in the mature stage of the reference simulation. The time average was taken to eliminate some of the small time-scale features of the flow and thereby facilitate the comparison of the simulated flow and the conceptual model presented in Fig. 2.1. The light and dark shading highlight regions of strong negative and positive velocity, respectively.

As shown in Fig. 4.2a, the time-averaged flow in the reference simulation is similar to that in the conceptual model of a squall line with trailing stratiform precipitation presented in Fig. 2.1. The FTRF begins just above the gust front ($x = 0$ km) and ascends as it moves rearward. Beneath the FTRF the RI extends rearward from the gust front. The region ahead of the convection in Fig. 4.2a also shows a similarity to the conceptual squall line; both the upper-level cloud edge and the rear-to-front flow indicate a LAF.

The flow shown in Fig. 4.2a is also consistent with observations of the 22 May 1976 squall line. The 27 m s^{-1} maximum speed in the FTRF is similar to the 25 m s^{-1} maximum reported by Smull and Houze (1987a) in their dual Doppler analysis of the 22 May 1976

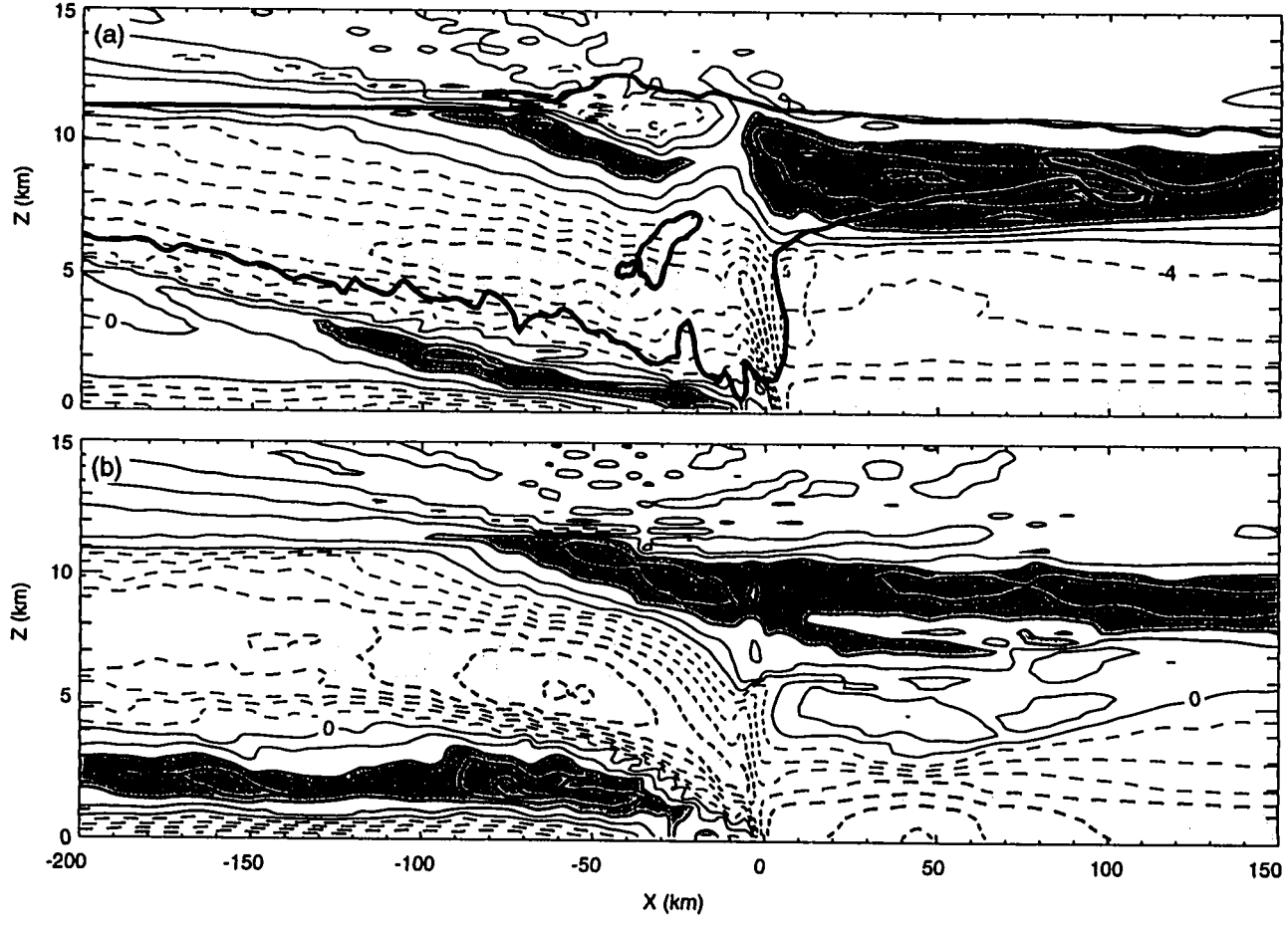

Figure 4.2. (a) Time-average system-relative horizontal velocity (thin lines, contoured in 4 m s^{-1} intervals) in the reference simulation. Time-average is taken from 7.5 to 8 hours. Dark shading highlights rear-to-front flow greater than 8 m s^{-1}; light shading highlights front-to-rear flow with speed exceeding 16 m s^{-1}. Cloud outline (q_c = 0.1 g kg^{-1}) is indicated by the heavy line. (b) Time-average horizontal velocity taken from t = 5.5 to 6 hours in the dry simulation. Shading and contours as in (a).

squall line. The RI in Fig. 4.2a reaches a maximum value in excess of 15 m s^{-1} which agrees with the 17 m s^{-1} peak reported by Smull and Houze (1987b). In Fig. 4.2a the LAF extends $\sim$ 120 km ahead of the convection and includes a region with forward-directed velocities exceeding 9 m s^{-1}. This is in broad agreement with Ogura and Liou (1980) who show a 110 km wide region of rear-to-front flow exceeding 10 m s^{-1}.

A series of numerical simulations were performed to test the sensitivity of the kinematic features in the trailing anvil to the heating and cooling in the region of the leading convective line. These simulations were performed using the same initial conditions and the same numerical model, but they were performed "dry", *i. e.* with the microphysical parameterizations turned off. Sensitivity tests performed using the dry model show that the mesoscale circulation around the squall line is primarily generated by the low-frequency components of the thermal forcing. A good approximation to the mesoscale circulation surrounding the squall line can be generated by a steady thermal forcing of the form shown in Fig. 4.3a. This thermal forcing was constructed by time averaging and smoothing the latent heating and cooling in the reference simulation. The heating and cooling in the reference simulation was averaged over the period from 4.5 to 6.5 hours in order to obtain a pattern representative of the mature phase of the squall line and eliminate the signature of individual convective cells. In order to keep the thermal forcing compact, the thermal forcing was set to zero at all points where its magnitude was less than 0.0001 K s^{-1}. The residual cellular structure was removed by running the time-averaged field through a second order smoother 200 times, and the resulting field was scaled so that its integrated absolute value matched the integrated absolute value of the time-averaged field. The instantaneous heating and cooling in the reference simulation at $t = 6$ hours is shown in Fig. 4.3b for comparison.

Figure 4.2b shows the horizontal velocities generated by the thermal forcing shown in Fig. 4.3a. Although the thermal forcing is steady and smooth, the dynamical response to this forcing is neither steady nor smooth. As in Fig. 4.2a, the horizontal velocities in Fig. 4.2b have been averaged over a 30-minute interval in order to emphasize the slowly

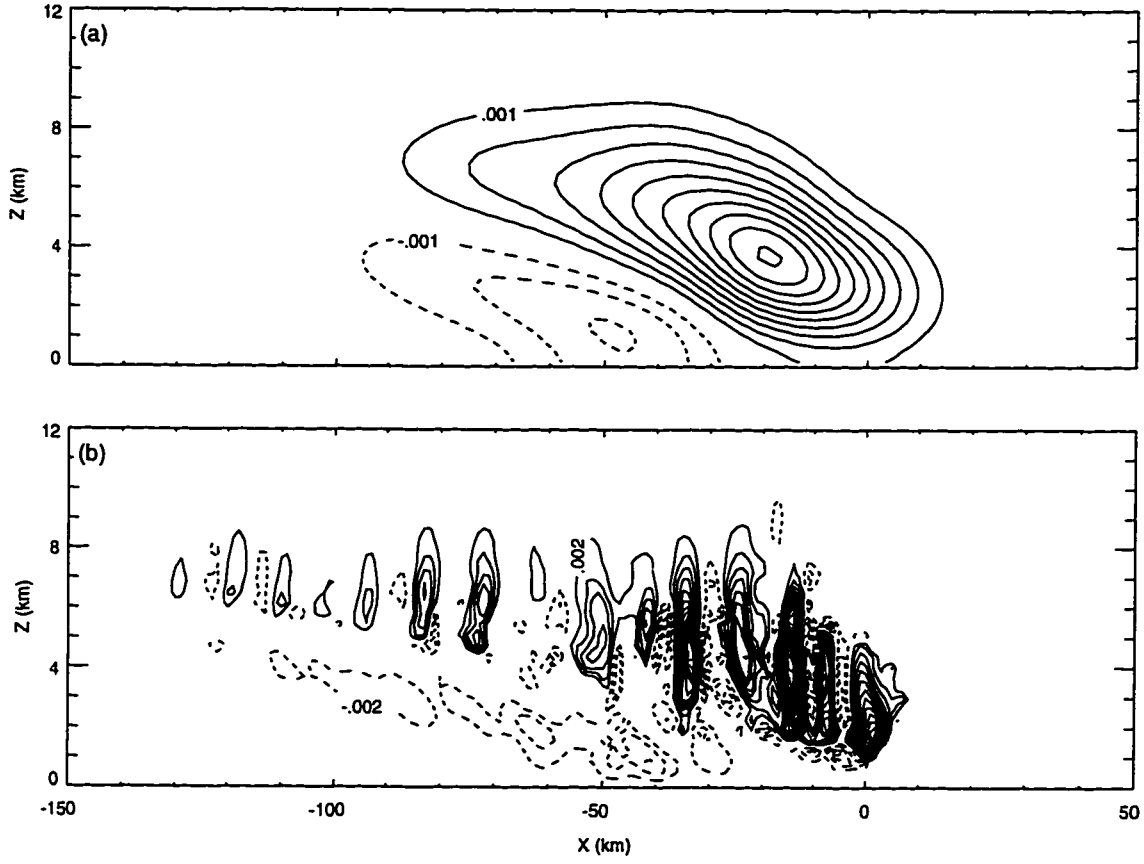

Figure 4.3. (a) Thermal forcing used in the dry simulation; contour interval is 0.001 K s^{-1}. (b) Instantaneous pattern of heating and cooling in the reference simulation at $t = 6$ hours; contour interval is 0.002 K s^{-1}.

varying structures in the flow. This 30-minute average was taken from 5.5 to 6.5 hours, two hours earlier than the time average shown in Fig. 4.2a, in order to account for the slower initiation and evolution of the squall line in the reference simulation during which time the pattern of latent heating and cooling differed from that in the mature phase.

The horizontal flow presented in Fig. 4.2b is qualitatively similar to the flow in both the reference simulation and the schematic diagram of a squall line shown in Fig. 2.1. A pronounced FTRF begins near the gust front ($x = 0$ km) and ascends rearward, and a region of RI occurs beneath it. An upper level LAF is visible in the region $z > 8$ km and $x > 0$ km.

The presence of these flows in the dry simulation suggests that the large-scale horizontal circulation in the stratiform region behind the squall line arises primarily in response to the thermal forcing generated near the system's leading edge.

The RI in the dry simulation shows a pronounced bimodal structure, with two regions of stronger inflow separated by an area of weaker inflow. In Fig. 4.2b, a local maximum in the inflow is centered at $x \sim$ -150 km and another stronger maximum inflow extends from $x \sim$ -90 km to the gust front. This bimodality in the amplitude of the RI was also observed in the stratiform region trailing the 22 May 1976 squall line (see Fig. 13 of Ogura and Liou 1980 and Fig. 9 of Smull and Houze 1985). A bimodal RI with a maximum inflow located immediately to the rear of the convective line and a second maximum at the back edge of the trailing stratiform anvil is common in leading line/trailing anvil systems (Smull and Houze 1987b). Some studies have suggested that the formation of the second maxima at the back edge of the trailing anvil results, at least partly, from local cooling (Smull and Houze 1987b; Yang and Houze 1995b). The results of the dry simulation indicate that some bimodality in the RI can, nevertheless, be generated by the mean thermal forcing at the system's leading edge.

Although the location and qualitative structure of the circulation features match in the dry and reference simulations, a close comparison of Figs. 4.2a and b reveals that the wind speeds are somewhat larger in the dry simulation in spite of the fact that the absolute amplitude of the thermal forcing in the two simulations was the same. In the dry simulation, the circulation was generated by a thermal forcing that was constant in time, whereas the circulation in the reference simulation was generated by a time-varying thermal forcing associated with the release and absorption of latent heat by the active convection. The steady thermal forcing in the dry simulation projected more directly onto the low-frequency gravity waves that determine the mesoscale circulation, while the time-varying thermal forcing in the reference simulation projected relatively more energy onto high-frequency modes less important to mesoscale circulation. Thus, since the amplitude of the thermal forcing was the same in the two simulations, the dry simulation had more amplitude in the

low-frequency modes and a stronger mesoscale circulation.

Although most large-scale features of the dry and reference simulation agree, there are some differences worth noting. In the dry simulation there is a region of rear-to-front flow between $x = 10$ km and $x = 60$ km and around $z = 6$ km that does not occur in the reference simulation. An explanation of this difference can be found in the evolution of the horizontal velocity field, which will be discussed in the next section.

4.2.2 Evolution of the horizontal velocity

Some insight into the dynamics governing the development of the mesoscale horizontal flows can be gained by examining the instantaneous horizontal velocity perturbations in the reference and dry simulations. Figures 4.4a and 4.4b show the instantaneous horizontal velocity in the reference simulation at $t = 4.5$ hours and $t = 6$ hours, respectively. In Figure 4.4a there are two distinct upper level extrema, features 1 and 3, which quickly move out of the model domain so that neither is visible in Fig. 4.4b. (Note that features 1 and 3 have a signature that extends all the way to the surface, although both features are weak at low levels and hard to identify because of the strong low-level mean wind.) Features 1 and 3 are fast moving transient gravity wave modes generated by the thermal forcing in the convective region. The tilt of features 1 and 3 is consistent with gravity waves transporting energy upward and away from the convective region and their speed of propagation is the same as the phase speed of hydrostatic gravity waves with a vertical half-wavelength of about 8.5 km, which is approximately equal to the 8 km depth of the convective cells.

While features 1 and 3 quickly propagate far away from the squall line, feature 2 moves at approximately the same speed as the downstream edge of the FTRF. Like features 1 and 3, feature 2 maintains its vertically upright structure as it propagates laterally from $x \sim$ -185 km in Fig. 4.4a to $x \sim$ -315 km in Fig. 4.4b. Horizontal velocity perturbations that include both an upper level FTRF and a low-level RI immediately trail feature 2. Feature 2

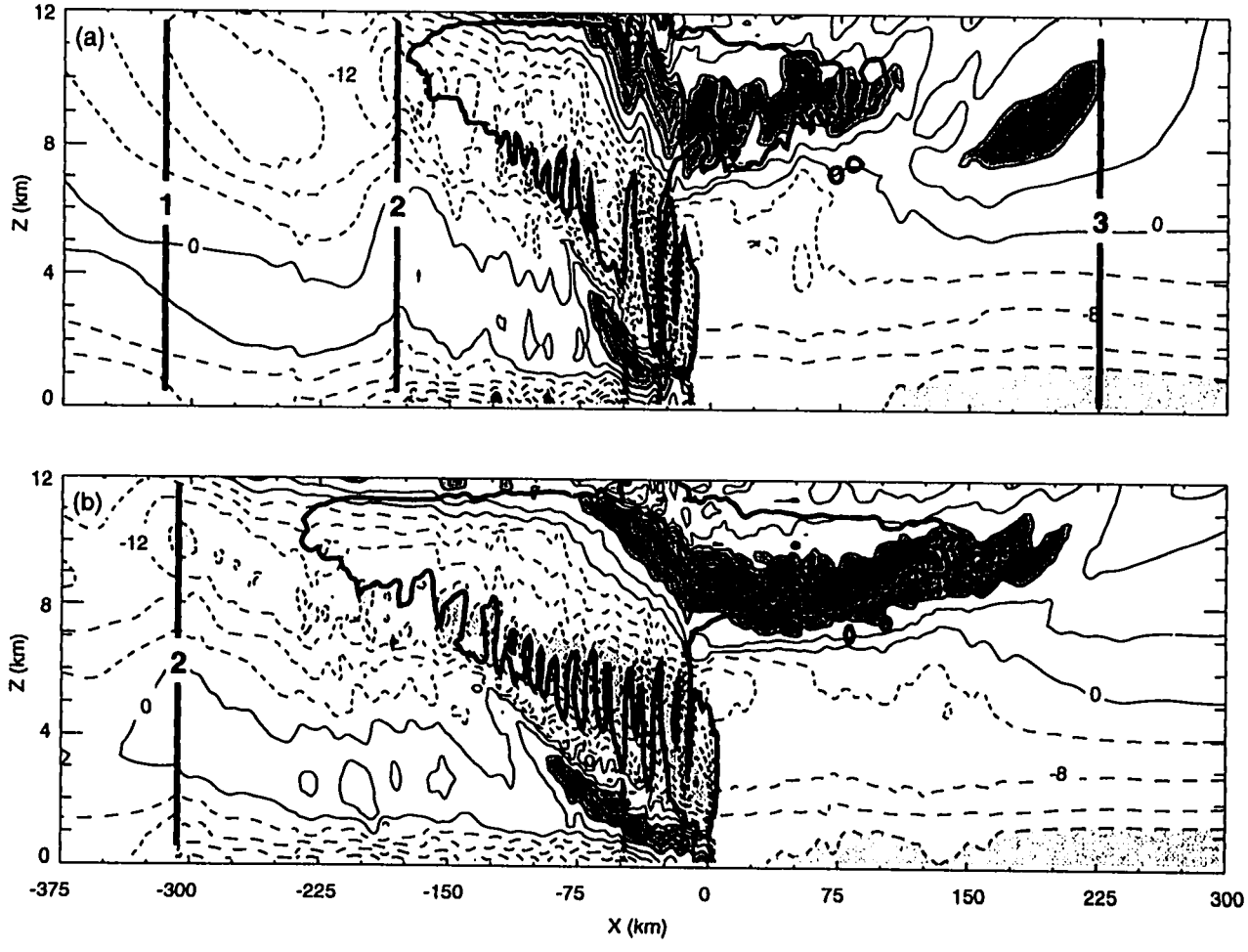

Figure 4.4. Snapshots of the horizontal velocity in the reference simulation at: (a) $t = 4.5$ hours and (b) $t = 6$ hours. Contours and shadings are as in Fig. 4.2. Cloud outline is indicated by the heavy line.

and the velocity perturbations behind it together resemble the linear gravity wave response to a steady and compact thermal forcing shown in Fig. 1.1. Thus, although the RI and FTRF don't look like canonical monochromatic gravity waves, they appear to be a gravity wave response to the convective thermal forcing. Notice that feature 2 and the RI and FTRF behind it propagate more rapidly than the cloud edge, suggesting that the FTRF and RI are not directly forced by in situ microphysical processes in the stratiform region.

Simple advection can not explain the fact that feature 2 retains its coherent vertical structure as it propagates. This can be seen in Fig. 4.5, which compares the propagation

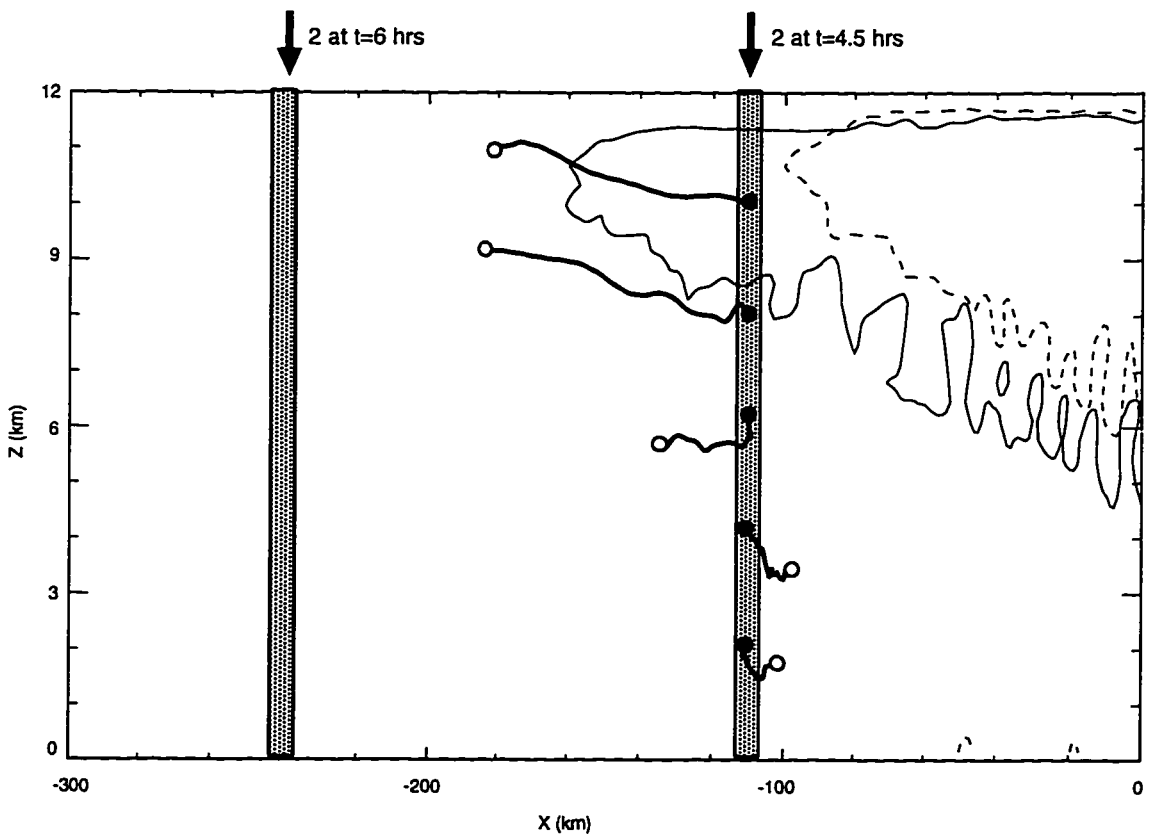

Figure 4.5. Trajectories (thick solid lines) from $t = 4.5$ (closed circles) to $t = 6$ hours (open circles) in the reference simulation. Cloud outline is indicated at $t = 4.5$ hours (thin dashed lines) and $t = 6$ hours (thin solid lines).

of feature 2 with the trajectories of air parcels initially within feature 2. The trajectories

begin at t = 4.5 hours at 2 km vertical intervals along the line x = -185 km, and end 1.5 hours later at the open circles. The propagation of feature 2 over the same interval is indicated by the two labeled shaded lines. Feature 2 propagates faster than any of the parcels initially within it, which is inconsistent with advection. Furthermore, advection along the trajectories indicated would tend to destroy the vertical structure but, as shown in Fig. 4.4, feature 2 maintains its vertical structure. Since there is no active convection in this region, and therefore no thermal forcing, and since the movement of feature 2 cannot be attributed to advection, the motion of feature 2 must be the result of gravity wave propagation.

Figure 4.6 shows the evolution of the flow in the dry nonlinear simulation over a 1.5 hour period. As in the reference simulation, shown in Fig. 4.4, a pair of upper-level outrunning horizontal velocity extrema (features 1 and 3 in Fig. 4.6a) develop in the dry simulation and quickly move out of the domain by the time shown in Fig. 4.6b. While the structure and speed of propagation of these features agree in the two simulations, feature 3 seems to have greater amplitude at midlevels in the dry simulation. This difference is the result of differences in thermal forcing early in the simulations. The dry simulation used a steady heat source that was switched on suddenly at t = 0, while the heating in the reference simulation evolved gradually. The amplitude of feature 3 was appreciably less in additional dry simulations in which the thermal forcing was turned on gradually.

As in the reference simulation, the spread of the horizontal velocity perturbations in the stratiform region appears to be linked to the propagation of feature 2. In both simulations feature 2 maintains its vertical structure as it propagates through regions of pronounced vertical shear and leaves velocity perturbations in its wake that include the FTRF and RI. The propagation of feature 2 and the velocity perturbations behind it are again reminiscent of the linear gravity wave response to a compact heat source as shown in Fig. 1.1. This suggests that the FTRF and RI are indeed part of the gravity wave response to the time-mean thermal forcing.

Examining the evolution of the flow in the reference simulation, Fig 4.4, one might suppose that features 1 and 3 are forced by an early profile of the thermal forcing from the

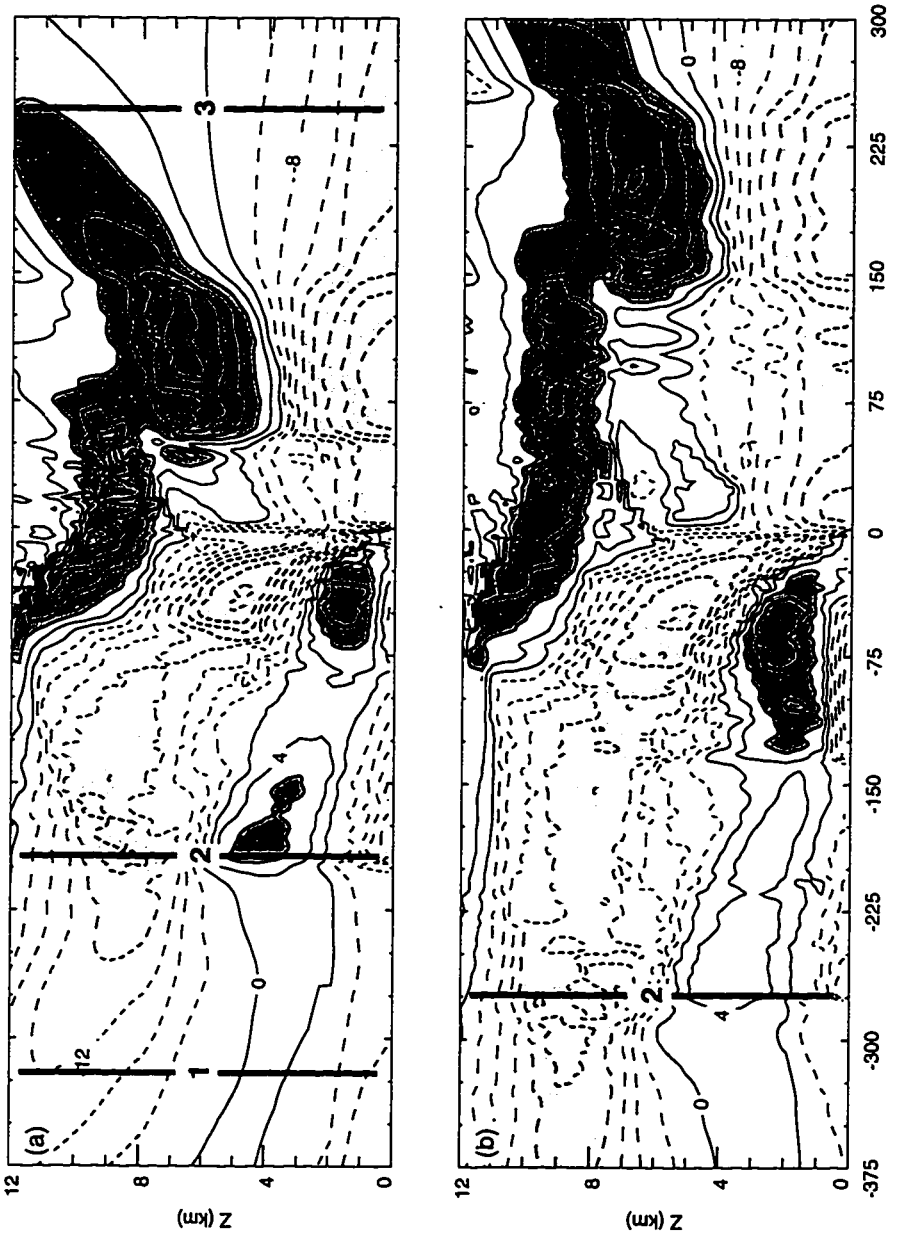

Figure 4.6. Snapshots of the horizontal velocity in the dry simulation at: (a) $t = 2.5$ hours and (b) $t = 4$ hours. Contours and shadings as in Fig. 4.2.

leading line, and feature 2 is the response to the thermal forcing of the mature state. This idea is, however, refuted by the presence of features 1 and 3 in the dry simulation (Fig. 4.6) in which the thermal forcing is constant in time. Instead, the formation of distinct features in the trailing anvil is the result of the horizontal dispersion of different gravity wave modes. In both the reference and dry simulations, features 1, 2, and 3 mark individual contour lines associated with disturbances that extend over a large horizontal distance, so these disturbances are approximately hydrostatic. The horizontal phase speed and the horizontal group velocity of hydrostatic, Boussinesq gravity waves are identical and equal to N/m where N is the Brunt-Väisälä frequency, and m is the vertical wave number. Since the horizontal group velocity and phase speed are identical, the displacement of any particular contour (not just a maxima and minima) will give an indication of the speed of the wave associated with the feature. In both the reference and dry simulations, feature 2 travels at $\sim$14 m s^{-1}, which is the speed of a hydrostatic wave whose $\sim$8.5 km vertical wavelength is comparable to the depth of the thermal forcing. Features 1 and 3 propagate at $\sim$28 m s^{-1}, which is the speed of a wave with a vertical wavelength twice the depth of the thermal forcing. The dispersion of modes with different vertical wavelengths is illustrated by the simple linear simulation shown in Fig. 4.7. This simulation is identical to the linear simulation shown in Fig. 1.1, except that the vertical structure of the heat source is composed of two modes whose vertical wavelengths differ by a factor of two (see Fig. 4 of Nicholls, *et al.* 1991). The superposition of these modes resembles the profile of diabatic heating associated with leading line/trailing stratiform systems (Houze 1982; Johnson and Young 1983; Mapes 1993; Mapes and Houze 1995). The horizontal velocity perturbations that develop in response to this forcing show two distinct modes propagating at different speeds that are analogous to features 1 and 2 in Figs. 4.4 and 4.6.

It is worth pointing out that in both the reference and dry simulations feature 2 moves at the same speed as the rearward traveling edge of the low-level cold pool. (The cold pool can be inferred from Figs. 4.4 and 4.6 by the negative velocities at the surface behind the gust front.) An additional simulation was performed that was identical to the reference

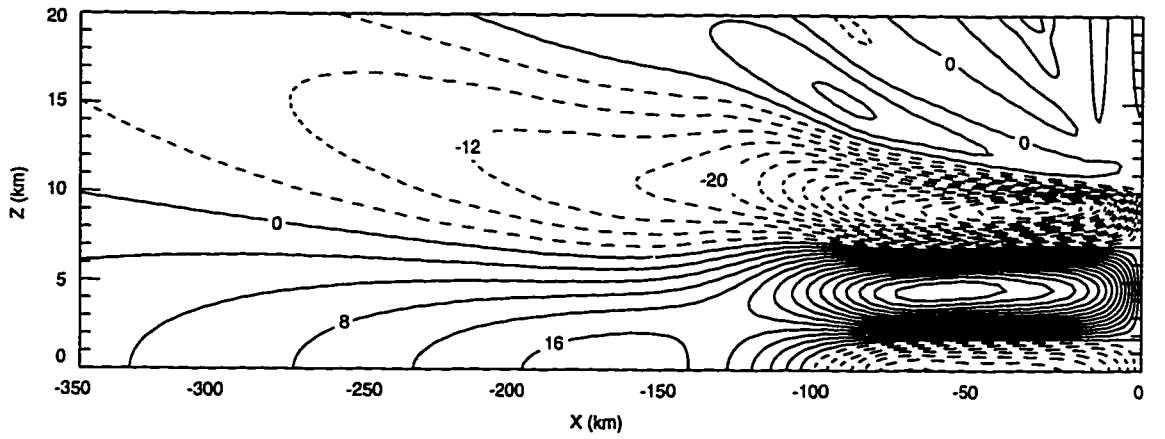

Figure 4.7. Horizontal velocity (contoured in 4 m s^{-1} intervals) at t = 2 hours generated by a compact heat source that forces two different modes in a linear model.

simulation except that the low-level cold pool was limited to x > -175 km by relaxing the temperature perturbations below 1.5 km and to the rear of x = -175 km back to the initial unperturbed values. Neither the upper-level structure nor the speed of propagation of feature 2 was significantly changed in this simulation, suggesting that the feature 2 is not dependent on the rearward spreading cold-pool, but is a consequence of the thermal forcing from the leading line.

4.3 Mesoscale vertical motions

As discussed in Section 2.1.4, significant vertical motion is often associated with the trailing stratiform anvil. The source of this motion is investigated in Section 4.3.1, and shown to be the result of gravity waves forced by the leading line. Further, these gravity waves produce velocity perturbations that determine how the cloudy air from the convective region is distributed outward. Thus, as shown in Section 4.3.2, the thermally forced gravity waves also influence the shape and extent of the trailing and leading anvils.

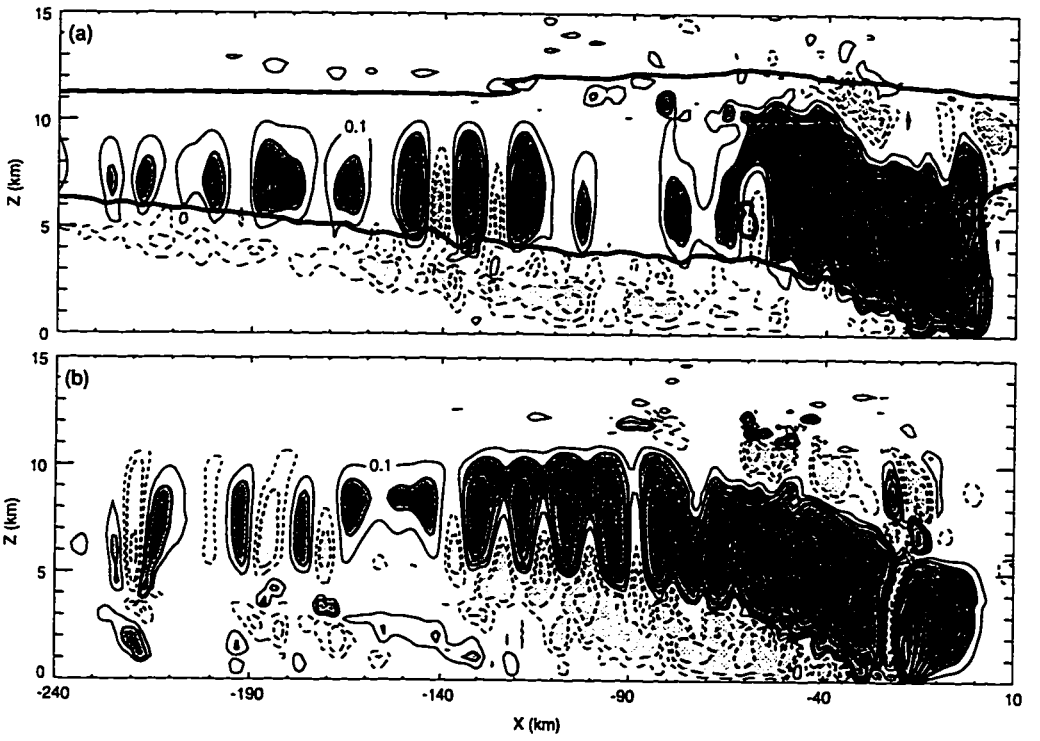

Figure 4.8. (a) Time-average vertical velocity (thin lines, contours are $w = \pm 0.1, \pm 0.2, \pm 0.4, \ldots,$ ± 6.4 m s^{-1}) taken from $t = 8$ to 10 hours in the reference simulation. Dark shading indicates upward velocity exceeding 0.2 m s^{-1}; light shading indicates downdrafts with speed exceeding 0.2 m s^{-1}. Cloud outline is indicated by the thick line. (b) Time-average vertical velocity taken from $t = 6$ to 8 hours in the dry simulation. Contours and shadings are as in (a).

4.3.1 Time-averaged vertical velocities

Ogura and Liou (1980) observed a ~90 km wide region of ascent centered at 400 mb and a ~65 km wide region of descent centered at 850 mb in the stratiform region of the 22 May 1976 squall line. The vertical velocities seem relatively smooth in their analysis which was based on composite soundings, but finer scale Doppler radar observations by Smull and Houze (1987a) reveal cell-like perturbations in the vertical velocity field. Figure 4.8a shows the vertical velocity field in the reference simulation, time averaged from 8 to 10 hours. There is a broad, continuous region of mesoscale ascent stretching ~80 km behind the gust front ($x = 0$ km). Farther to the rear, the vertical velocity field appears more cellular. These

cell-like updrafts exceed 0.8 m s^{-1}, comparable to to the >0.6 m s^{-1} maximum reported by Ogura and Liou (1988) $\sim$ 100 km behind the convection (they show a contour of -0.03 mb s^{-1} at 400 mb in their Fig. 16). Nearer to the region of convection, the vertical velocity exceeds 6.4 m s^{-1}, consistent with the 10 m s^{-1} measured by Smull and Houze (1987a). A region of mesoscale descent is visible behind the gust front and below the mesoscale updraft. The magnitude of the descent exceeds 0.4 m s^{-1}, consistent with the 40 cm s^{-1} downdraft observed by Ogura and Liou (1980) (contoured as 0.04 mb s^{-1} downdraft at 850 mb in their Fig. 16).

Figure 4.8b shows the time average vertical velocity that develops in the dry simulation driven by the thermal forcing shown in Fig. 4.3a. Here the time average was taken from t = 6 to 8 hours, which is two hours earlier than the interval shown in Fig. 4.8a. The 2 hour offset accounts for the gradual development of the convection early in the reference simulation, as discussed in Section 4.2.1. In agreement with the reference simulation, the mesoscale ascent in the dry simulation is continuous near the gust front (x = 0 km) and more cellular farther to the rear, and a broad region of mesoscale descent is apparent beneath the mesoscale updraft. Although the vertical velocity fields agree qualitatively in the two simulations, the magnitudes of the vertical velocities in the dry simulation systematically exceed those in the reference simulation. This is because, as discussed in Section 4.2.1, the steady thermal forcing in the dry simulation projects more directly onto the low frequency modes responsible for the mesoscale circulation than does the thermal forcing in the reference simulation.

In both the reference and dry simulations, the vertical velocity field shows more short horizontal wavelength structure than the horizontal velocity field, as can be seen by comparing Figs. 4.2a and b to Figs. 4.8a and b. For example, in the dry simulation, the FTRF extends smoothly to the left of x = -200 km, while the mesoscale updraft shows a cellular structure for x < -90 km. These cell-like velocity features cannot be the result of local microphysical processes since they are also apparent in the dry simulation which did not include microphysical processes. The vertical and horizontal velocity perturbations in

Boussinesq gravity waves are related by the polarization relation,

$$w_o = \frac{-H}{L} u_o, \tag{4.1}$$

where u_o and w_o are the amplitudes of the horizontal and vertical velocities, and H and L are the horizontal and vertical wavelengths, respectively. Equation (4.1), which can also be derived from scaling arguments applied to the continuity equation where H and L are horizontal and vertical length scales, implies that if two features have the same vertical scale and the same amplitude in the horizontal velocity perturbations, the feature with the shorter horizontal scale will be associated with the larger vertical velocity perturbations. Since the dominant vertical length scale in the horizontal and vertical velocity perturbations of the trailing anvil appears to be the same ($\sim$5 km), the vertical velocity field should be expected to show more small scale horizontal structure than the horizontal velocity field. Examining Fig. 4.8 reveals that the cells in the mesoscale updraft have a horizontal scale of $\sim$10 km, a vertical scale of $\sim$5 km, and an amplitude on the order of 0.5 m s^{-1}. Thus, according to (4.1), the horizontal velocity perturbations associated with this mode should have an amplitude of approximately 1 m s^{-1}. Although it is hard to see, Fig. 4.2 does indeed show weak small-horizontal scale modulations of the FTRF with a horizontal scale of $\sim$10 km and an amplitude of $\sim$1 m s^{-1}.

4.3.2 Vertical displacement

Although monochromatic linear gravity waves propagate without producing a net parcel displacement, the finite-amplitude gravity waves forced by the convective line and discussed in Section 4.2.2 do generate a perturbed flow that produces a net air-parcel displacement. All air-parcel displacements generated in the squall line are not, however, produced by gravity waves. In particular, the large vertical displacements that occurs as air in the convective region is lifted from the surface to the upper troposphere are driven by the diabatic heating of rising air parcels. The gravity wave and convectively driven displacements associated with squall lines are distinguished in Fig. 4.9a, which shows the

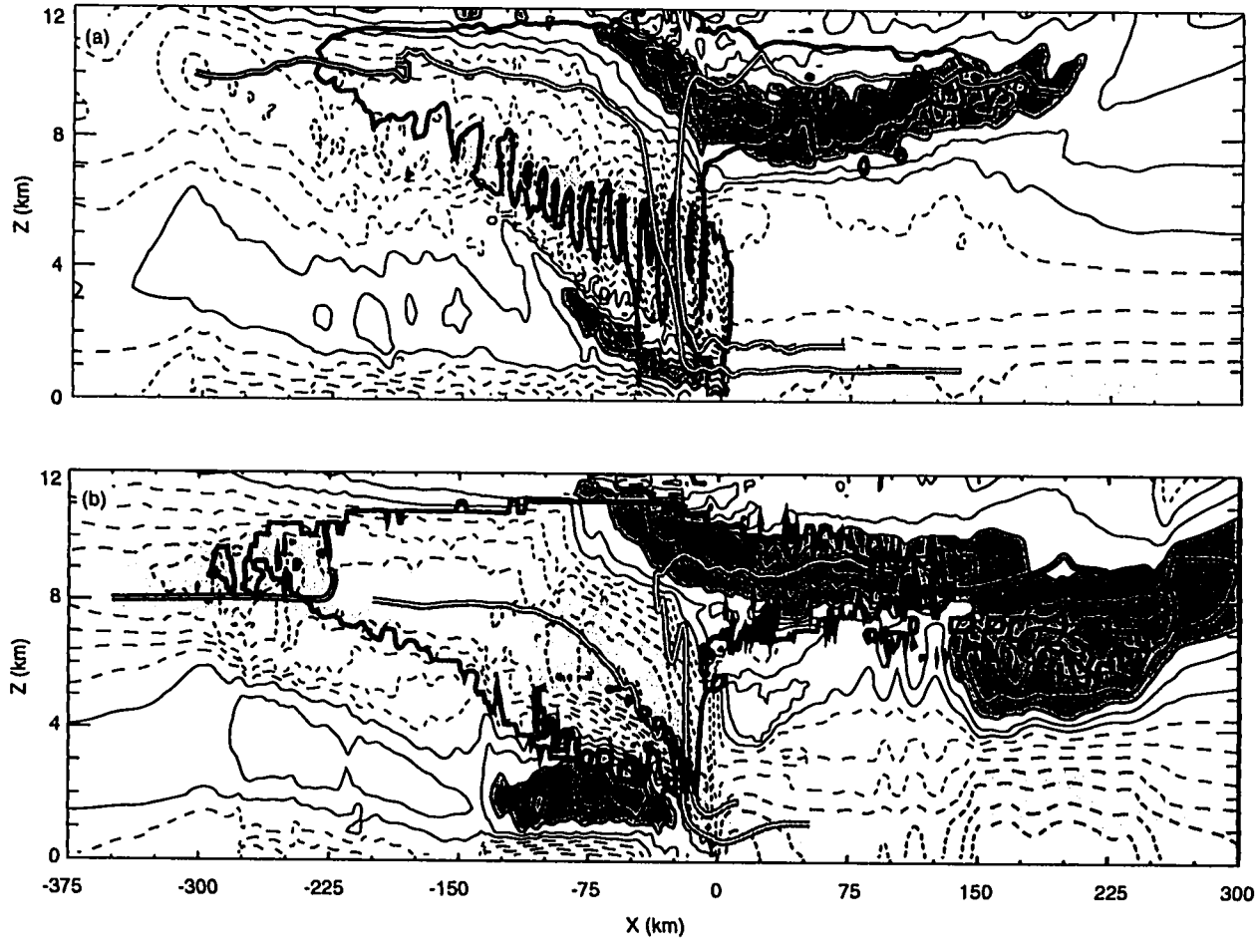

Figure 4.9. (a) Instantaneous horizontal velocity (thin lines, intervals and shading as in Fig. 4.2) at 6 hours in the reference simulation. Cloud outline is indicated by the heavier line. Trajectories of air parcels that end up within (outside) the cloud are indicated by grey (black) double lines. (b) Instantaneous horizontal velocity (thin lines, intervals and shading as in Fig. 4.2) at 4 hours in the dry simulation. The 2 km vertical-displacement contour is indicated by the heavier line. Trajectories of air parcels that end up within (outside) this region of enhanced vertical displacement are indicated by grey (black) double lines.

horizontal velocity (thin lines) and cloud outline (thick line) at time 6 hours in the reference simulation. Overlayed on the velocity field are back trajectories of two air parcels within the cloud (double grey lines), one from the leading anvil and one from the trailing anvil. The back-trajectories reveal that both of these air parcels have undergone a diabatically driven ascent within the region of convection and were advected away from the convective region by the perturbed horizontal flow. Note that the perturbed horizontal flow, which was established as a gravity wave response to the thermal forcing in the convective line, extends well beyond the edge of the cloud. The back trajectories of air parcels that end up outside the cloud (double black lines) are much shorter than those ending up within the cloud and show no diabatically driven ascent; this is consistent with the gravity wave interpretation of the spreading LAF and FTRF discussed in Section 4.2.2.

The cloud outline in Fig. 4.9a can be compared to the 2 km vertical-displacement contour in the dry simulation, indicated by the heavy line in Fig 4.9b. Also shown in Fig. 4.9b are contours of the horizontal velocity field at time 4 hours. (As in Fig. 4.2 the 2 hour offset between the dry and reference simulation was taken to account for the slower evolution of the squall line in the reference simulation.) The vertical displacement of an air parcel that ends up at the final position (x_f, z_f) at time $t = t_f$ is determined by first following the trajectory of that air parcel backward to time $t = 0$ to determine the initial position of the parcel, (x_o, z_o). The vertical displacement is then given by $z_f - z_o$. If x_o is beyond the right edge of the computational domain, z_o is assumed to be the same as the height of the parcel when it entered the domain.

Comparing Figs. 4.9a and 4.9b reveals that the vertical displacement field in the dry simulation is most conducive to the production and transport of condensate into the regions where the trailing and leading anvils form in the reference simulation. Furthermore, the shape and vertical extent of both the leading and trailing features agree in the two simulations. As in the reference simulation, the air which undergoes large vertical displacement in the region of diabatic heating is advected by the perturbed flow at upper levels (as shown by the backward trajectories plotted as double grey lines), while the air parcels outside of the

vertical-displacement boundary have back-trajectories (double black lines) suggesting that the motion of these air parcels was produced exclusively by gravity-wave induced velocity perturbations. In both the dry and reference simulations, the gravity waves excited by the thermal forcing produce the LAF and FTRF and these flows advect the diabatically heated and lifted air away from the region of heating. The similarity in the large-scale qualitative structure of the cloud in the reference simulation and the vertical displacement field in the dry simulation suggests that the gravity waves excited by the time-mean thermal forcing in the region of the leading convective line exert a dominating influence on the qualitative structure of the stratiform cloud.

4.4 Cloud-top temperatures

Ogura and Liou (1980) reported a broad horizontal region of negative temperature anomaly at ~200 mb in the stratiform region to the rear of the convection in their observations of the 22 May 1976 squall line and trailing anvil (see their Figure 21). They attributed this cold anomaly to air parcels overshooting into the stratosphere. Gamache and Houze (1985) reported a similar negative temperature anomaly at upper-levels of the trailing stratiform cloud and in the cloud-free post-stratiform region behind the 12 September GATE squall line. Zipser (1988) compared satellite and radar data to show that the coldest cloud tops occurred well away from the region of most vigorous convection, suggesting that the stratiform cooling is not produced by the backward advection of air parcels that overshot their level of neutral buoyancy in the leading line. Johnson *et al.* (1990) suggested that the cold anomaly may be the result of enhanced IR cooling near cloud top. Similar regions of upper-level cooling are, however, generated in numerical simulations that do not include radiative processes. Fritsch and Brown (1982) used numerical simulations to conclude that the cold anomaly is the result of adiabatic expansion and cooling resulting from ascent within the trailing stratiform anvil. The simulations to be discussed in this section suggest that the adiabatic ascent occurs within gravity waves generated by the low-frequency component

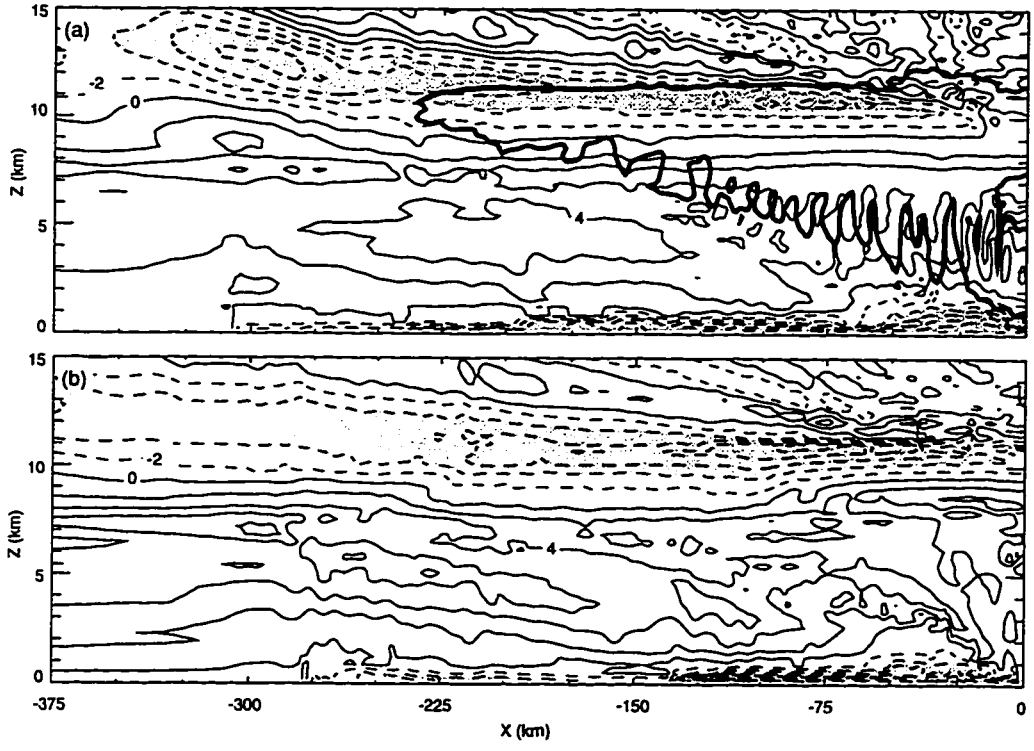

Figure 4.10. Perturbation potential temperature (thin lines, contoured in 2 K intervals) at: (a) t = 6 hours in the reference simulation and (b) t = 4 hours in the dry simulation. Areas where the potential temperature is less than -4 K are shaded. Cloud outline is indicated by the heavy line in (a).

of the thermal forcing at the leading edge of the squall line system, consistent with the the dynamical interpretation of Fritsch and Brown (1982).

Figure 4.10a shows the potential temperature perturbations that develop to the rear of the convective region in the reference simulation. The gust front is at x = 0 km. The negative cloud-top potential temperature anomaly reaches -6 K, comparable to the -6.5 K value reported by Ogura and Liou (1980) (plotted as a 4 °C sensible temperature value in their Fig. 21). The spatial structure of the simulated cold region also agrees with the observations; in both cases the coldest air is located in a thin layer that begins ~50 km behind the gust front and extends rearward.

Figure 4.10b shows the potential temperature perturbation generated by the steady thermal forcing shown in Fig. 4.3a. A comparison of Fig. 4.10a and b reveals both qualitative and quantitative similarity between the dry and reference simulations; both exhibit an upper-level negative potential temperature anomaly centered around $z \sim 11$ km that stretches well behind the gust front. Notice that overshooting cloud tops, which are not present in the dry simulation, are not required to produce the upper-level cooling. Instead, the upper-level cooling develops as a result of adiabatic ascent in motions within gravity waves. The maximum value of the negative potential temperature anomaly in the dry simulation is -10 K. This is greater than the -6 K potential temperature maximum in the reference simulation but, as discussed in Section 4.2.1, a stronger response develops in the dry simulation because the steady thermal forcing used in the dry simulation projects more directly onto the low-frequency gravity wave modes responsible for the mesoscale structure of the squall line. This hypothesis is supported by the fact that although the low-frequency modes have larger amplitude in the dry simulation, the high-frequency gravity wave modes have larger amplitude in the reference simulation. For example, the amplitude of the higher frequency modes propagating through the region centered on x = -100 km, z = 14 km is largest in the reference simulation.

Figure 4.10 shows that the upper-level potential temperature minimum in the stratiform and post-stratiform regions occurs as part of a larger-scale pattern of alternating bands of negative and positive potential temperature that extend up into the lower stratosphere. The slope of these bands is consistent with gravity waves transporting energy away from the convective region. The gravity wave structure of the lower stratosphere is particularly easy to recognize because the waves are almost monochromatic, as in the numerical simulations by Fovell, *et al.* (1992). (The waves in the troposphere are harder to recognize because they are a superposition of many different modes.) For simple monochromatic vertically propagating plane parallel gravity waves, the extrema in the velocity field should be 90°out of phase with the extrema in the θ field. This phase shift can, in fact, be observed in Fig. 4.11, which compares the horizontal velocity and perturbation potential temperature

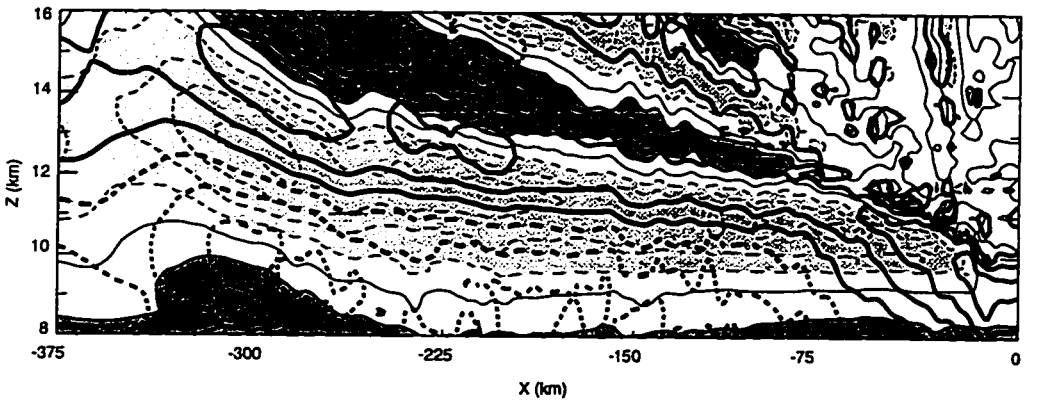

Figure 4.11. Contours of potential temperature (thin lines, contoured as in Fig. 4.10) and horizontal velocity (thick lines, contoured in 5 m s^{-1} intervals) at $t = 6$ hours in the reference simulation. Light and dark shading indicate θ' <-2 K and θ' >2 K, respectively.

in the reference simulation. A similar result holds for the dry simulation, although, as already discussed, the amplitudes of the perturbations are somewhat less above $z = 12$ km.

Chapter 5

SENSITIVITY STUDIES IN TWO DIMENSIONS

Chapter 4 demonstrated that the kinematic and thermodynamic features around squall lines are the result of gravity waves generated by the time-mean thermal forcing in the leading convective line. Gravity waves are influenced by both the environment through which they propagate and the shape and magnitude of the thermal forcing that generates them. In this chapter, the way in which changes in the propagation of gravity waves influences the mesoscale circulation around squall lines is investigated. Section 5.1 examines the effect that varying the magnitude of the thermal forcing has on the meso-γ-scale vertical velocity field in the leading line. Section 5.2 investigates the question of whether or not the gravity waves are linear. The relative importance of stratiform and convective heating is considered in Section 5.3. Finally, Section 5.4 investigates the effect that varying either the environment or the thermal forcing has on the gravity waves that determine the meso-β-scale circulation around squall lines.

5.1 Development of updraft cells from a steady heat source

Observations and numerical simulations indicate that the convection in mature squall lines is often composed of a number of individual cells with horizontal and temporal scale much less than that of the squall line itself. Dudhia *et al.* (1987) reported that the cells in their numerical simulation periodically detached themselves from a persistent low-level updraft and drifted rearward through the storm. They speculated that the periodic formation of new cells might be either a gravity-wave phenomenon or a microphysical phenomenon related to the rate of rain production. Fovell and Ogura (1988) suggested that the decay of an older cell results from the formation of a new cell which cut off the moisture supply to

the older cell, but didn't explicitly describe the mechanism responsible for the formation of a new cell. Rotunno *et al.* (1988) attributed the periodicity in cell formation to new cells being forced by the rain-produced cold pool surging out from previously generated cells. More recently, Yang and Houze (1995a) noted that there were no pulsations in the strength of the updraft at the leading edge of the cold pool in their simulations and that cells formed by periodically detaching from the steady updraft. They showed that the amplitude and vertical structure of the velocity perturbations associated with these cells could be successfully reproduced using a linear model in which the horizontal wavelength and phase speed of the cells as well as the vertical profile of the latent heating were specified using data from a nonlinear simulation. Yang and Houze concluded on the basis of this linear analysis and the polarization of the velocity and pressure fields in nonlinear simulations that the cells were resonant trapped gravity waves.

Figure 5.1a shows the vertical velocity that develops in the dry simulation, which is forced by the steady pattern of heating and cooling shown in Fig. 4.3a. The vertical velocity field (thin lines) exhibits structure on a much finer spatial scale than the applied thermal forcing (thick lines). Cells appear in the vertical velocity field that resemble the vertical velocity cells in multicell squall lines, although their evolution is more chaotic than that of the cells in the reference simulation or in observations of actual squall lines. Gallus and Johnson (1995a) also noted some tendency for cellularity in the vertical velocity field in their numerical simulations even when the thermal forcing was steady, but they didn't explore the issue further. Figures 5.1b, c, and d show the vertical velocity generated when the thermal forcing is reduced in magnitude. The cells vanish when the amplitude of the thermal forcing is reduced by a factor of 10 (Fig. 5.1c), but some cellularity remains when the thermal forcing is reduced in amplitude by a factor of 5 (Fig. 5.1b). When the thermal forcing has infinitesimal amplitude, so that the linear approximation is valid (Fig. 5.1d), the vertical velocity field is smooth and noncellular. The vertical velocity shown in Fig. 5.1d was computed using the fully linear model discussed in Chapter 3.

The simulations shown in Fig. 5.1 demonstrate that a steady thermal forcing, with a

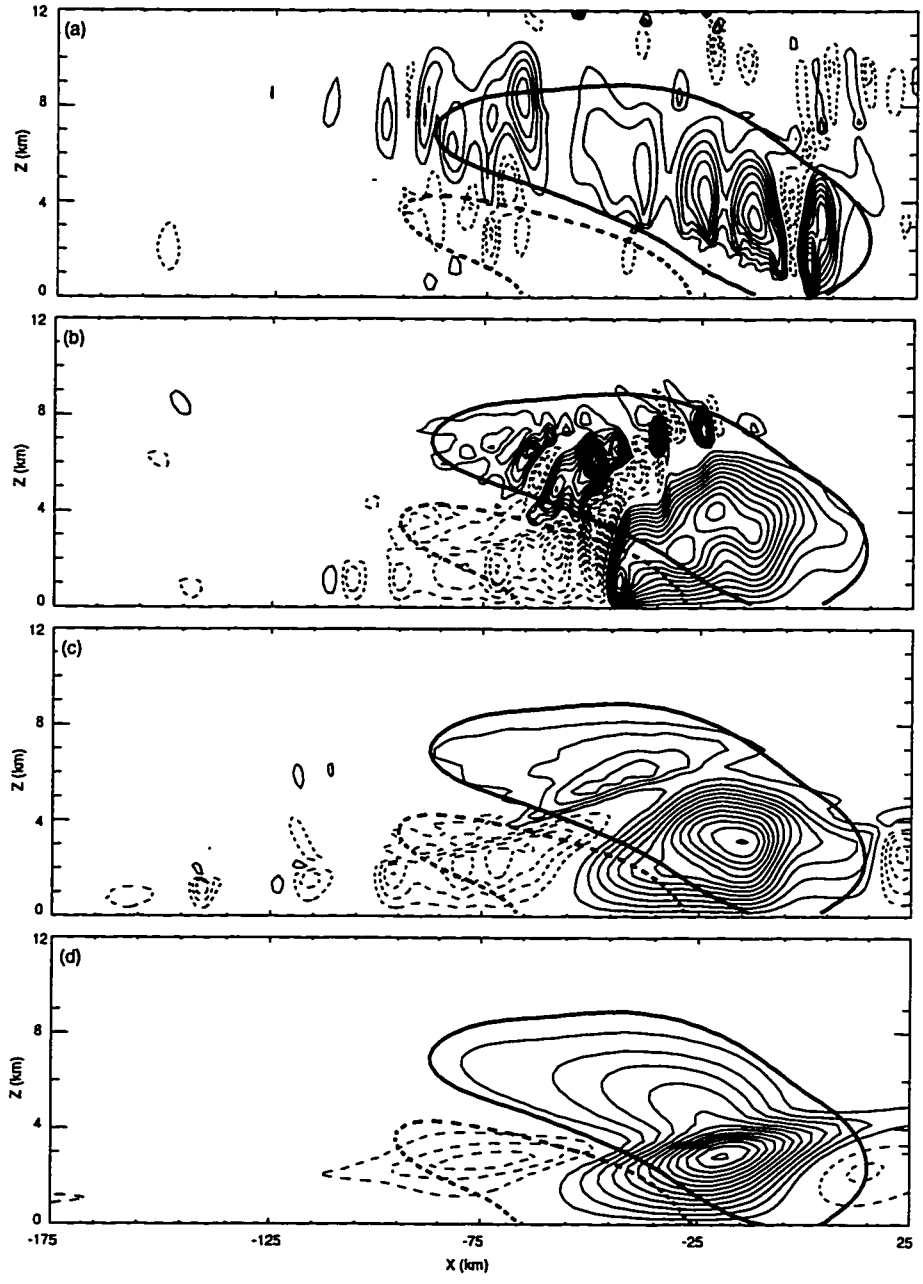

Figure 5.1. Vertical velocity (thin lines) and thermal forcing (thick lines) in: (a) the dry simulation, (b) a nonlinear simulation with thermal forcing reduced by a factor of 5, (c) a nonlinear simulation with thermal forcing reduced by a factor of 10, and (d) a linear simulation with the thermal forcing as in (a). Contour interval on w is 0.5 m s^{-1} in (a), 0.1 m s^{-1} in (b), 0.05 m s^{-1} in (c), and 0.5 m s^{-1} in (d). Contours of the thermal forcing are $\pm$ 0.001 in (a), $\pm$ 0.0005 in (b), $\pm$ 0.0001 in (c), and $\pm$ 0.001 in (d).

magnitude characteristic of that present in the low-frequency components of actual squall lines, is sufficient to generate cellular updrafts in nonlinear simulations. No temporal variations in the forcing are required to produce these cells; instead, vertical velocity cells are an inevitable nonlinear consequence of a steady thermal forcing with sufficient magnitude. In actual squall lines, this unsmooth and unsteady response to the steady thermal forcing may the gravity waves modes associated with the rearward cell propagation that Yang and Houze (1995a) identified as resonant.

5.2 Are the wave dynamics linear?

If much of the mesoscale structure associated with squall lines is determined by gravity waves forced by the low-frequency component of the latent heating and cooling at the system's leading edge, one might ask to what extent these gravity waves can be described by linear dynamics. In order to investigate this question, a linear model (described in Chapter 3) was used to simulate the response of a Boussinesq atmosphere to the same thermal forcing used in the dry simulation. The linear model was integrated with the thermal forcing shown in Fig. 4.3a and no microphysical parameterization. The mean-state stability and horizontal winds were identical to those in the dry simulation, shown in Fig. 4.1.

The total horizontal velocity ($\bar{U} + u'$) that develops in the linear simulation is shown in Fig. 5.2, which can be compared to the corresponding nonlinear result shown in Fig. 4.2b. At upper levels the linear solution agrees reasonably well with the nonlinear solution; above $z > 6$ km, an FTRF is visible for $x <$ -75 km and a rear-to-front flow appears that is similar to the LAF for $x > 0$ km. Below 6 km, however, the flow in the linear simulation differs dramatically from that in the nonlinear simulation. There is some indication of a RI in the linear solution but it does not descend toward the gust front in a realistic manner and the low-level outflow behind the gust front is completely absent in the linear solution. In an attempt to determine why the linear model failed to adequately reproduce the flow below $z = 6$ km, an additional linear simulation was conducted with the basic state modified

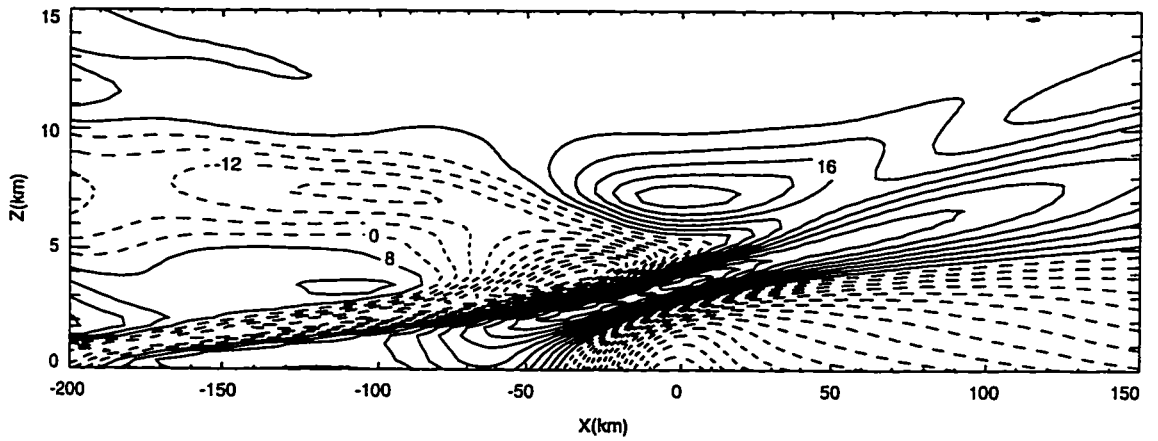

Figure 5.2. Horizontal velocity (contoured in 4 m s^{-1} intervals) generated by the thermal forcing shown in Fig. 4.3a at time $t = 3$ hours in a linear simulation.

so that the temperatures below $z = 1.5$ km matched those in the low-level cold pool that formed in the dry simulation. As in the previous simulation, the basic state remained horizontally uniform. This second linear simulation, shown in Fig. 5.3, did a far better job than the previous linear simulation of reproducing the rear inflow jet and other low-level features of the squall line to the rear of the thermal forcing.

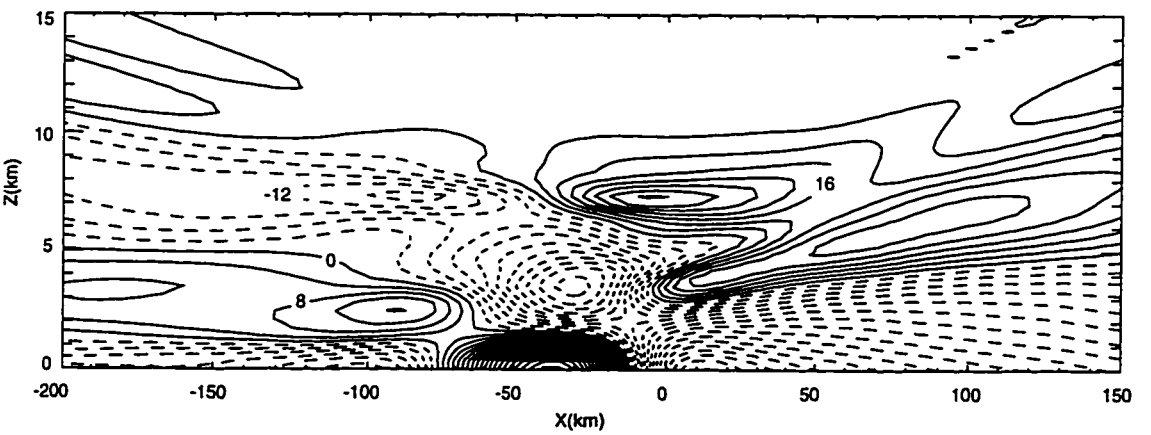

Figure 5.3. Horizontal velocity (contoured in 4 m s^{-1} intervals) generated by the thermal forcing shown in Fig. 4.3a at time $t = 3$ hours in a linear simulation with modified low-level stability.

(Note that the basic state was not modified to incorporate information about the rear inflow jet; the only modification was to include a low-level temperature perturbation.) Thus it appears that the linear model fails to accurately represent the low-level circulations because it cannot account for the local modification of the basic state stability associated with the development of the low-level cold pool.

5.3 Convective versus stratiform thermal forcing

Houze (1982) and Johnson and Young (1983) analyzed the vertical distribution of heating for the entire leading line/trailing anvil system. Houze (1982) noted that large-scale upward motion must occur to balance the upper level heating. Gallus and Johnson (1992) concluded that latent heat absorption and release in the trailing anvil leads to the formation of a midlevel mesolow which is sufficiently strong to drive the RI. Yang and Houze (1995b) have concluded that the addition of a bulk-ice microphysical parameterization to a warm-rain cloud model leads to a more realistic RI and asserted that the descending nature of the RI is a result of latent cooling associated with evaporation and sublimation within the trailing stratiform region. Zhang and Gao (1989) also pointed out the importance of melting and evaporative cooling in the stratiform region in producing a descending RI. The extent to which in situ microphysical forcing dominates the overall dynamics in the trailing anvil has, however, remained an open question. In more recent work, Gallus and Johnson (1995a and b) performed a series of simulations of the stratiform region using specified one-dimensional profiles of thermal forcing and hydrometeor advection meant to represent inputs from the convective region at the lateral boundary of a two-dimensional kinematic cloud model. They concluded that ice processes within the stratiform region were an important dynamical contribution to the circulation that developed in their model of the stratiform region.

On the other hand, many previous numerical and observational studies have specifically attributed the development of the RI to dynamical forcing from within the convective line

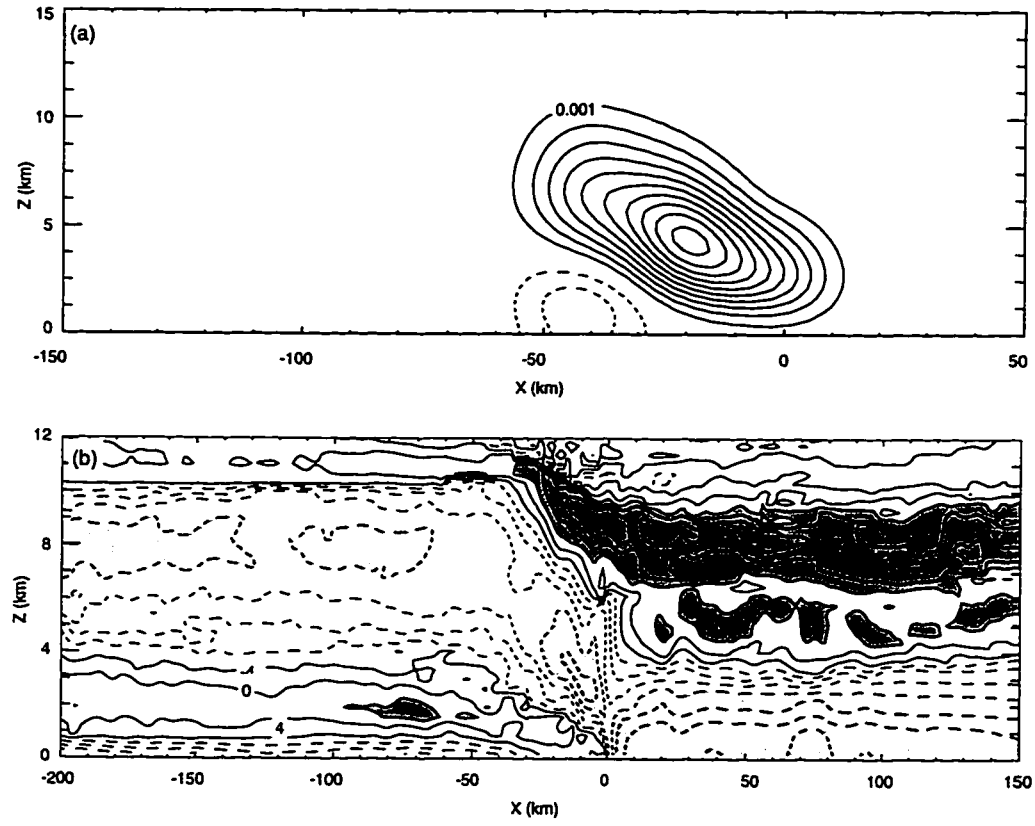

Figure 5.4. (a) Time-mean thermal forcing meant to represent the forcing from the leading convective line alone (contours as in Fig. 4.3a). (b) Horizontal velocity at time = 6 hours generated by the thermal forcing in (a). Horizontal velocity contours and shading are as in Fig. 4.2. Note the difference in horizontal scale between in Fig. 5.4a and Fig. 5.4b.

(Smull and Houze 1987b; Lafore and Moncrieff 1989; Weisman 1992; Klimowski 1994). An additional dry simulation was, therefore, performed with the modified thermal forcing shown in Fig. 5.4a in order to investigate the relative importance of the stratiform and convective heating. Although there is no completely satisfactory procedure for splitting the total thermal forcing into convective and stratiform components, an attempt was made as follows. The instantaneous latent heating and cooling from time 4.5 to 6.5 hours in the reference simulation was averaged, and any heating or cooling rearward of x = -50 km was neglected in order to isolate the convective elements of the leading line. The resulting field

was then smoothed and scaled in the same way as the thermal forcing used in the original dry simulation. This smoothing smears the thermal forcing slightly ahead of $x = 0$ km and rearward of x = -50 km.

The thermal forcing in Fig. 5.4a consists of a heating region that slants backward over a low-level cooling formed by the evaporation of precipitation. Although the 50 km wide scale of the thermal forcing is clearly wider than an individual convective element, updrafts exceeding 3 m s^{-1} were visible in the reference simulation throughout this entire 50 km wide region. This is roughly consistent with the analysis of Smull and Houze (1987a), who found an approximately 40 km wide convective region in their observational study of the 22 May 1976 squall line (see their Fig. 3). Note also that the quasi-horizontal pattern of heating overlying cooling apparent in the region x < - 60 km of the thermal forcing used in the dry simulation (Fig. 4.3a) has been eliminated from the thermal forcing shown in Fig. 5.4a.

The response to the thermal forcing shown in Fig. 5.4a is shown in Fig. 5.4b and can be compared to the response in the dry simulation, shown in Fig. 4.2b. The overall qualitative structure of the flow is similar in the two figures; thus the thermal forcing from the leading convective line is sufficient to generate the FTRF, the RI and the LAF. The amplitudes of the FTRF, RI and LAF are smaller than in the dry simulation, indicating that thermal forcing in the stratiform region does augment and modify the stratiform circulation. This is consistent with the results of Yang and Houze (1995b), Zhang and Gao (1989), and Gallus and Johnson (1992, 1995a, and 1995b) who suggested that local microphysical processes can influence the trailing anvil circulation. In both dry simulations (Figs. 5.4b and 4.2b) the RI does not descend to the surface until it nearly reaches the gust front, whereas in the reference simulation (Fig. 4.2a) the RI descends over its entire 200 km length. This suggests that the realistic descent of the RI may depend on latent heating and cooling in the stratiform region that is so weak it fell below the threshold for inclusion in the thermal forcings used in the two dry simulations. Nevertheless, these results suggest that the thermal forcing from the leading convective line provides the *primary* forcing for the

RI, FTRF, and LAF.

5.4 Sensitivity to the environment and the thermal forcing

The results of the previous sections demonstrate that gravity waves forced by the time-average pattern of latent heating and cooling in and near the leading convective line can generate the basic structures in the trailing stratiform anvil. The gravity waves themselves are influenced by both the environment through which they propagate and the pattern of latent heating and cooling that forces them. Additional numerical simulations were performed in order to investigate the sensitivity of the mesoscale storm structure to changes in the large-scale environment and the thermal forcing. The large-scale environment and the applied thermal forcing were varied independently in these sensitivity studies. It should be noted, however, that in real squall lines, changes in the large-scale environment can influence the latent heating and cooling of the convective line. For example, Rotunno *et al.* (1988) have discussed how the environmental wind shear and CAPE affect the orientation of the updraft at the leading edge of the gust front and thereby influence the distribution of the thermal forcing. The following section should, therefore, be understood to examine only one aspect of the sensitivity of the squall line to the environment, namely the extent to which a hypothetical fixed thermal forcing would generate different mesoscale circulations in different environments.

5.4.1 Sensitivity to the environment

Figure 5.5 illustrates the influence of variations in the large-scale environment on the horizontal velocity field generated by the thermal forcing shown in Fig. 4.3a. In Fig. 5.5b the initial profile of the horizontal wind was the same as in the dry simulation, but the initial thermodynamic profile was modified so that the Brunt-Väisälä frequency was 0.01 s^{-1} below 2 km. This modification eliminates the well mixed layer of constant $\bar{\theta}$ near the surface. The flow behind the thermal forcing in Fig. 5.5b looks very similar to the flow in the dry

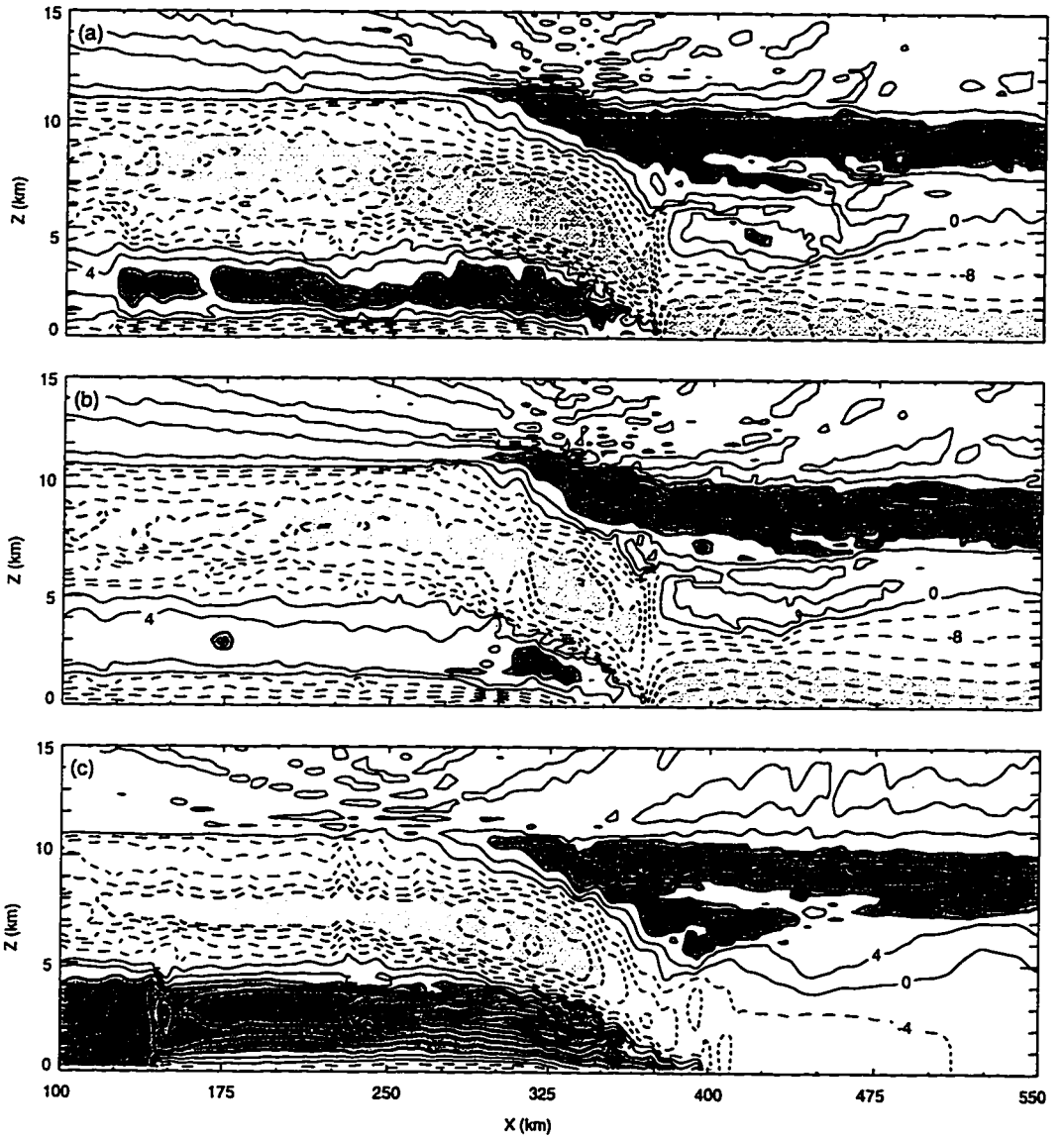

Figure 5.5. Horizontal flow at time $t = 6$ hours arising from the thermal forcing shown in Fig. 4.3a in: (a) the dry simulation, (b) a simulation with modified low-level Brunt-Väisälä frequency, and (c) a simulation with modified low-level winds. Contours and shading are as in Fig. 4.2.

simulation (shown in Fig. 5.5a) except at low levels where the increased stability seems to weaken the flow (compare, for example, the RI in the two figures). Gallus and Johnson (1995b) found a similar decrease in the magnitude of the flow when they increased the

initial stability in their numerical simulations of the stratiform region of the 10-11 June squall line. Ahead of the thermal forcing, the LAF is slightly stronger in Fig. 5.5b. An additional simulation was performed with the initial Brunt-Väisälä frequency given by $N = 0.01\ s^{-1}$ throughout the entire depth of the model domain in order to examine the effect of variations in the upper-level stability. The flow that developed was very similar to the flow in Fig. 5.5b, suggesting that changing the upper-level stability doesn't strongly affect the circulation. Further, since the assumption of uniform Brunt-Väisälä frequency precludes the accurate representation of a tropopause, the similarity of the $N = 0.01\ s^{-1}$ experiment to that shown in Fig. 5.5b implies that the vertical extent of the circulation generated by the thermal forcing is not limited by the tropopause. This result will be explored in more detail in Section 5.4.3.

In Fig. 5.5c, the initial stability is the same as in the dry simulation, but the low-level shear in the initial wind was removed, instead $\bar{U}$ was 1 m s^{-1} at all heights. The flow in Fig. 5.5c is comparable to the flow in the dry simulation, shown in Fig. 5.5a, except in the lowest levels where the lack of an opposing wind exaggerates the strength of the RI and creates a gust front that runs out ahead of the storm. The difference in the low-level velocities in Figs. 5.5a and c is, in fact, comparable to the difference in the mean wind between the two simulations.

5.4.2 Sensitivity to the thermal forcing

In order to examine the sensitivity to the thermal forcing in a systematic way, an easily varied analytic thermal forcing was developed. (This forcing is described in the Appendix) Figure 5.6a shows the horizontal flow (thin lines) at $t = 6$ hours generated by this thermal forcing (thick lines). Like the thermal forcing shown in Fig. 4.3a, the thermal forcing in Fig. 5.6a consisted of a backward slanting region of heating trailed by a more compact backward slanting region of cooling. Note that the flow in Fig. 5.6a resembles the circulation around a squall line.

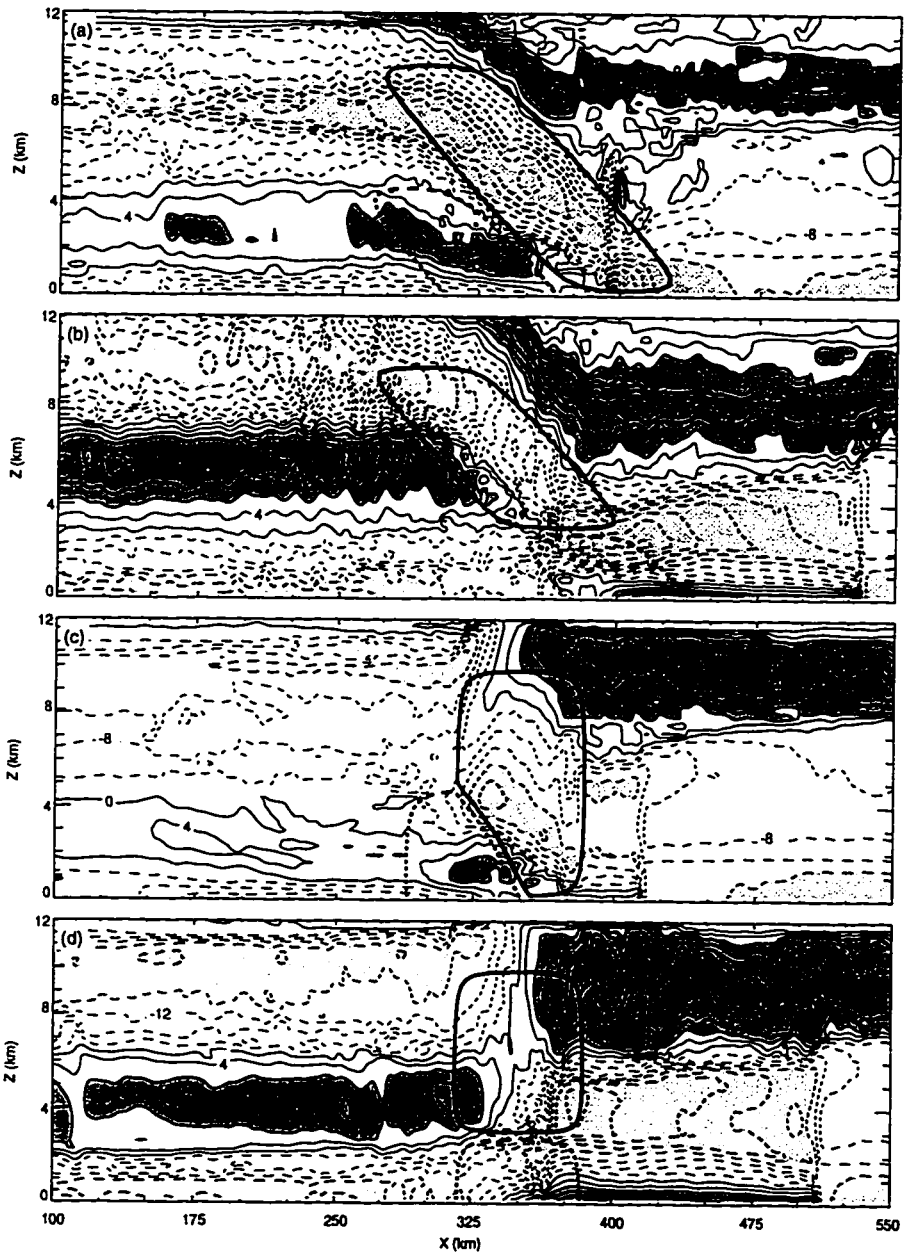

Figure 5.6. Horizontal perturbation velocity (thin lines) generated by four distinct patterns of thermal forcing (thick lines) at $t = 6$ hours. Horizontal velocity contours and shading are as in Fig. 4.2. Thermal forcing contours are ± 0.001 K s^{-1}

Figure 5.6b shows the flow that resulted when the thermal forcing was modified so that the region of cooling was aligned along the same sloping axis as the region of heating. The flow that developed from this thermal forcing is qualitatively different from the flow shown in Fig. 5.6a, especially at low levels. The RI in Fig. 5.6b never descends to the surface as it does in the more representative flow shown in Fig. 5.6a. Ahead of the thermal forcing, there is a low-level region of rear-to-front flow that is not present in the 22 May 1976 squall lines or in Fig. 5.6a. Above this, Fig. 5.6b shows that the LAF extends to lower altitudes than in Fig. 5.6a.

The thermal forcing used in the simulation shown in Fig. 5.6c was identical to the thermal forcing indicated in Fig. 5.6a, except for the removal of the backward tilt to the heating and cooling. The most striking feature of the flow in Fig. 5.6c is the lack of any organized or coherent FTRF. At lower levels to the rear of the forcing, there is a region of RI, but it is relatively weak. Unlike the flow in Fig. 5.6b, however, the RI does descend to the surface. The LAF is too strong and there is a shallow low-level rear-to-front flow ahead of the region of heating.

Finally, Fig. 5.6d shows the flow that resulted when the cooling underlay the heating and both features lacked a backward tilt. As in Fig. 5.6b, the flow in Fig. 5.6d has an elevated RI that never descends to the gust front. The upper-level front-to-rear flow is stronger and better organized than in Fig. 5.6c, but the low-level rear-to-front flow is excessive and the upper-level LAF extends too low. Finally, the upper-level FTRF to the rear of the thermal forcing never connects to the flow ahead of the heating as it does in the 22 May 1976 squall line and in the flows in Figs. 5.6a, b, and c.

A circulation including a FTRF, LAF, and RI like that observed in the 22 May 1976 squall line only develops when the applied heating and cooling have the pattern shown by the heavy lines in Fig. 5.6a, suggesting that the mesoscale circulation is strongly influenced by the shape and structure of the applied thermal forcing. In contrast, the circulation in the mesoscale region surrounding the squall line shows much less sensitivity to variations in the mean-state environment. Figures 5.5a-c show that varying the mean-state stability and

winds alone, while leaving the thermal forcing unchanged, varies the strength of the FTRF, LAF and RI, but does not fundamentally change the qualitative pattern of the mesoscale circulation. In real squall lines, however, changing the mean state environment may alter the distribution of latent heating and cooling within the region of the leading line. Given the results of these sensitivity studies, it appears that changes in the mean state environment will primarily influence the mesoscale circulation by changing the thermal forcing, rather than by affecting the propagation of low frequency gravity waves generated by the thermal forcing.

Gallus and Johnson (1995a and b) reported that thermal forcing from the convective line alone didn't generate a realistic circulation in the stratiform region. The apparent contradiction between their conclusions and our results can be reconciled on the basis of the sensitivity tests discussed here. As mentioned earlier, Gallus and Johnson modeled only the trailing anvil and specified a profile of heating and cooling along the upstream boundary to represent the thermal forcing from the convective line. The vertical profile of their specified heating and cooling was based on a heat budget derived from observations of a squall line (see Fig. 2b in Gallus and Johnson 1995b). Given the sensitivity of the circulations in the stratiform region to small changes in the thermal forcing, their vertical, one-dimensional profile of heating and cooling may not have been sufficient to generate a realistic flow in the trailing stratiform anvil.

5.4.3 Vertical extent of the anvil cloud

It was noted in Section 5.4.1 that removing the tropopause had almost no effect on the vertical extent of the mesoscale circulation generated by thermal forcing which suggests that the height of the top of anvil cloud might be relatively insensitive to the height of the tropopause. This hypothesis can be tested by comparing two microphysical squall line simulations: one with and one without a tropopause.

The initial potential temperature profile used in these simulations was adapted from the

widely used idealized midlatitude sounding of Weisman and Klemp (1982), such that

$$\bar{\theta}(z) = \begin{cases} \theta_o + (343\,\mathrm{K} - \theta_o)\left(\frac{z}{12\,\mathrm{km}}\right)^{5/4} & \text{if } z \le z_{tr} \\ \left(\left(\frac{z_{tr}}{12\,\mathrm{km}}\right)^{5/4} - 1\right)(343 - \theta_o) + 343\,\mathrm{K}\,\exp\left[\frac{g}{C_p 243\,\mathrm{K}}(z - z_{tr})\right] & z > z_{tr}, \end{cases} \tag{5.1}$$

where z_{tr} indicates the height of the tropopause and θ_o is the potential temperature at the surface. The initial profile of relative humidity was as given in Weisman and Klemp (1982), and the mixing ratio was not allowed to exceed .016 at low levels. The initial profile of the winds was also based on profiles used in Weisman and Klemp (1992), and is given by

$$\bar{U} = U_o\left(\tanh\left(\frac{z}{z_u}\right) - 1\right), \tag{5.2}$$

where $U_o = 12$ m s^{-1} and $z_u = 3$ km.

Figure 5.7a shows the horizontal velocity (thin lines) and cloud outline (thick lines) 6 hours into the simulation of a storm where the tropopause was eliminated by setting $z_{tr} = \infty$ in (5.1). The horizontal velocity field shows all the expected features of a squall line and the mesoscale cloud top is fairly uniform at $z \sim 11$ km except in the overshooting cloud tops of the region of active convection ($x \sim 390$ km). Figure 5.7b shows the flow and cloud outline in a simulation with the height of the tropopause set to 10 km. The presence of the stratosphere in this second simulation has very little effect on the squall line. In particular, the top of the anvil cloud is again found at approximately 11 km. Recall that the vertical extent of the quasi-horizontal disturbances generated by the idealized small-amplitude heating profiles shown in Figs. 1.1 and 4.7 are determined exclusively by the depth of the thermal forcing. It appears that the depth of the thermal forcing is also the primary factor determining the height of the anvil cloud in these moist simulations. As indicated by the height of the overshooting cloud tops in Figs. 5.7a and 5.7 b, the depth of the main convective towers in the leading line is similar in both simulations and, according to the preceding hypothesis, there should be little change in the elevation of the top of the anvil cloud. Moreover, when the depth of the convective towers was reduced in an additional simulation (not shown) in which the tropopause was lowered to 8 km, the top

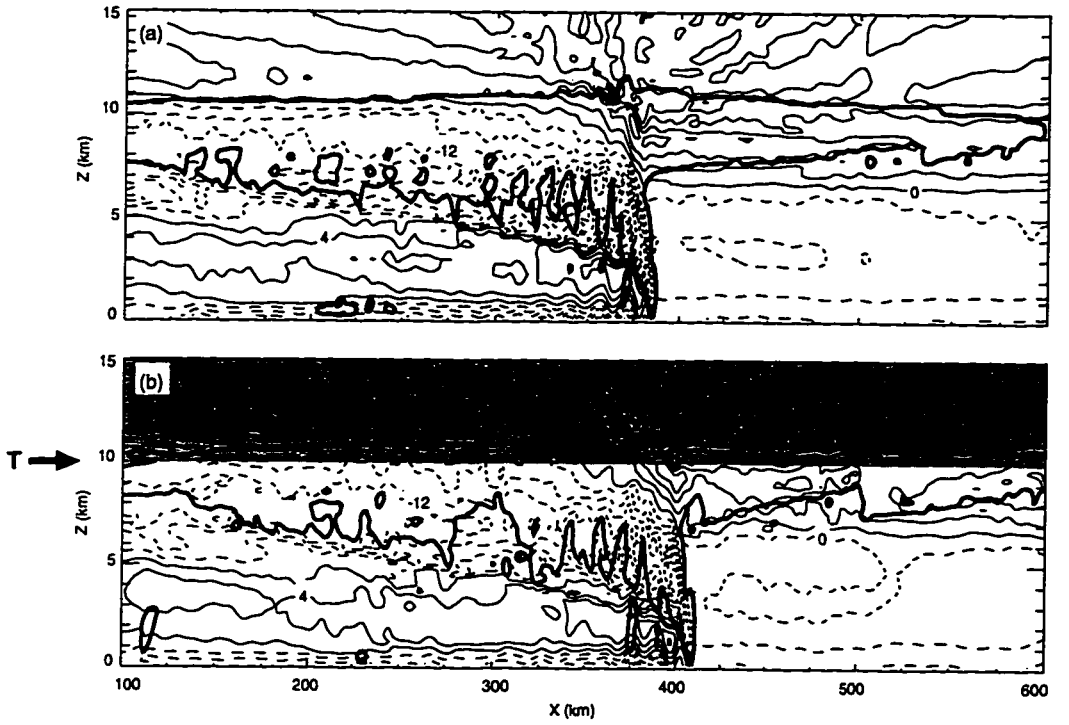

Figure 5.7. Horizontal velocity (thin lines, contoured in 4 m s^{-1} intervals) and cloud outline (thick lines) in "moist" simulations in an environment: (a) with no tropopause and (b) a tropopause at z = 10 km. Shading in (b) indicates the stratosphere.

of the anvil cloud descended to 9 km. Even in this last case, however, the anvil cloud penetrated the stratosphere. Thus, the height of the top of the anvil cloud appears to be primarily determined by the depth of the convection in the leading line. The tropopause influences the height of the anvil only indirectly by limiting the depth of the convection in situations where the tropopause is located well below the level at which air parcels in the main updraft cores return to a state of neutral buoyancy.

Note that the mesoscale cloud top in Fig. 5.7b lies above the tropopause, suggesting a large area of cloudiness can occur within the stratosphere. Although this storm is a simulated one, the real occurrence of such a system might be important in understanding the exchange of water vapor across the tropopause.

Chapter 6

THREE-DIMENSIONAL CIRCULATION AROUND SQUALL LINES

Chapters 4 and 5 suggest that the line-normal circulation around squall lines is the result of gravity waves generated by the time-mean pattern of latent heating and cooling released and absorbed in the leading convective line. This conclusion was reached primarily through the comparison of two *two*-dimensional simulations: a "moist" simulation in which the circulation develops in response to the parameterized microphysical processes, and a "dry" simulation in which the circulation develops in response to a constant thermal forcing and there are no microphysical processes. Real squall lines, however, are three-dimensional. In order to extend the conclusion of Chapters 4 and 5 to real squall lines, it is necessary to repeat the comparisons of dry and moist simulations using fully *three*-dimensional simulations. In addition to verifying that the line-normal circulation of squall lines is the result of gravity wave propagation, the three-dimensional simulations will allow us to investigate components of the circulation around squall lines that aren't addressed by the quasi-two-dimensional conceptual model.

The attempt to perform parallel dry and moist simulations in three dimensions introduces some computational issues which are discussed in Section 6.1. The dry and moist simulations are compared in Section 6.2. Section 6.3 investigates the sensitivity of the circulation to variations in the thermal forcing, and Section 6.4 examines how the Coriolis force influences the propagation of the gravity waves generated by the thermal forcing.

6.1 Accuracy of the numerical models

Because of limited computational resources, some of the simulations presented in this chapter were performed using smaller domains and coarser resolutions than the two-dimensional simulations presented in Chapters 4 and 5. A smaller domain increases the likelihood that errors from the open computational lateral boundaries, which are meant to account for the the fact that the computational boundaries are artificial and do not correspond to physical boundaries, will influence the solution in the interior of the domain. Because the model is unable to resolve features with a horizontal length scale comparable to Δx and Δy, coarse resolution can lead to increased errors in the simulation. Increasing either the domain or the resolution increases the number of model grid points at which the basic equations must be evaluated and integrated and, therefore, increases the computational cost of the simulation. In the two-dimensional simulations presented in Chapters 4 and 5 domains and resolutions sufficient to accurately reproduce the circulation around squall lines were computationally affordable. (We were able to continually increase the resolution and domain size until we found no additional change in the large-scale circulation with further increases in the resolution and/or domain size). Three-dimensional simulations with a similar resolution and a comparable domain are, however, prohibitively expensive. As an example consider the effect of increasing the horizontal resolution: in a two-dimensional simulation the number of model grid points increases linearly with horizontal resolution, while in three dimensions the number of model grid points increases as the square of the horizontal resolution.

Some of the cost associated with increasing the domain and resolution can be mitigated by nesting grids of different horizontal resolutions. In the region of most physical interest, a fine grid is used to achieve the greatest accuracy. The fine grid is embedded in a coarser grid which allows the computational boundaries to be moved farther away at a lower computational cost than extending the fine grid the same distance. Use of nested grids is particularly well suited to the investigation of the mesoscale circulation around squall lines.

The convective region, which is dominated by motion on small horizontal scales, can be modeled with the finer resolution grid while the trailing stratiform anvil, where the motion is of a larger horizontal scale, can be modeled using a coarser resolution grid. The basic equations of the nested model are described in Section 3.3 and details of the nesting are described by Skamarock and Klemp (1992). A parameterization of convection has not yet been developed for this model, however, so the nested grid model was only used for those simulations performed dry (*i.e.* with no microphysical forcing).

Even with the nesting, however, we were unable to use as fine a resolution in the three-dimensional simulations as in the two-dimensional simulations presented in Chapters 4 and 5. In the dry simulations presented in this chapter, a coarse grid with $\Delta x = \Delta y = 9$ km was used. In the region of the applied thermal forcing the resolution increased to $\Delta x = \Delta y =$ 3 km. Since even this resolution is significantly coarser than the resolution in the two-dimensional simulations, it is worth investigating the effect of the decreased resolution on the circulation around the squall lines. In addition, the nested grid model uses a slightly different form of the basic equations than the model without nesting, so it is worthwhile to compare the two models.

Figure 6.1a shows the u field generated by the thermal forcing shown in Fig. 5.4a at 6 hours in a simulation performed using the two-dimensional model described in Section 3.2 and used in Chapters 4 and 5. This simulation differs from the one shown in Fig. 5.4b only in the horizontal resolution; the horizontal resolution is $\Delta x = 3$ km in Fig. 6.1a and $\Delta x = 1$ km in Fig. 5.4b. Examining Fig. 6.1a reveals that the coarser horizontal resolution is capable of reproducing the *qualitative* characteristics of the flow around squall lines, including the FTRF, RI and LAF. Comparing the circulation in Fig. 6.1a to that in Fig. 5.4b reveals that the circulation in the coarser horizontal resolution differs *quantitatively* from the circulation in the finer horizontal resolution simulation. In particular, the RI is much weaker in the simulation performed at low horizontal resolution. The FTRF and LAF are also affected by the coarser resolution, with the FTRF weakened slightly and the LAF strengthened. The coarse resolution simulation shows significantly less fine-scale structure

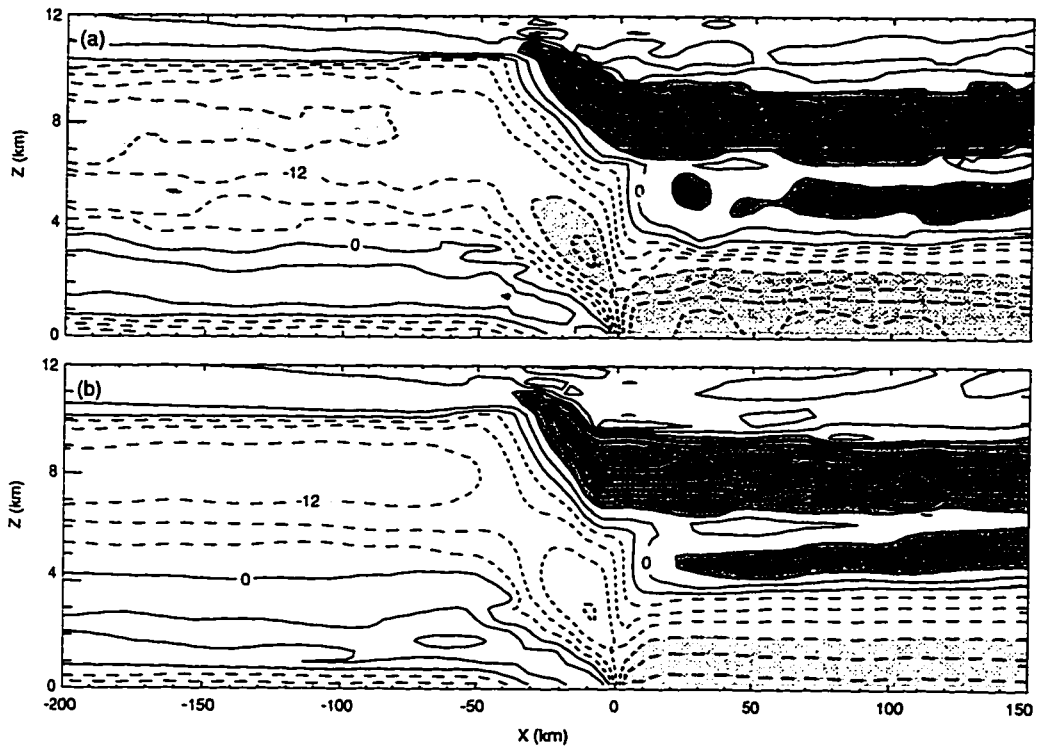

Figure 6.1. The x component of the velocity generated by the thermal forcing shown in Fig. 5.4a 6 hours into a simulation performed with (a) the two-dimensional model using a horizontal resolution of 3 km, (b) the three-dimensional nested model (run without nesting) using a horizontal resolution of 3 km. Contours and shading as in Fig. 4.2.

as well.

Figure 6.1b shows the u velocity at time 6 hours in a simulation performed using the three-dimensional nested grid model described in Section 3.3. To make the circulation two-dimensional and facilitate comparison to Fig. 6.1a, the simulation was performed with periodic boundaries at $y = 0$ km and $y = 12$ km, and the thermal forcing was uniform in the y direction and had the x-z profile shown in Fig. 5.4a. Because the nested grids must lie entirely within the coarse grids and cannot extend to the boundaries, a nested grid couldn't be used without ruining the simulations two-dimensional character. Instead, the simulation was performed using a single grid with a resolution of $\Delta x = \Delta y = 3$ km, which is the same as the resolution used on the finest grid in the simulations discussed later

in this chapter. The initial conditions, time-steps, and boundary conditions were the same as in the simulation shown in Fig. 6.1a. The u velocity in Fig. 6.1b shows all the features of the circulation around squall lines, including the FTRF, RI and LAF. Comparing the circulation in the nested model to that in the model without nesting (Fig. 6.1a) shows that the FTRF in the three-dimensional nested model is slightly weaker in magnitude than in the two-dimensional model and that the LAF is slightly stronger. The RI in the two simulations is, however, roughly comparable. This suggests that changing the horizontal resolution has more impact on the simulated circulation than the choice of one of these two numerical models.

6.2 Mesoscale velocity perturbations

This section compares the circulation that develops in two contrasting three-dimensional numerical simulations. The first simulation considered, the "moist simulation", was performed using parameterized warm-cloud microphysics. The second simulation was performed without any microphysical parameterization; instead, a constant thermal forcing was used to generate motion. This simulation will be referred to as the "derived forcing simulation". These simulations and others discussed in this chapter are summarized in Table 6.1.

Because the nested-grid model described in Section 3.3 lacks a working microphysical parameterization, the moist simulation was performed using the numerical model described in Section 3.2. This is the same model that was used to perform the two-dimensional simulations discussed in Chapters 4 and 5. Because this model does not use nested grids, the moist simulation had to be performed on a limited domain in order to be computationally tractable. The domain of the moist simulation was only 300 km in x by 260 km in y by 16.1 km in z. Open boundary conditions were applied at the top, $x = 0$ km, $x = 300$ km, and $y = 260$ km and the flow was assumed to be symmetric about $y = 0$ km. The horizontal resolution was $\Delta x = \Delta y = 2$ km and the vertical resolution was 350 m. The initial

TABLE 6.1
The three-dimensional simulations presented in Chapter 6

Name of Simulation	Microphysics or Thermal Forcing	f	Model Conditions
moist	microphysics	$0\ s^{-1}$	small domain nonnested model symmetric about $y = 0$ km
derived forcing	thermal forcing derived from the moist simulation	$0\ s^{-1}$	large domain nested model
line-shaped forcing	analytic thermal forcing described by (6.1)	$0\ s^{-1}$	large domain nested model
comma-shaped forcing	analytic thermal forcing described by (6.2)	$0\ s^{-1}$	large domain nested model
moist Coriolis	microphysics	$1.0 \times 10^{-4}\ s^{-1}$	small domain nonnested model
derived forcing Coriolis	thermal forcing derived from the moist simulation	$1.0 \times 10^{-4}\ s^{-1}$	large domain nested model

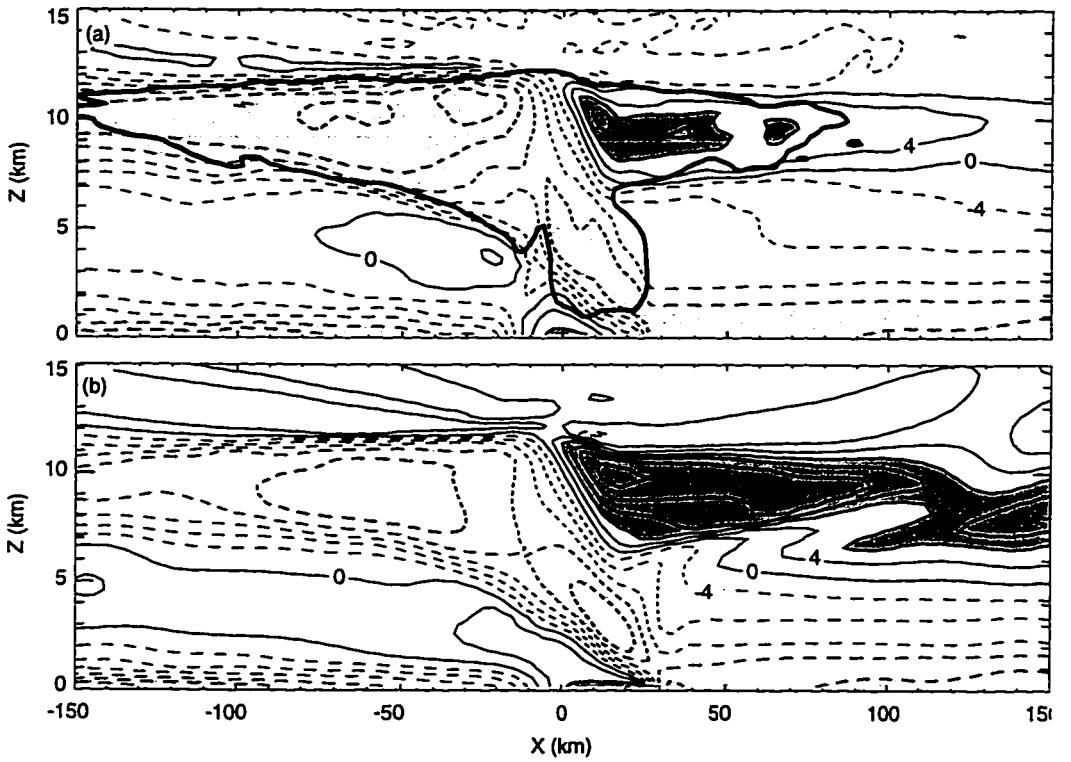

Figure 6.2. The u field averaged from y = -60 km to y = 0 km (a) 4 hours into the moist simulation and (b) 2 hours into the derived forcing simulation. Contours and shading as in Fig. 4.2. Cloud outline indicated by the heavy line in (a).

conditions are those described in Fig. 4.1, and the Coriolis force was neglected. Convection was initiated using three warm bubbles of horizontal radius 10 km and vertical radius 1.4 km, with a peak potential temperature perturbation of 2 K at the bubbles' centers. The bubbles were located along a line 260 km from the western edge of the domain at y = 240, 200, and 160 km.

6.2.1 Line-averaged velocity

Figure 6.2a shows the x component of the velocity in the moist simulation averaged between y = 0 km and y = 60 km. In the moist simulation convection develops in a long line that runs from north to south (*i.e.* parallel to the y axis). Fig. 6.2a can be regarded as a

plot of the along-line average of the line-normal horizontal velocity and can be compared to the conceptual model of the quasi-two-dimensional circulation around squall lines presented in Section 2.1. The line-averaged circulation in Fig. 6.2a shows all the features of the quasi-two-dimensional conceptual model described in Section 2.1 including an FTRF, RI, and LAF. The FTRF in the moist simulation exceeds 24 m s^{-1}, which is comparable to the 25 m s^{-1} maximum FTRF observed by Smull and Houze (1987a) in their dual-Doppler radar analysis of the storm. The RI in the derived forcing simulation is 4 m s^{-1}, significantly weaker than the 17 m s^{-1} maximum observed by Smull and Houze (1987b). The LAF reaches a maximum of 12 m s^{-1}, which is similar to the 10 m s^{-1} reported by Ogura and Liou (1980) in their composite sounding analysis of the 22 May 1976 squall line.

Comparing the line-averaged u field in the three-dimensional simulation to the u field in the the two-dimensional reference simulation (shown at time 4 hours and with a different horizontal scale in Fig. 4.4a) reveals that the FTRF and LAF are similar in the two figures, but that the RI is significantly weaker in the three-dimensional simulation. It should be noted, however, that this comparison is far from exact; the moist simulation was performed with a much smaller domain and a coarser resolution than the two-dimensional reference simulation. As noted in Section 6.1, decreasing the horizontal resolution causes a weakening of the RI. The boundaries of the moist simulation were at x = -150 km and x = 150 km, well within the region of physical interest, which means that errors associated with the lateral boundaries have influenced the circulation shown in Fig. 6.2a. These errors have particularly affected those features that propagate away from the convective line, including the FTRF, RI, and LAF. After 4 hours errors associated with the lateral boundary conditions overwhelm the true solution, effectively limiting the duration of the moist simulation to 4 hours. Nevertheless, at 4 hours the circulation in the moist simulation is qualitatively correct, especially in the interior of the domain.

The sensitivity of the three-dimensional circulation around squall lines to the pattern of latent heat released in the leading convective line was tested by performing a number of dry simulations with different thermal forcings. A good approximation to the circulation

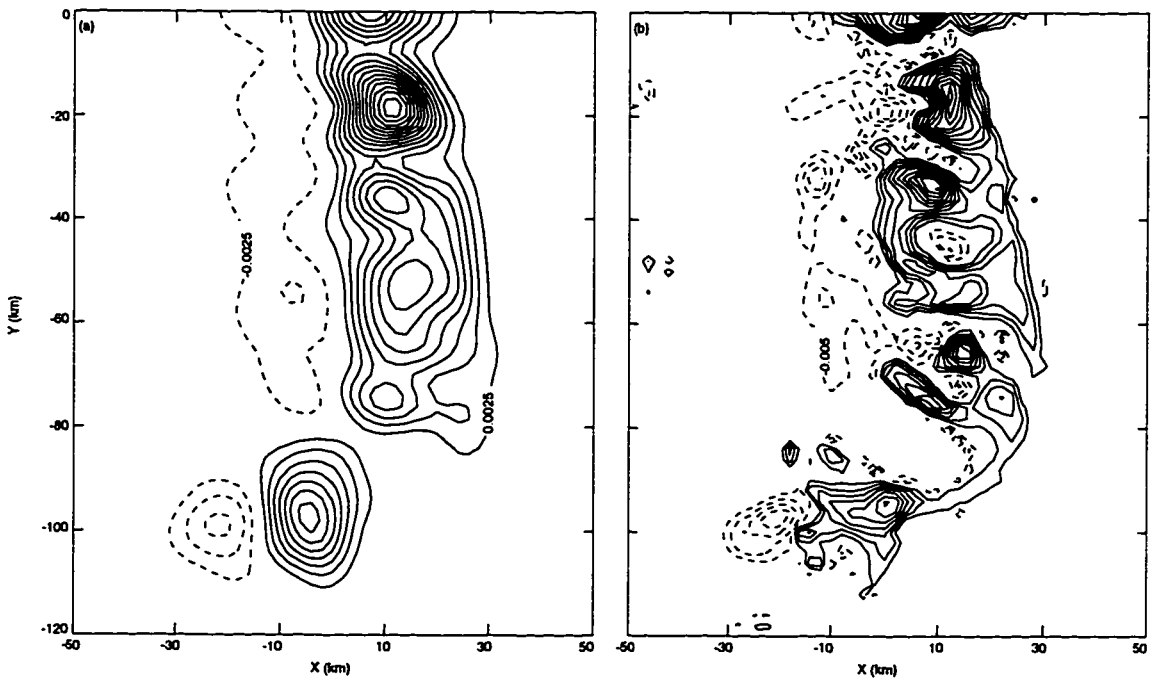

Figure 6.3. (a) The thermal forcing at $z = 3$ km used in the derived heating simulation. (b) The pattern of latent heating and cooling at 3.5 hours in the moist simulation. Contour interval is 0.0025 K s^{-1} in (a) and 0.005 K s^{-1} in (b).

around squall lines was generated by the thermal forcing shown in Fig. 6.3a. This thermal forcing was generated by averaging the instantaneous pattern of latent heating and cooling from the moist simulation, output every 180 seconds, over the period from 3 to 4 hours. The time average was taken in order to eliminate the signature of individual convective cells and to highlight the mature phase of the squall line. Because of the short duration of the moist simulation, however, the time average was only taken over an hour instead of over two hours as in the thermal forcing used in the two-dimensional simulations. In order to eliminate the spurious convection that developed near the boundaries in the moist simulation (discussed in Section 6.2.4) from the time average, any heating or cooling within 100 km of the x boundaries and 30 km of the y = -260 km boundary was ignored in the time average. Residual small-scale cellular structure was removed by running the field 16 times through a second-order smoother. Since smoothing can result in some loss of

amplitude, the integrated absolute value of the smoothed field was then scaled to match the integrated absolute value of the initial, unsmoothed average. The resultant field is shown in Fig. 6.3a; a snapshot of the heating and cooling in the moist simulation is shown in Fig. 6.3b for comparison.

The derived forcing simulation was performed using the nested grid model discussed in Section 3.3. This simulation was performed dry, without any parameterization of microphysical processes; instead, motion was generated by the thermal forcing shown in Fig. 6.3. The derived forcing simulation used a nested grid which allowed us to use a much larger computational domain than the one used in the dry simulation. Because of this, the derived forcing simulation was not affected by the errors in the lateral boundaries that diminished the accuracy of and limited the length of integration in the moist simulation. The thermal forcing was applied within a fine resolution grid 450 km in x by 360 km in y and a horizontal resolution of $\Delta x = \Delta y = 3$ km. This fine grid was embedded within a coarse grid 900 km by 630 km with a resolution of $\Delta x = \Delta y = 9$ km. The vertical domain was 16.1 km and the vertical vertical resolution was $\Delta z = 400$ m on both grids. The boundary conditions and initial conditions were the same as in the moist simulation, and Coriolis force was neglected as in the moist simulation. The conditions of the derived forcing simulation are summarized in Table 6.1.

Figure 6.2b shows the y-averaged x component of the velocity at 2 hours generated by the thermal forcing shown in Fig. 6.3a. The line-averaged u field shows all of the features associated with the quasi-two-dimensional conceptual model of squall lines: the RI extends 150 km behind the gust front and shows a descending character over its entire length, the FTRF extends rearward for a similar distance, and the LAF extends 100 km ahead of the storm. Figure 6.2b can be compared to Fig. 6.2a, which shows the y-averaged u field in the moist simulation at 4 hours. The two hour offset between the two simulations accounts for the difference in the initiation of the simulations and is analogous to the two hour offset used in comparing the two-dimensional dry and reference simulations (see Section 4.2.1). The y-averaged FTRF in the derived forcing simulation exceeds 20 m s^{-1} in, which is

comparable to the 24 m s^{-1} in the reference simulation. The RI is stronger in the derived forcing simulation and extends farther to the rear. The LAF in the derived forcing simulation is considerably stronger than in the moist simulation and shows a second maximum near the right boundary not present in the moist simulation. In the two-dimensional simulations presented in Section 4.2.1, a similar overestimate of the LAF was observed in the simulation that was performed dry. In Section 4.2.1 the excess in the LAF was attributed to the unrealistic way in which the thermal forcing was switched on impulsively at the start of the dry simulation, whereas in the moist simulation the forcing evolved gradually with the convection. Nevertheless, the overall similarity of the circulation in the moist and derived forcing simulations suggests that the line-normal quasi-two-dimensional circulation around squall lines is principally the result of the time-mean thermal forcing in the leading convective line. Chapter 4 demonstrated that this is true in two dimensions; the comparison of the three-dimensional moist and derived forcing simulations has verified this is also true in three dimensions.

6.2.2 Evolution of the line-averaged velocity

The limited domain of the moist simulation makes it difficult to analyze the horizontal propagation of the FTRF, RI, and LAF. Furthermore, the propagation of these features in the model is strongly influenced by errors in the boundary conditions and cannot be considered representative of real storms. Alternatively, we can examine the propagation of these features in the three-dimensional derived forcing simulation which was performed using a much larger domain. Figure 6.4a shows that the rear edge of the spreading RI, FTRF, and low-level cold pool are vertically aligned at x = -220 km 3 hours into the derived forcing simulation. For convenience this alignment has been labeled as feature 2 in Fig. 6.4a; it is analogous to feature 2 in the two-dimensional simulations. Feature 2 maintains its vertical structure as it propagates to x = -310 km in Fig. 6.4b and leaves a perturbed velocity field in its wake that includes the FTRF, RI, and the low-level cold

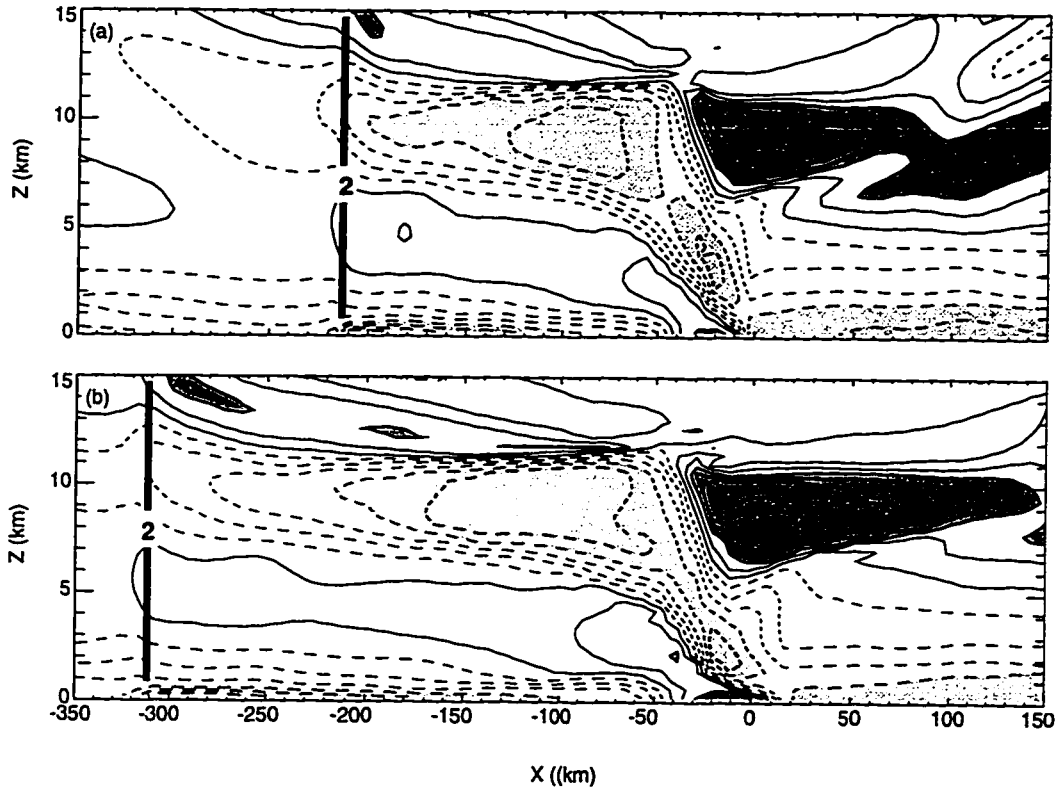

Figure 6.4. The y-averaged u field in the derived heating simulation at (a) 2 hours and (b) 3 hours. Contours and shading as in Fig. 4.2.

pool. (The cold-pool is indicated by the low-level front-to-rear flow.) The fact that feature 2 maintains its vertical structure as it propagates is strong evidence that feature 2 is not merely being advected by the prevailing winds; simple advection by the sheared wind field would distort its vertical structure. The absence of thermal forcing in this region eliminates the possibility that feature 2's propagation is influenced by local thermal forcing. The elimination of advection and local forcing leaves gravity waves as the mechanism responsible for the propagation of this feature. Further, the propagation of feature 2 is reminiscent of the simple linear gravity wave propagation presented in Fig 1.1. Notice that the velocity field in Fig. 6.4 is a line-averaged velocity which implies that the vertical alignment of the FTRF, RI, and low-level cold pool is a common feature along the central

120 km of the system. This alignment of the RI, FTRF, low-level cold pool is also apparent in individual cross sections through the line (not shown).

The low-level cold pool, indicated by the front-to-rear velocities in the surface layer, extends forward to x = 10 km in Fig. 6.4b, somewhat ahead of its position at x = 0 km an hour earlier (Fig. 6.4a). The cold pool continues to spread forward as the simulation progresses; at 6 hours the low-level cold pool is at x = 50 km. In observations of the 22 May 1976 squall line, there was no forward spread of the low-level cold pool. A similar forward spread in the low-level cold pool can be observed in some of the two-dimensional simulations forced by analytic thermal forcings and presented in Section 5.4.2. In these cases, the forward spread of the cold pool is associated with an over-estimate of the low-level cooling. The thermal forcing used in the derived forcing simulation was based on the latent heating and cooling in the moist simulation between 3 and 4 hours. This time period includes an early phase of the storm's evolution, when the low-level cooling was considerably stronger than in the storm's mature phase. In the two-dimensional dry simulation presented in Chapter 4 the circulation was generated by a thermal forcing based on the latent heating and cooling from 4.5 to 6.5 hours in the two-dimensional reference simulation, a time period that did not include the early phase of the storm's evolution. The cold pool that developed in this simulation did not spread forward. An additional two-dimensional dry simulation, in which the thermal forcing was constructed by averaging the latent heating and cooling in the two-dimensional reference simulation from 3 to 4 hours, produced a cold pool that spread forward. This suggests that the time-mean thermal forcing later in the storm projects more directly onto the gravity wave modes responsible for the circulation around mature squall lines, and earlier in the lifetime of the storm the time-mean thermal forcing includes a strong low-level cooling that would lead to forward spreading of the low-level cold pool if the cooling were to persist.

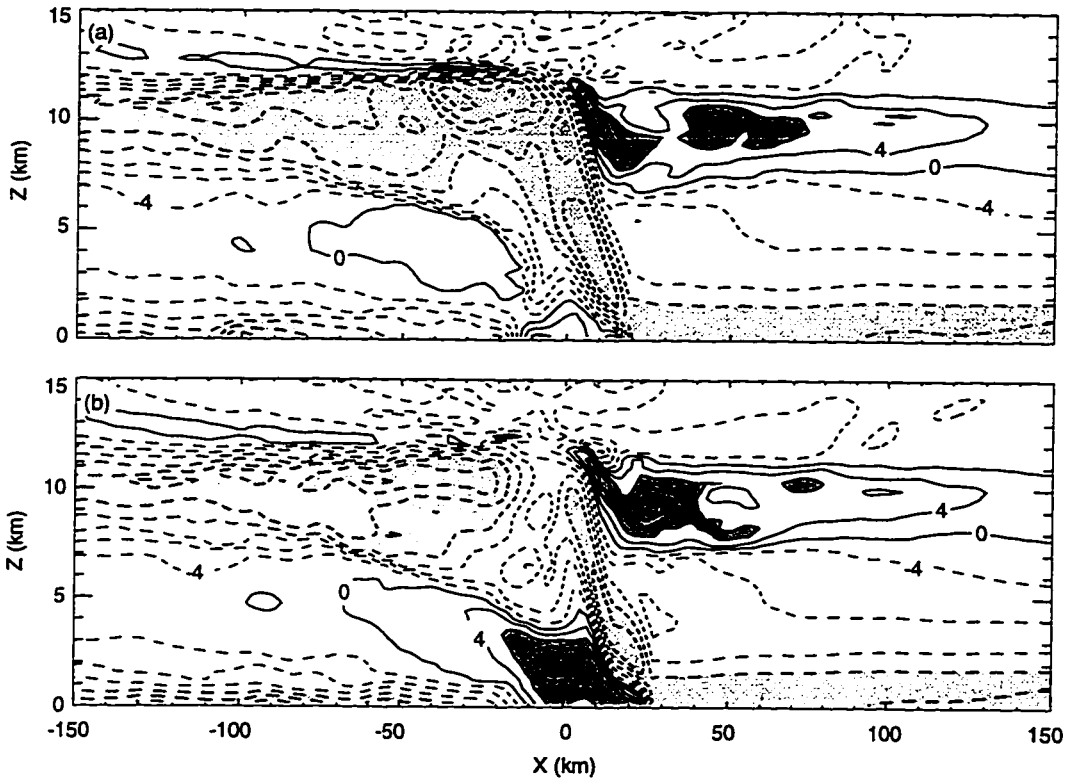

Figure 6.5. The u field at (a) y = -20 km and (b) y = -40 km 4 hours into the moist simulation. Contours and shading as in Fig. 4.2.

6.2.3 Along-line variability of the circulation

Figures 6.5a and 6.5b show the u field at 4 hours at y = -20 km and y = -40 km, respectively, in the moist simulation. Both cross sections exhibit all the features of the quasi-two-dimensional conceptual model of the circulation, including the FTRF, RI, and LAF. The *strength* of these features at y = -20 km and y = -40 km does, however, differ. At y = -40 km (Fig. 6.5b), where the convection is strongest and the line bows outward, the RI extends to x = -50 km and shows a peak velocity of 16 m s^{-1} in the region of the convective line. At y = -20 km (Fig. 6.5a), to the north of the line's bow where the convection is weaker, the RI is also weaker and peaks at 8 m s^{-1}. Unlike the RI at y = -40 km which extends continuously into the convective region, the RI at y = -20 km shows a gap at $x \sim$

-20 km. The FTRF also shows similar along-line variations; in the cross section at y = -40 km the FTRF is considerably less continuous than in the cross section at y = -20 km. This difference is most pronounced close to the leading line, at $x \sim 0$ km. The LAF, on the other hand, shows less difference between Figs. 6.5a and 6.5b than either the FTRF or RI.

A paucity of observational studies of the along-line variability of squall lines makes it difficult to determine how representative the variability shown in Fig. 6.5 is of real squall lines. It has been suggested that the strongest RI occurs behind the bowed portion of the line (Brandes 1989; Weisman 1992; Jorgensen and Smull 1993). Klimowski (1994) used dual-Doppler radar data to construct several line-normal cross sections through a developing squall line. In some of Klimowski's cross sections, the RI does not extend continuously to the gust front but is separated from the low-level gust front by a region of front-to-rear flow, as shown in Fig. 6.5. Other cross sections through the same storm, however, show a smooth RI that extends all the way to the gust front. The FTRF also shows a considerable variation along the line in Klimowski's analysis. Johnson and Hamilton (1988), using wind-profiler and sounding data to construct line-normal cross sections through the trailing anvil of the 10-11 June 1985 PRE-STORM squall line, also found that the FTRF and RI showed significant along-line variations.

Figures 6.6a and 6.6b show the u field 2 hours into the derived forcing simulation at y = -20 and y = -40 km, respectively. Comparing the two figures reveals that the line-normal circulation in the derived forcing circulation also varies in the along-line (y) direction. At y = -20 km, the FTRF is less continuous than at y = -40 km, particularly in the region near $x \sim 0$ km. The RI is stronger at y = -20 km than at y = -40 km. A similar co-location of strong RI and discontinuous FTRF is apparent in the moist simulation (Fig. 6.5). The along-line variability in the derived forcing simulation is somewhat less pronounced than in the moist simulation, most likely as a consequence of the smoothing applied to the thermal forcing used in the reference simulation.

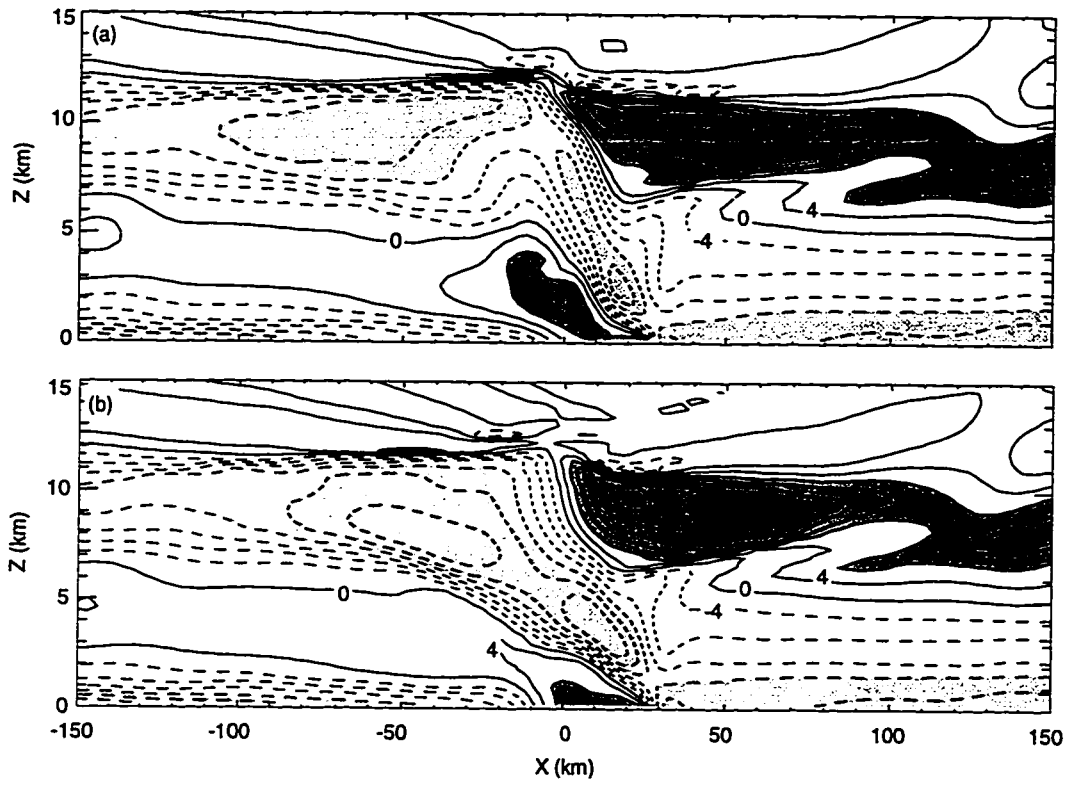

Figure 6.6. The u field at (a) y = -20 km and (b) y = -40 km 2 hours into the derived forcing simulation. Contours and shading as in Fig. 4.2.

6.2.4 Three-dimensional circulation

Figure 6.7a shows the horizontal velocity at a height of 350 meters 4 hours into the moist simulation. By this time, the convective line, indicated by the darkly (lightly) shaded regions of heating (cooling), no longer shows evidence of its artificial initiation. The moist simulation began with vigorous vertically oriented convection that occurred in isolated clusters around the warm bubbles. These early convective events dissipated 2 hours into the simulation, and a more continuous band of convection formed. This later continuous band of convection was weaker than the earlier isolated convection and exhibited the backward slant with height characteristic of squall lines. At 4 hours, the convective line is $\sim$ 200 km long (Fig. 6.7 shows only the southern half of the domain, since the moist simu-

lation was performed assuming symmetry about $y = 0$ km) and bows out to the south and north of the line's center. The region of bowing is also the region of the strongest convection. Skamarock *et al.* (1994), using a three-dimensional nested-grid model with warm cloud microphysics to simulate an idealized squall line, noticed a similar behavior in the convective leading line of their simulations. They found that the convection was initially strongest at the line's end, and that the areas of strong convection and bowing gradually migrated to the line's center (see their Figs. 5 and 6). In our moist simulation the most intense convection did appear to migrate toward the center. Because of the computational constraints imposed by the small spatial domain, however, the moist simulation ran only to 4 hours, which was not long enough to for the apex of the bowing region to move all the way to the center of the line.

The low-level circulation in Fig. 6.7a is dominated by convergence along the gust front. (The gust front is indicated by the thick dashed $\theta' = -1$ K contour.) Unlike the simulation performed by Skamarock *et al.* (1994), the low-level winds in the moist simulation do not show much evidence of a southward turning at the line's southern end. The circulation in Fig. 6.7a is, however, strongly influenced by the proximity of the computational boundaries in the moist simulation. The imperfect boundary condition results in artificial convergence which initiates convection. By time 4 hours, this spurious convection has spread to just south of the convective line, and is visible in Fig. 6.7 at $x \sim -100$ km and $y < -120$ km. Closer to the line's center, where the spurious convection at the boundary exerts less influence on the solution, the circulation is fairly uniform in the along-line direction.

The midlevel circulation in the moist simulation (shown in Fig. 6.7b) is considerably weaker than the flow at low levels. The weak westerly component of the storm relative winds in the region -50 km $< x < 0$ km is evidence of the RI. The circulation in this region also shows evidence of a large anticyclonic vortex, with easterly flow at the south end of the line ($y = -100$ km) and westerly flow at the line's center ($y = 0$ km). This vortex, together with the a complementary cyclonic vortex in the northern part of the domain, resembles the mesoscale vortices in the nested grid simulation of Skamarock *et al.* (1994). Weisman

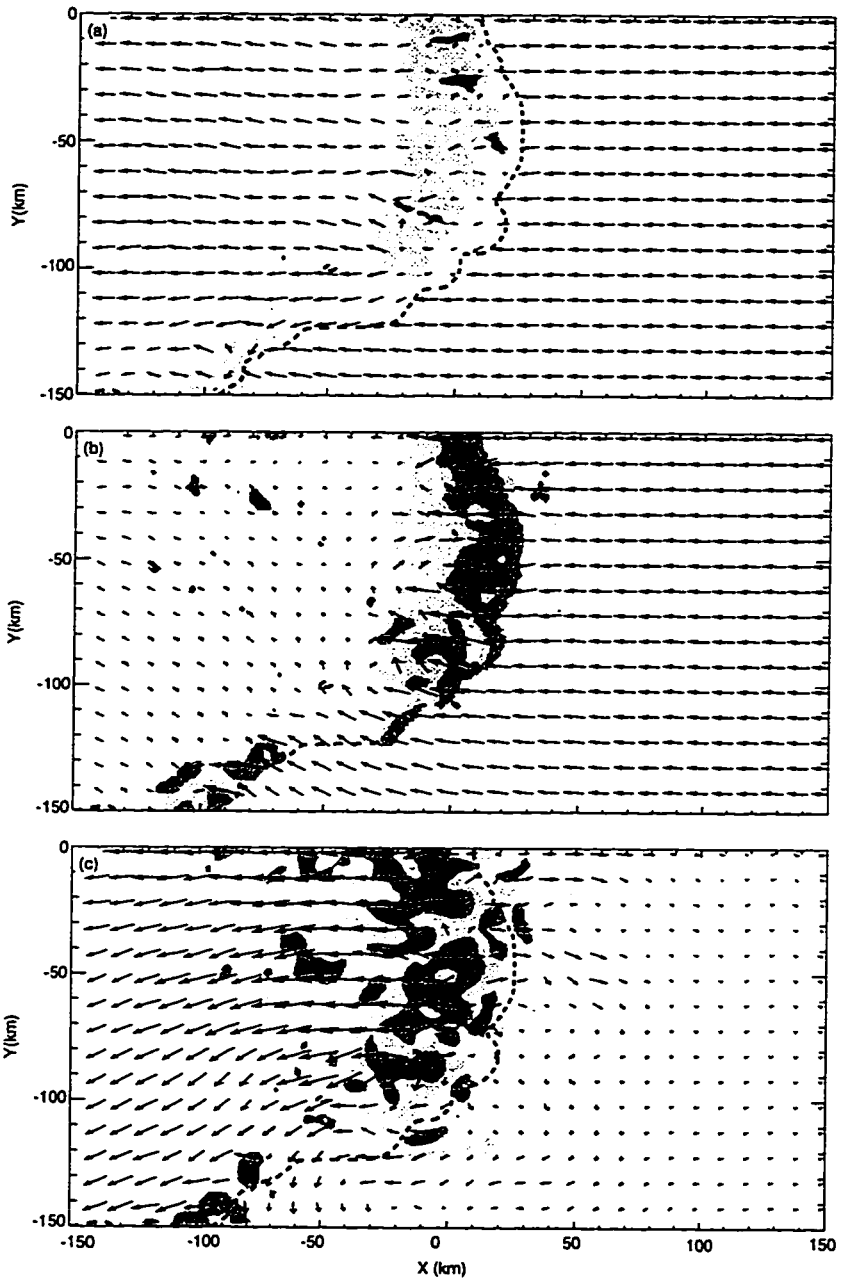

Figure 6.7. Storm relative horizontal velocity vectors at 4 hours and height (a) 350 m, (b) 3000 m, and (c) 8000 m in the moist simulation. Dark (light) shading indicated heating (cooling) greater than 0.001 K s^{-1}. Thick dashed line is the $\theta' = 1.0$ K contour at $z = 350$ m. In (a) vector length of one grid box corresponds to a speed of 20 m s^{-1}. In (b) and (c) a vector of length one grid box corresponds to a speed of 10 m s^{-1}.

(1992) and Skamarock *et al.* (1994) suggested that these vortices act together to strengthen the RI at the center of the line. In Fig. 6.7b the strongest RI is not at the center of the line, but immediately behind the strongest convection at $y \sim$ -40 km. Fig. 6.7b, however, shows the circulation relatively early in the storm. Skamarock *et al.* (1994) had a similar circulation in their three-dimensional nested simulation at time 4 hours (see their Fig. 5b) and by 6 hours in their simulation, both the RI and the convection were strongest at the line's center.

At upper levels, the storm-relative winds behind the leading line are predominantly easterly and much stronger than the westerlies ahead of the line, as can be seen in Fig. 6.7c. The easterlies behind the line are the FTRF, and the westerlies ahead of the line represent the lowest levels of the LAF. The flow to the southwest of the line exhibits a cyclonic turning and becomes increasingly northerly as it leaves the domain. This is similar to the simulation performed by Skamarock *et al.* (1994), which, in turn, were similar to the squall lines in the climatological study of Houze *et al.* (1990).

Figure 6.8a shows the horizontal circulation at $z = 350$ m generated by the thermal forcing shown in Fig. 6.3a 2 hours into the derived forcing simulation. The circulation at 2 hours can be compared to the circulation in the moist simulation at 4 hours as discussed earlier. Ahead of the thermal forcing (regions of heating and cooling in Fig. 6.8 are indicated by the dark and light shading, respectively) the circulation shows convergence along the boundaries of the low-level cold pool, which is indicated by the $\theta' = 1$ K contour. The winds behind the thermal forcing are predominately westerly, but show a southerly (northerly) component near the thermal forcing's southern (northern) end. A similar lateral convergence was noted in a composite rawinsonde analysis of a GATE[1] squall line by Gamache and Houze (1981). The low-level winds in the moist simulation (Fig. 6.7a) don't show a similar turning, but this is probably due to errors associated with the boundary conditions and the influence of the spurious convection that develops in the moist simula-

[1] GATE is the *G*lobal Atmospheric Research Programme's *A*tlantic *T*ropical *E*xpirement.

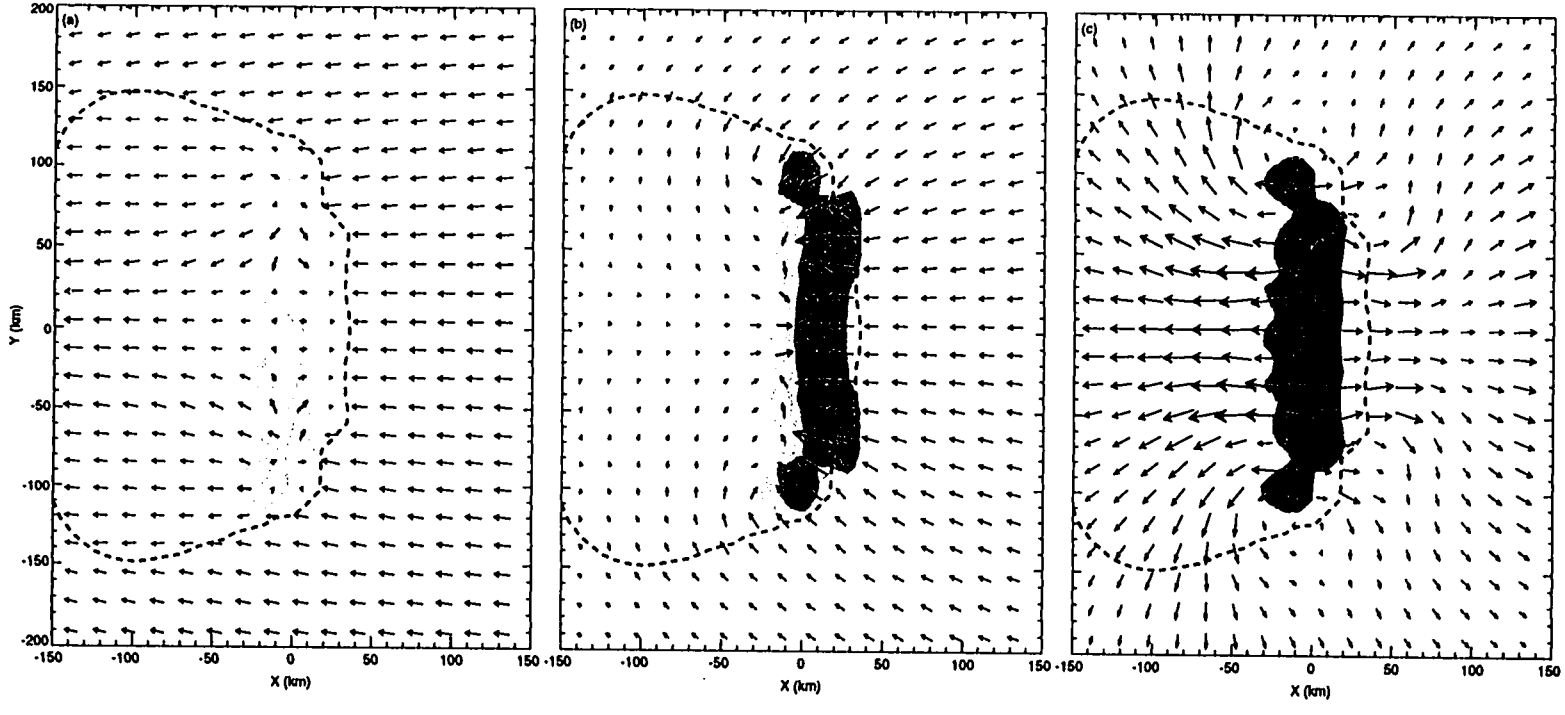

Figure 6.8. Storm relative horizontal velocity vectors at 2 hours and height (a) 350 m, (b) 3000 m, and (c) 8000 m in the derived forcing simulation. Shading and thick dashed line as in Fig. 6.7. In (a) a vector of length 1 grid box is 12 m s^{-1}. In (b) and (c) a vector of length 1 grid box is 6 m s^{-1}.

tion. Both of these problems are avoided in the derived forcing simulation by using the time-mean thermal forcing shown in Fig. 6.3a which excludes the spurious convection and by using a nested grid to minimize the impact of the computational boundaries. For these reasons, the low-level circulation in the derived forcing simulation (Fig. 6.8a) more closely resembles the circulation in the simulations by Skamarock *et al.* (1994) than the winds in the moist simulation (Fig. 6.7a).

Figure 6.8b shows the midlevel circulation in the derived forcing simulation shown in Fig. 6.3. It is dominated by two large-scale vortices centered around the line's ends and extending to the center of the line where they contribute to the RI. Weisman (1992) and Skamarock *et al.* (1994) argued that this vortex couplet makes an important contribution to the RI. The presence of such a couplet in the derived forcing simulation demonstrates that the gravity waves forced by the time-mean thermal forcing are sufficient to produce the large-scale vortex couplet that contributes to the formation of a strong RI. Comparison of Figs. 6.7b and 6.8b reveals that the vortices are more pronounced in the derived forcing simulation than in the reference simulation. This may reflect more accurate treatment of the line-ends in the derived forcing simulation, which avoids the spurious convection near the lines' ends that occurs in the moist simulation.

The upper-level circulation in the derived forcing simulation is shown in Fig. 6.8c. The FTRF shows up as easterlies behind the thermal forcing while the LAF shows up as upper-level westerlies ahead of the thermal forcing. The flow is in the east-west plane for -50 km $< y <$ 50 km while to the north (south) of this the flow becomes increasingly southerly (northerly). In general, the flow shows evidence of the upper-level divergence apparent in real squall line systems and in the moist simulation. The LAF in the derived forcing simulation is more pronounced than in the refence simulation but, as discussed in connection with Fig. 6.2b, the strong LAF in the derived forcing simulation may be a result of the instant start of the thermal forcing.

In summary, the time-mean thermal forcing shown in Fig. 6.3a generates many of the features that are observed around real squall lines and in realistic three-dimensional nu-

merical simulations of squall lines. In particular, the three-dimensional thermal forcing produced a line-normal circulation that included a FTRF, RI, and LAF similar to the quasi-two-dimensional conceptual model of squall lines and to the circulation observed in real squall lines. The thermal forcing also produced a realistic three-dimensional circulation that included a large-scale vortex couplet which contributed to the development of a strong midlevel RI. The close similarity of the circulation in the moist and derived forcing simulations suggests that the large-scale circulation around squall lines is the result of gravity waves forced by the time-mean thermal forcing in the leading convective line. While this thesis was demonstrated for the line-normal circulations in the two-dimensional simulations presented earlier, the simulations of this chapter extend this thesis to the fully three-dimensional circulation around squall lines.

6.3 Sensitivity to the three-dimensional thermal forcing

Section 5.4.2 showed that the circulation in the two-dimensional simulations was very sensitive to the two-dimensional structure of the thermal forcing. It seems likely, therefore, that the circulation in three-dimensional simulations might be sensitive to the three-dimensional structure of the thermal forcing. In order to investigate this sensitivity, additional simulations were performed with different profiles of the thermal forcing and the same large-scale environment. As pointed out in Section 5.4.2, changes in the thermal forcing are often related to changes in the environment. These tests should be understood, therefore, to examine only how changes in the thermal forcing affect the propagation of gravity waves in a hypothetical fixed environment.

6.3.1 *Line-shaped thermal forcing*

A line-shaped thermal forcing can be described by

$$Q = \begin{cases} \hat{Q} & \text{if } |y| < L_1 \\ \hat{Q}\frac{1}{2}\left(1 + cos\left(\pi\frac{|y|-L_1}{L_2-L_1}\right)\right) & \text{if } L_1 < |y| < L_2 \\ 0 & \text{otherwise} \end{cases}, \tag{6.1}$$

where $\hat{Q}$ is the thermal forcing shown in Fig. 5.4b, L_1 is 160 km, and L_2 is 200 km. The line lies along the y axis, with $y = 0$ km at the center and is of uniform magnitude, except at the edges where its magnitude decreases smoothly to zero. The line-normal profile of Q is given by the thermal forcing used in the two-dimensional dry simulation presented in chapter 4, which was chosen to prevent the forward spread of the low-level gust front observed in the derived forcing simulation. Except for an enhanced region of low-level cooling, however, the line-average of the thermal forcing in the three-dimensional moist simulation is similar to this two-dimensional thermal forcing.

Using the thermal forcing described by (6.1), an additional was performed using the nested model run without any microphysical parameterization. In this simulation the finer resolution grid was 540 km in the across-line dimension (x) and 540 km in the along-line dimension (y), and the coarser grid it is nested in was 1080 km in x and 810 km in y. As in the derived forcing simulation, $\Delta x = \Delta y = 3$ km on the fine grid and $\Delta x = \Delta y = 9$ km on the coarse grid. The vertical domain for both grids was 16.1 km, and the vertical resolution was $\Delta z = 400$ m. The boundary conditions and initial conditions were the same as in the moist and derived forcing simulations, and the Coriolis force was neglected, as in the moist simulation. The conditions of this simulation, the "line-shaped forcing" simulation, are summarized in Table 6.1.

Figure 6.9 shows the u field at 6 hours generated by the thermal forcing shown in (6.1). Unlike the derived heating simulation, the low-level cold pool does not spread ahead of the thermal forcing, but stays near $x = 0$ km. Near the center of the line the effects of the line ends are small and the circulation is similar to the circulation caused by an infinitely long

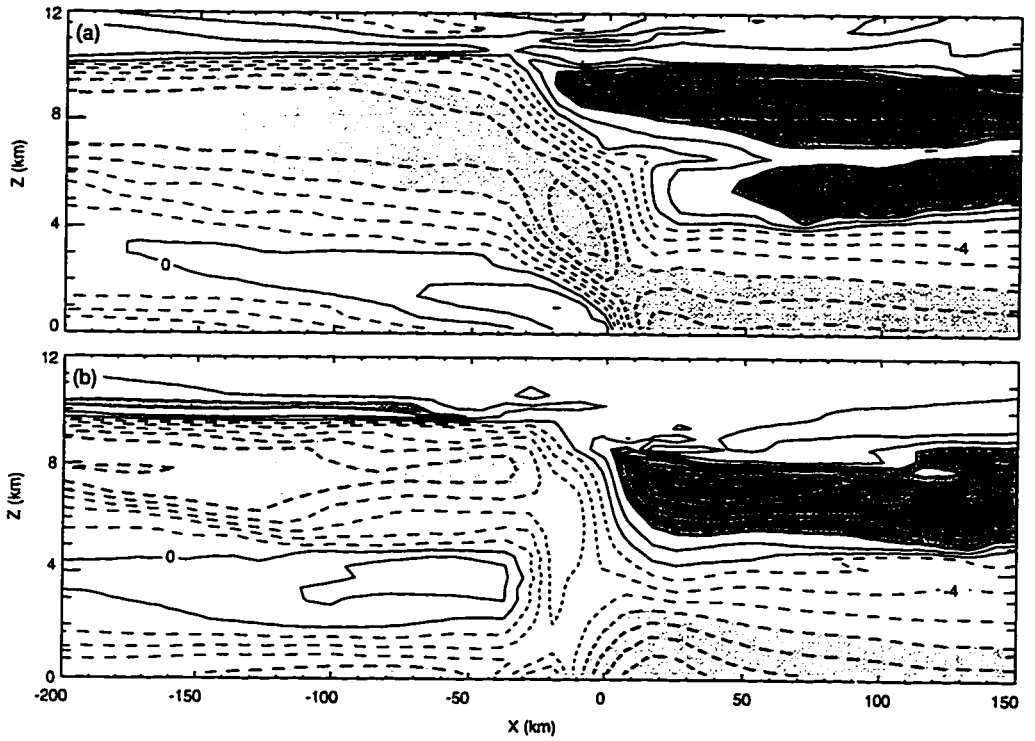

Figure 6.9. The instantaneous x component of the horizontal velocity 6 hours into the line-shaped forcing simulation. (a) A cross section taken at the center of the line, $y = 0$ km. (b) A cross section at $y = 150$ km. Shading and contours as in Fig. 4.2.

line (*i.e.* the circulation is similar to the circulation in the two-dimensional dry simulation discussed in Chapter 4). The u-velocity at $y = 0$ km shows an FTRF and LAF above $z \sim$ 4 km and an RI that descends from $z = 4$ km at $x \sim$ -180 to the gust front ($x = 0$ km). Farther from $y = 0$ km, however, the thermal forcing's finite length has a greater impact on the circulation and the circulation looks less like that in the two-dimensional simulations. At $y = 150$ km (Fig. 6.9b), for example, the RI does not descend to the surface and there is no low-level gust front. The FTRF is also unrealistic; it lacks a backward slant in the region of the thermal forcing.

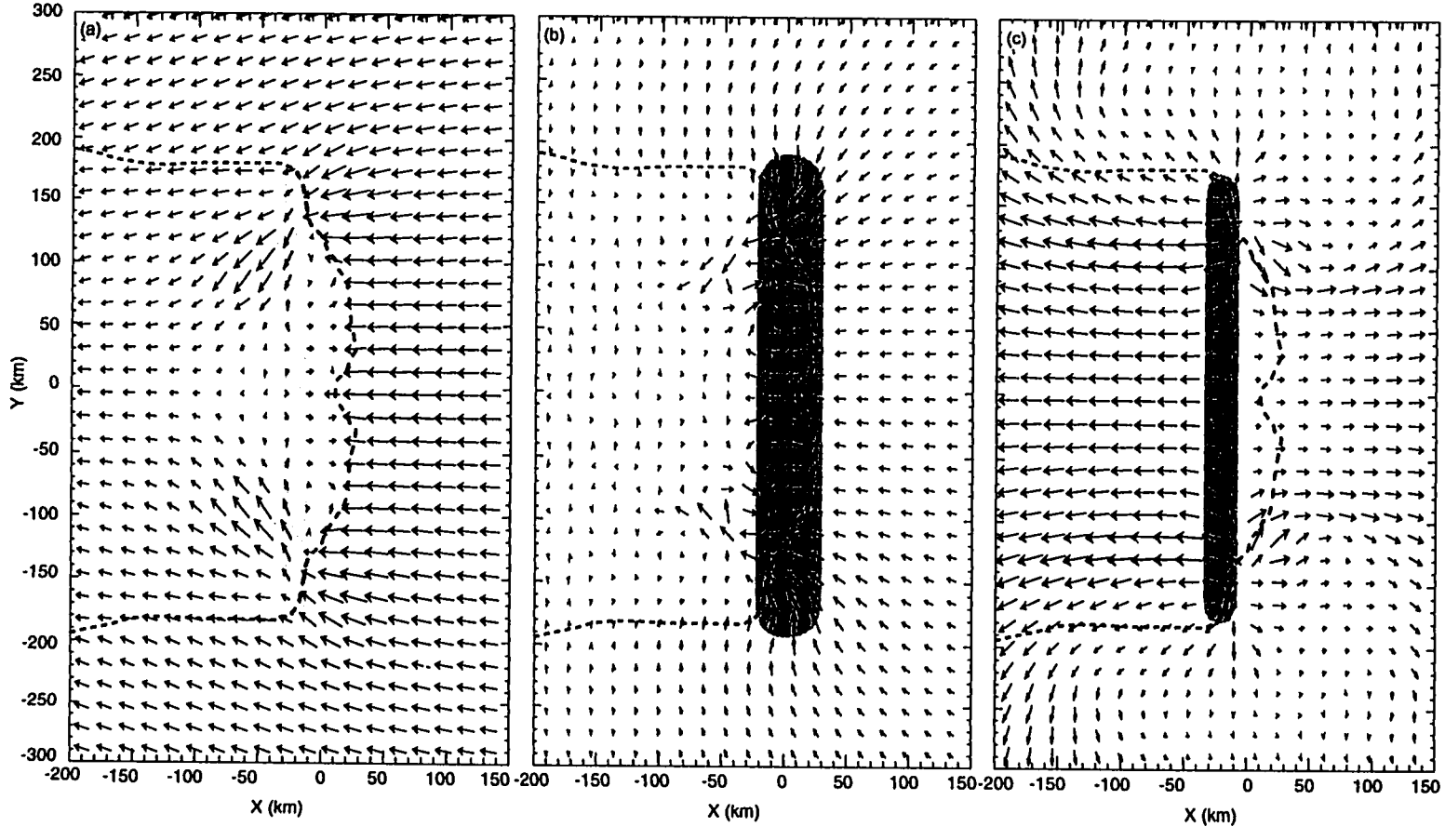

Figure 6.10. Horizontal velocity vectors at (a) 350 m, (b) 3000 m, and (c) 8000 m in the line-shaped forcing simulation at 6 hours. Vectors indicate the horizontal wind, plotted every sixth grid point on the nested grid; a vector of length one grid interval is 10.5 m s^{-1}. Shading and dashed line as in Fig. 6.8.

Figure 6.10a shows the horizontal velocity vectors at 6 hours and a height of 350 m in the line-shaped forcing simulation. At this height, the flow resembles that in the derived heating simulation (Fig. 6.8a); there is convergence along the cold pool (the cold pool is indicated by the the heavy dashed $\theta' =$ -1 K contour), with the strongest convergence along the low-level gust front at the front of the cold pool. To the rear of the thermal forcing, the flow is predominantly easterly, although there is a pronounced southerly (northerly) component to the winds near the southern (northern) end of the thermal forcing at $y =$ -200 km ($y = 200$ km). This turning of the low-level winds toward the line's center just behind the ends of the thermal forcing is not as pronounced in the derived forcing simulation (Fig. 6.8a).

The winds at a height of 8 km, shown in Fig. 6.10c, also resemble the winds in the derived forcing simulation, shown in Fig. 6.8c. The circulation in Fig. 6.10b is dominated by a divergence in the region of the thermal forcing. Behind the the thermal forcing, the FTRF shows up clearly in the easterly flow that extends to the left edge of the figure. The LAF is evident ahead of the thermal forcing, and extends to the right edge of the figure. At the southern (northern) edge of the leading line, the circulation shows a significant northerly (southerly) component; ahead of the thermal forcing this produces an anticyclonic turning in the north and a cyclonic turning in the south, while to the rear this turning is anticyclonic in the south and cyclonic in the north.

The midlevel flow behind the the line-shaped thermal forcing is weak and the and the RI (which would show up as westerly flow at this level) is hard to discern in Fig. 6.10b. The strongest RI doesn't appear at the center of the line as in the derived forcing simulation (Fig. 6.8b); instead the strongest RI is at $y \sim \pm 90$ km. Further, instead of the large anticyclonic-cyclonic vortex couplet that develops in the derived forcing simulation, the flow in the line-shaped forcing simulation (6.1) shows significantly smaller vortices centered at $x \sim$ -10 km and $y \sim$ -100 km. Weisman (1992) and Skamarock *et al.* (1994) attributed the development of the mesoscale vortices at midlevels to the spin up of vorticity at the ends of the line. The lack of large-scale vortices in the midlevel circulation in the

line-shaped forcing simulation suggests that (6.1) fails to correctly describe the lines' ends. Comparing the the thermal forcing given by (6.1) and shown in Fig. 6.8 with the thermal forcing in the derived forcing simulation, shown in Fig. 6.10, reveals that the differences between the two thermal forcings are most pronounced near the lines' ends. In the interior, where the circulation in the two simulations is more similar, the thermal forcings are also more similar.

Additional simulations were performed with shorter lines of thermal forcing. In these simulations unrealistic circulations associated with the arbitrary line ends modified the circulation even in the line's center. Since the 400 km line length used in the line-shaped forcing simulation represents the largest length of convective lines observed in real squall lines, the inability of the line-shaped thermal forcing to produce realistic circulations anywhere but the at the line's center suggests that (6.1) isn't sufficiently realistic to generate the gravity waves responsible for the mesoscale circulation around real squall lines. In particular, the simple treatment of the line ends in 6.1 is inadequate to produce realistic large-scale vortices at midlevels.

6.3.2 Comma-shaped thermal forcing

A comma shaped thermal forcing can be described by

$$Q(x_c, y, z) = \begin{cases} M\hat{Q} & \text{if } |y| < L_1 \\ \hat{Q}\frac{1}{2}\left(1 + cos\left(\pi\frac{|y|-L_1}{L_2-L_1}\right)\right) & \text{if } L_1 < |y| < L_2 \\ 0 & \text{otherwise} \end{cases}, \qquad (6.2)$$

where, as in 6.1, L_1 is 160 km, L_2 is 200 km, and $\hat{Q}$ is the thermal forcing shown in Fig. 5.4b. M is given by

$$M = \begin{cases} \frac{1}{2}\left(1. + cos\left(\pi\frac{|y-P_c|-P_w}{P-w}\right)\right) & \text{if } -P_w - P_c < y < -P_c + P_w \\ 0 & \text{otherwise} \end{cases},$$

where P_c = -100 km and P_w = 50 km. x_c in 6.2 is given by

$$x_c = \begin{cases} \frac{-y^2 R}{L_2^2} & \text{if } y < 0 \\ 0 & \text{otherwise} \end{cases},$$

where R is 100 km. Equation (6.2) describes a comma shaped thermal forcing that has its strongest magnitude at the southern end of the convective line. This profile is similar to the asymmetric leading line structure described in Section 2.2, where the convection is strongest to the south and the leading line is curved.

Figure 6.11 shows the horizontal velocity near the surface generated by the thermal forcing described in (6.2). As in the derived forcing simulation (shown in Fig. 6.8a) the low-level winds are dominated by convergence along the edge of the spreading cold pool (indicated by the dashed $\theta' = 1$ K contour). To the north, the low-level flow is similar to the flow in the line-shaped forcing simulation (shown in Fig. 6.10a) which is not surprising since the thermal forcing described by (6.2) is identical to the one described by (6.1) for $y > 0$ km. In the southern portion of Fig. 6.11a the winds are weaker than in the northern portion, and show less turning toward the center of the line. The flow behind the curved portion of the line looks more like the flow in the derived forcing simulation than either the flow in the northern portion of this simulation or the flow in the line-shaped forcing simulation. The thermal forcing in the derived forcing simulation shows a slight curvature like the one described by (6.2) and this may account for the similarity in the flow in these two simulations. Overall, however, the degree of resemblance between the low-level flow in the derived forcing simulation and the comma-shaped forcing simulation is low.

The midlevel winds in the comma-shaped forcing simulation (Fig. 6.11b) are dominated by a pair of counter-rotating vortices, cyclonic to the north and anticyclonic to the south, that are centered around x = -50 km, y = -120 km. These vortices surround the only region of significant RI behind the southern portion of the line. There were vortices on either side of the RI in the derived forcing simulation and in simulations with microphysical forcing performed by Skamarock *et al.* (1994), but in both of these cases the vortices were much larger in horizontal scale. The vortices in Fig. 6.11b form at the boundaries of a region in

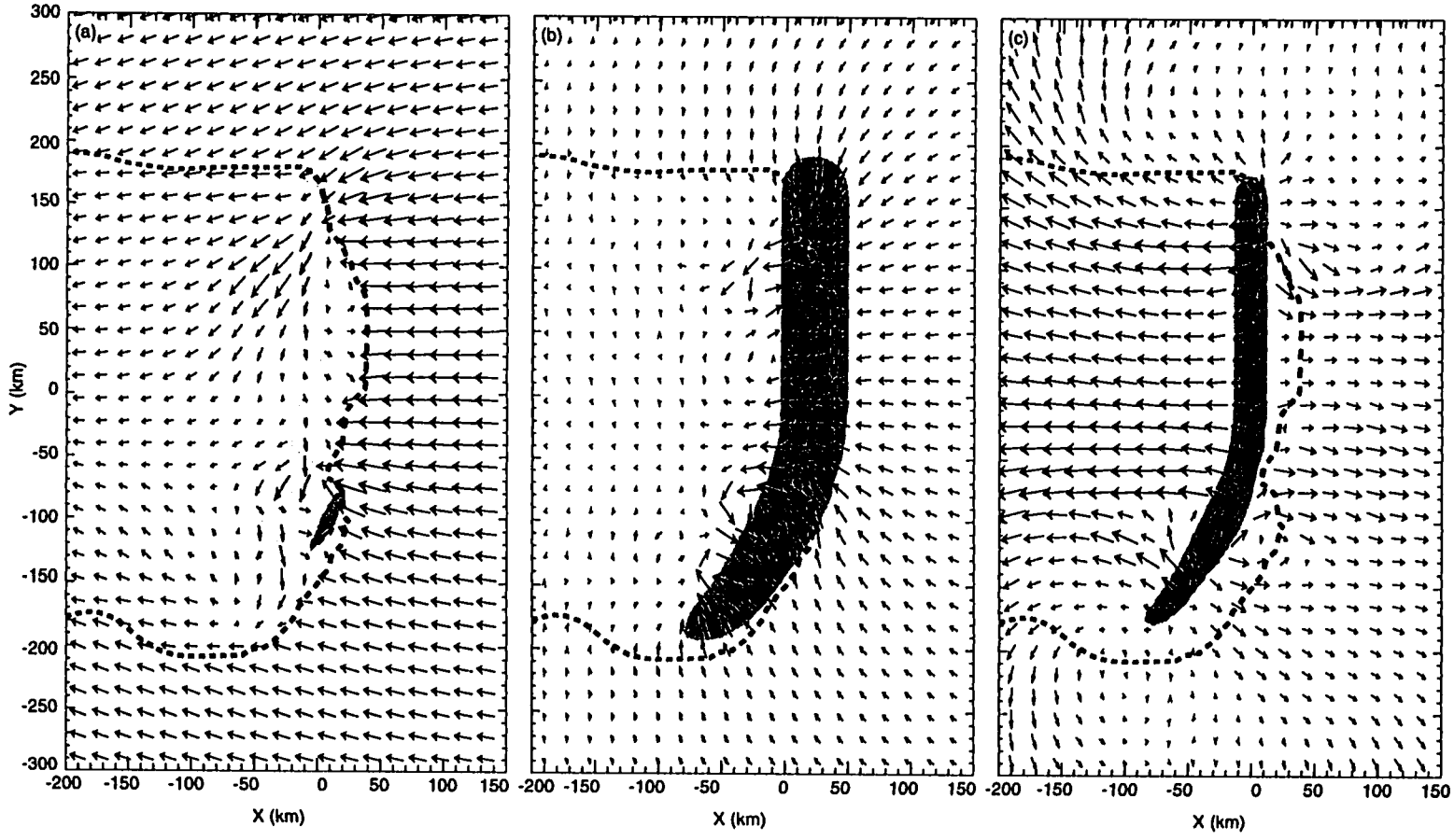

Figure 6.11. Horizontal velocity vectors at a height of (a) 350 m, (b) 3000 m, and (c) 8000 m in the comma-shaped forcing simulation at 6 hours. Vectors, shading, and lines as in Fig. 6.8.

which the magnitude of the thermal forcing was increased (see Eq. 6.2). In additional dry simulations using a simple line of thermal forcing with a region of enhancement, a similar vortex couplet was observed to form at the edges of the region of enhanced thermal forcing. When the region of enhanced thermal forcing was enlarged, the vortices moved farther apart but were otherwise unchanged. Thus, the small vortices in the comma-shaped thermal forcing simulations appear to be associated with the edges of the region of enhanced thermal forcing.

The upper-level winds in Fig. 6.11c show an organized FTRF that extends behind the thermal forcing to the left boundary of the figure. The FTRF is weakest immediately behind the region of strongest thermal forcing at x = -50 km, y = -170 km. The LAF is also weakest in this region, but the RI at midlevels is strongest in this region (see Fig. 6.11b). The structure of the FTRF is complicated in the southern portion of the domain as the FTRF turns from southeasterly in the south to more easterly in the north. The winds ahead of the thermal forcing in the south also show a turning from northwesterly in the south to westerly in the north. This turning has the effect of keeping the flow ahead of and behind the thermal forcing perpendicular to the axis of thermal forcing.

Like the line-shaped thermal forcing, the comma-shaped thermal forcing generated a *qualitatively* correct quasi-two-dimensional circulation that included the FTRF, LAF and RI in the interior of the forcing. Both of these circulations, however, were *quantitatively* different from the circulation in the derived forcing simulation, particularly in the strength of the RI. The two simulations did a relatively poor job of simulating the fully three-dimensional flow, particularly near the ends of the forcing. The comma-shaped thermal forcing did produce a vortex couplet bounding a region of stronger RI at midlevels, but the vortices were significantly smaller in scale than those observed in the dry simulation and they were displaced from the line's center. The results here indicate that the gravity waves that determine the circulation around squall lines are strongly influenced by the three-dimensional structure of the heat source. In particular, the three-dimensional thermal forcing of squall lines is not a mere extension of the thermal forcing in two dimensions,

but involves significant sensitivity to processes occurring at the line's ends.

6.4 Sensitivity to the Coriolis force

This section investigates the impact of the Coriolis force on the the gravity waves that determine the circulation around squall lines. In these simulations f, the Coriolis parameter, was set equal to 1.0×10^{-4} s^{-1}, a value appropriate for the midlatitudes. The initial thermodynamic sounding and vertical wind profile are given in Fig. 4.1 and the initial environment was considered uniform in x and y. These initial conditions were chosen in order to facilitate comparison with the other simulations discussed in this chapter which were also performed with horizontally uniform initial conditions. In a rotating atmosphere, however, the horizontally uniform initial conditions violate thermal wind balance; the vertical shear of the horizontal wind is not balanced by a y gradient in θ. As a result of this imbalance, a circulation will develop in this environment even in in the absence of any external forcing. In a simulation performed with no external forcing, the velocity field, which was originally easterly, turned to become southeasterly. The turning was less than 5° at 6 hours into the simulation, which is small compared to the perturbations that developed from the thermal forcing.

Figure 6.12 shows the flow in the moist Coriolis simulation. This simulation included the Coriolis force and a parameterization of microphysical processes. The simulation was run with the same model and at the same resolution as the moist simulation described in Section 6.2. The domain of the moist Coriolis simulation was 200 km in x by 400 km in y, and all the lateral boundaries were open. As in the moist simulation, the boundary conditions in the moist Coriolis simulation produced some spurious convection near the boundaries; this convection is visible in Fig. 6.12 near y = -150 km.

The low-level winds at 4 hours in the moist Coriolis simulation are shown in Fig. 6.12a. The circulation is dominated by convergence at the boundaries of the low-level cold pool (the low-level cold pool is indicated by the thick dashed θ'= -1 K contour). By comparing

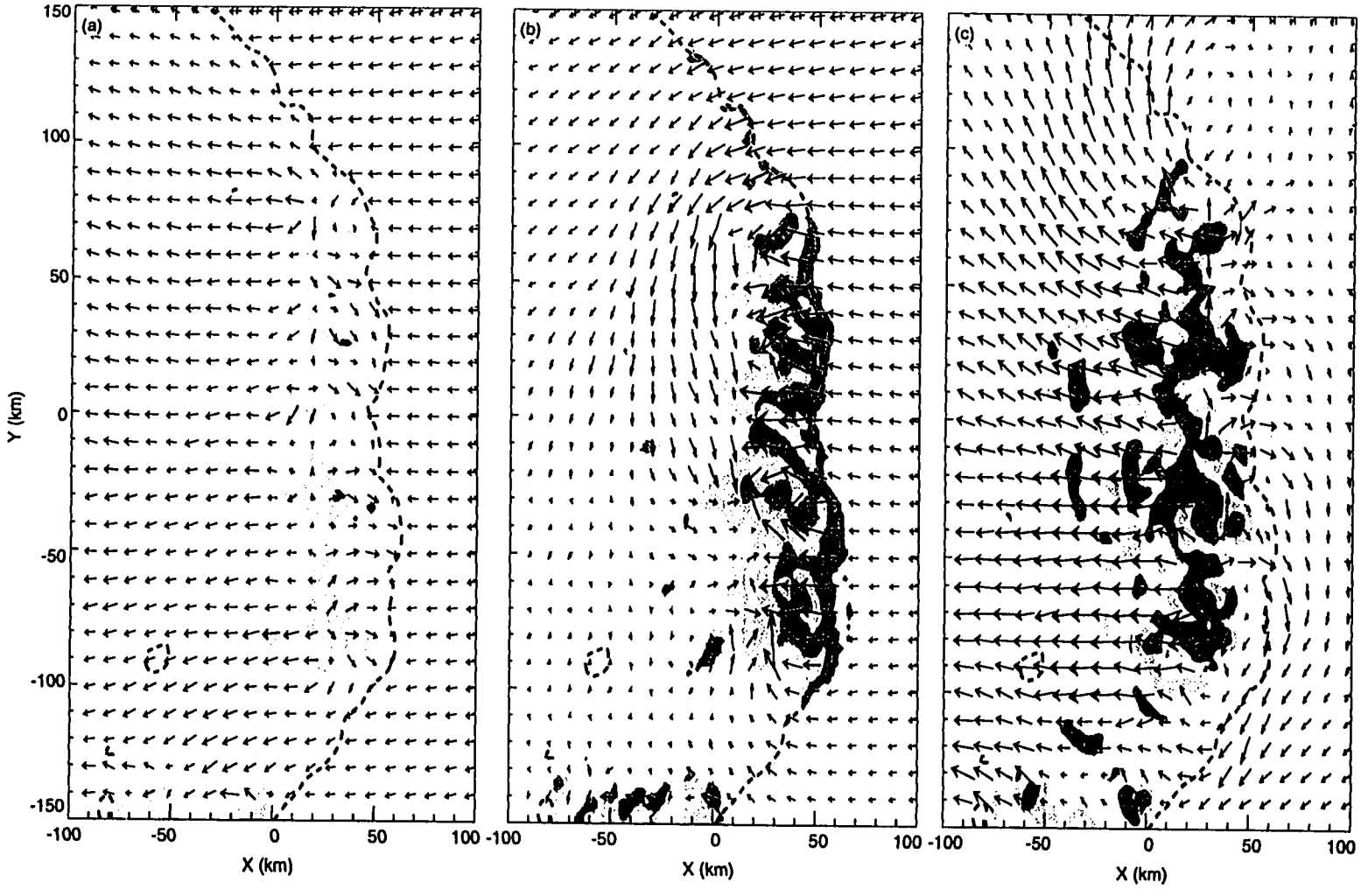

Figure 6.12. Storm-relative horizontal velocity vectors at 4 hours and height (a) 350 m, (b) 3000 m, and (c) 8000 m in the moist Coriolis simulation. Shading, lines, and vectors as in Fig. 6.7.

the flow in the moist Coriolis simulation to the flow in the moist simulation we can gain some insight into the role of the Coriolis force on the circulation that develops around squall lines. Four hours into the simulations, the Coriolis force has little impact on the low-level circulation, as can be seen by comparing Fig. 6.7a and Fig. 6.12a. (Care should be taken in comparing these two figures since the scales are different in the two figures.) Skamarock *et al.* (1994) performed numerical simulations of squall lines using a much larger nested grid, both with and without the Coriolis force. They also showed little difference in the low-level winds between the simulations performed with and without the Coriolis force at 4 hours. At later times, however, the low-level winds in the two simulations differ.

Figure 6.12b shows the midlevel winds at 4 hours in the moist Coriolis simulation. An elongated cyclonic vortex dominates the northern 2/3 of the circulation behind the convective line. A smaller, weaker anticyclonic vortex is also visible to the south of the larger vortex in Fig. 6.12b. In the moist simulation, performed without the Coriolis force, the cyclonic and anticyclonic vortices are equal in size and magnitude (see Fig. 6.7b). The difference in the size and magnitude of the vortices in the two simulations suggests that the planetary vorticity contributes to the development of the cyclonic vortex and inhibits the growth of the anticyclonic vortex in the moist Coriolis simulation. Since the large cyclonic vortex in the moist Coriolis simulation resembles the MCV often observed in the trailing anvil behind real squall lines (Bartels and Maddox 1990; Brandes 1990; Johnson and Bartels 1992; Brandes and Ziegler 1993; Scott and Rutledge 1995), this suggests that planetary vorticity is essential to the development of strong MCVs. Both observations (Bartels and Maddox 1991; Johnson and Bartels 1992) and modeling studies (Zhang 1992; Skamarock *et al.* 1994) have pointed to the importance of the planetary vorticity in developing a strong MCV.

The RI in Fig. 6.12b, which shows up as westerlies behind the convective line, reaches its maximum speed at $x \sim$ -70 km, near the southern edge of the cyclonic vortex. This is consistent with observations of real convective systems, in which the strongest RI is often observed at the southern end of the line (Jorgensen and Smull 1993; Klimowski 1995).

VITA

Rajul Edward Pandya

Ph.D. Atmospheric Sciences, University of Washington, 1996.

B.S. Physics, University of Illinois, 1991.